PLASMA DEFECT ENGINEERED AND CHARACTERISATION OF YTTRIA-STABILISED ZIRCONIA

BY

Fangzhou Shi

A thesis submitted to

The University of Birmingham

for the degree of

DOCTOR OF PHILOSOPHY

School of Metallurgy and Materials

College of Engineering and Physical Sciences

The University of Birmingham

March 2024

Synopsis

Oxygen-deficient zirconia ($ZrO_{2-\alpha}$) holds great promise for applications demanding light absorbing materials and has recently become the focus of many high-quality studies. Despite various approaches taken to manufacture this material, ranging from electrical, chemical, and physical methods, achieving commercial success in the production of bulk $ZrO_{2-\alpha}$ has proven challenging to date. This project aimed to investigate the feasibility and transformation mechanism for plasma-induced blackening of zirconia ($ZrO_{2-\alpha}$) and to illustrate the resulting change in properties and potential for applications.

Different types of plasma technologies (DC plasma and active-screen plasma), variations in DC plasma treatment configurations (contact conditions and cathode material), and a range of treatment parameters (potential, temperature, and duration) were explored to study the conditions for plasma-induced blackening of zirconia and to understand the underlying mechanisms involved in the generation of the black oxygen-deficient zirconia. Comprehensively characterisation of black zirconia generated through low-pressure plasma treatment, against untreated equivalent samples, was characterised in terms of structure, microstructure and properties. In addition, a plasma-induced crack-healing phenomenon was also discovered and fully characterised.

The findings reveal that the bulk-transformed black zirconia can be successfully fabricated by low-pressure plasma treatment from industrially available dense zirconia and that the oxygen-deficient zirconia formed is structurally unmodified from the pristine material. The oxygen-deficient nature of the plasma treated zirconia ($ZrO_{2-\alpha}$) is revealed using a combination of electron paramagnetic resonance (EPR), X-ray photoelectron spectroscopy (XPS) and thermal analysis (TGA and DSC) characterisation techniques. Light absorption behaviour of plasma-treated zirconia, measured via diffuse reflectance spectroscopy (DRS), demonstrates >65% absolute light absorption across the tested spectrum (200-3000 nm). Comparisons of the average absorption across the spectrum indicate a substantial enhancement of 66.2% after plasma treatment of the zirconia.

Furthermore, plasma treatment is also found to lead to a significant reduction in both the direct and indirect bandgap values of zirconia. The direct bandgap decreases from 4.84 eV to 2.61 eV, while the indirect bandgap decreases from 3.19 eV to 1.45 eV.

The results also elucidate the conditions and the mechanism involved in the plasma blackening (reduction) process. The initial location and reduction rate of plasma blackening are determined by the contact conditions with the cathode. The initiation of blackening in oxygen-deficient zirconia is found to consistently arise at locations in direct contact with the cathode, before gradually spreading to non-contacting regions. The black areas are always found to expand from the cathode-facing surface towards the anode-facing surfaces, and the opposing migration of oxygen vacancies and lattice oxygen leads to the hemispherical growth of black regions, which differs from traditional current reduction methods. Throughout the plasma treatment, the degree of blackening (reduction) of zirconia samples varies based on plasma treatment parameters (such as temperature, time, voltage, pressure, etc.), with a positive correlation with the blackening process being observed for most of them.

It has also been found that during the plasma reduction of zirconia, indentation-formed microcracks on zirconia can be healed and microcracks formed by a load of 20 kgf are partially repaired under the plasma conditions of N_2 gas, 500 °C, 10 hours, and 3 mbar pressure. The repair of the cracks is attributed to the plasma induced transformation of the tetragonal phase around the cracks to the monoclinic phase with a lower specific volume as compared with the tetragonal phase, which is accompanied by a volume expansion that enables the closing or repair of the cracks. Raman mapping and XRD measurements around an indent produced by a load of 5 kgf provided strong supporting evidence. Moreover, a unique simultaneous increase in both surface hardness and fracture toughness is also measured following the plasma-treatment of zirconia and is also attributed to the formation of the dispersed monoclinic crystal that pre-stress the material.

Acknowledgements

First of all, I would like to express my great gratitude to my academic supervisors, Prof. Hanshan Dong and Dr Xiaoying Li, for their invaluable supervision and support throughout my PhD study. Their rigorous academic style and diligent research spirit have always been exemplary in my heart. They have provided me with a wealth of inspiring advice, detailed guidance, and valuable patience in my academic pursuits. In addition to their supervision for my academic studies, they have also shared numerous life experiences and offered advice that helped me overcome all kinds of difficulties during challenging periods.

Next, I would like to express special gratitude to my co-supervisor, Dr Behnam Dashtbozorg. Thank you for your consistent recognition, assistance, and guidance. It has been a great pleasure working with you in designing treatments, discussing results, and writing papers. Following your lead, I have gained a wealth of knowledge throughout this process. Your patience in tackling complex issues, academic professionalism, and proficiency in handling various experimental equipment and programs have impressed me. Your sense of responsibility toward apprentices like me is commendable, and meeting you on my academic journey has been an immense stroke of luck.

I must express my deep appreciation to the studentship from the Centre for Doctoral Training in Innovative Metal Processing (IMPaCT) funded by EPSRC, UK (EP/F006926/1), which made my PhD study possible.

I would like to express my gratitude to my companions, Mr Yepeng Yang, Mr Weiyu Deng, Dr Hailiang Liao, Mr Hao Gong, Dr Mo Qu, Dr Yana Liang, Dr Haoxuan Ding, and Mr Tong Pan. Thanks to you all, I have been able to navigate through the numerous challenging moments on my doctoral journey; without your support, completing my academic pursuits would be very difficult. The carefree and joyful days spent with you in Birmingham are beautiful memories of my doctoral journey in the United Kingdom.

I must express my gratitude to my little companions, Mr Weian Zhou, Miss Hanzhang Zhou, and Miss Xi Han. Despite being miles away in my home country

since the onset of the COVID-19 pandemic, your constant encouragement and care have been a tremendous support, helping me overcome various challenges in my personal and academic life. As I have always said, meeting you all was my good fortune, and my life became much brighter due to your presence.

I would also like to express my deep appreciation to my father, Mr Jinjiang Shi, and my mother, Mrs Jie Fang; thank you all for the unconditional love, care, and guidance you have provided me throughout. Your unwavering support has given me a sense of emotional stability, allowing me to focus on my studies and work without distraction. You fill my days with love and warmth; the thought of it never fails to move me deeply.

Finally, I want to extend gratitude to myself, though it may not be a common practice in the graduation thesis. I appreciate my perseverance in facing various setbacks on the doctoral journey. Thanks for staying committed and not giving up. I am grateful for the countless nights I spent working until the early of the day, for maintaining a youthful mindset, and for the spirit of striving and advancing that I have never let go.

List of publications

- Dashtbozorg, B., **Shi, F***., Tagliaferro, A., Abela, S., Falticeanu, L., Dong, H., (2024). Plasma defect-engineering of bulk oxygen-deficient zirconia. Acta Materialia 262, 119457.

  Contributions: (Conceptualization: Supporting; Data curation: Lead; Formal analysis: Equal; Investigation: Lead; Methodology: Supporting; Validation: Equal; Writing –original draft: Lead; Writing – review & editing: Equal).

- **Shi, F**., Dashtbozorg, B*., Li, X., Dong, H., (2024). Processing conditions and mechanisms for the plasma defect-engineering of bulk oxygen-deficient zirconia. Journal of Materials Research and Technology, Volume 29, March–April 2024, Pages 3759-3770.

  Contributions: (Conceptualization: equal; Data curation: Lead; Formal analysis: Equal; Investigation: Lead; Methodology: Supporting; Validation: Equal; Writing – original draft: Lead; Writing – review & editing: Equal).

- **Shi, F.**, Dashtbozorg**,** B*., Li, X., Dong, H., (2024). Plasma-defect engineering induced crack-healing of zirconia. Scripta Material, submitted.

  Contributions: (Conceptualization: equal; Data curation: Lead; Formal analysis: Lead; Investigation: Lead; Methodology: Supporting; Validation: Supporting; Writing – original draft: Lead; Writing – review & editing: Lead).

  * Corresponding author.

Contents

List of Figures

List of Tables

Chapter 1 Introduction

Zirconia is a versatile material known for its high hardness, exceptional fracture toughness, excellent wear resistance, and good heat insulation properties. It has found a wide range of applications as a refractory material, biomedical implant material, and for various industrial devices in the last century [1-3]. Introducing metal oxides dopants, such as CaO, MgO, or Y_2O_3, into zirconia can stabilise the high-temperature tetragonal (T) and cubic (C) phases, even at room temperature [4]. This advancement has significantly enhanced the properties and performance of zirconia and further expanded its range of applications [5, 6].

As oxygen-deficient zirconia (ZrO_{2-a}) is regarded as a promising material for light absorption and photocatalytic applications, it has recently been the subject of some high-quality studies [7-15]. The desirable photocatalytic properties of these metal oxides photocatalytic materials are related to the abundance of oxygen vacancies introduced into the material by defect engineering [8, 15]. This approach has widened the application range and potential value of black oxygen-deficient zirconia (ZrO_{2-a}) for future energy harvesting, hydrogen generation, decomposition of pollutants, and tumour therapy uses [7, 9, 14, 16] (This paragraph was adapted from the work previously published in Acta Materialia (Vol 262, 119457) [12]).

Each of these methods offers alternative pathways to reduce the bandgap of zirconia and improve its photocatalysis property. Nonetheless, the current approaches to produce blackened zirconia are marked by inherent drawbacks. These include prolonged production cycles, the utilisation of dangerous chemical reagents, suboptimal efficiency, elevated energy consumption, and environmental concerns [13-15, 17]. Moreover, most zirconia materials generated through these methods exist in

the form of powders, nanotubes or disks. This can create significant barriers to the use of dense oxygen-deficient zirconia in future industrial applications. Furthermore, many of the approaches involve demanding processing conditions such as high pressures and temperatures or the use of strong reducing agents (e.g., acids), thereby creating environmental concerns about their safe usage and proper disposal if such methods were to be upscaled (This paragraph incorporates work previously published in Journal of Materials Research and Technology (Vol 29, Pages 3759-3770) [18]).

Low-pressure DC plasma treatments, typically employed for surface modifications of metallic materials [19-21], involve the applications of a potential difference across physically separated anode and cathode electrodes. In the context of low-pressure DC plasma treatments, this potential difference induces the creation of a conductive medium (plasma), thus completing the circuit between the electrodes. The positive ions of the plasma are accelerated towards the cathode while the free electrons move towards the anode [22]. As the plasma medium can carry the charge between the cathode and anode, low-pressure DC plasma treatments represent a distinctive form of electrochemical treatment with no need for a physical connection between the electrodes. Therefore, low-pressure DC plasma treatments can be considered a unique way that has the potential to bulk-reduce zirconia materials under certain conditions (such as pressure, temperature, gas mixture, and voltage) [23, 24] (This paragraph incorporates work previously published in Journal of Materials Research and Technology (Vol 29, Pages 3759-3770) [18]).

Therefore, this PhD project aimed to investigate the feasibility and transformation mechanism for plasma-induced blackening of zirconia and to illustrate the resulting change in properties and potential applications.

The specific research objectives were:

To investigate the potential of low-pressure plasma technologies to produce blackened oxygen-deficient zirconia. This has been explored using both DC and active-screen plasma treatments with different treatment configurations and contact conditions between the sample and the cathode worktable.

To study the mechanism involved in plasma-induced zirconia blackening by controlling different treatment parameters such as voltage, temperature, duration, gas composition, and gas pressure.

To characterise the microstructure and optical properties of plasma-induced oxygen-deficient zirconia (including XRD, Raman, XPS, EPR, SEM, DRS and STA), providing information for understanding the mechanism and laying the groundwork for its potential applications.

To evaluate the change in mechanical properties such as fracture toughness and surface hardness and to explore the potential to induce crack-healing behaviour of plasma-treated zirconia.

A brief overview of the following chapters of this thesis is provided below:

Chapter 2 Literature review of the structure and properties of zirconia, partially stabilised zirconia (PSZ), and oxygen-deficient zirconia (ZrO_{2-a}), as well as fundamental background of plasma treatment technologies.

Chapter 3 The key experimental methods used throughout the whole project, which include sample preparation, plasma treatments, imaging, XRD and Raman scanning.

Chapter 4 Content based on the first published paper (Paper I) with supplementary materials to report the novel plasma defect engineering approach for the formation of

bulk oxygen-deficient zirconia (ZrO_{2-a}) supported by detailed microstructure analysis and optical absorption characteristics.

Chapter 5 Content is based on the second published paper (Paper II) with additional information to report a systematic study of the conditions and the mechanisms for plasma-induced blackening (reduction) of zirconia.

Chapter 6 Complete draft manuscript (based on which a letter paper is to be submitted) devoted to the plasma transformation induced crack-healing phenomena of zirconia and a comparative analysis of the mechanical properties between pristine and plasma-treated zirconia.

Chapter 7 General discussion that coalesces the findings presented across Chapters 4-6 to serve as a complete picture of the research project.

Chapter 8 Comprehensive summary of the key findings of this project and a forward-looking perspective based on current understanding.

Chapter 2 Literature Review

2.1 History and development of zirconia research

As an essential part of the ceramic material family, zirconia is widely used in many fields, including refractory materials, biological implants, dielectric materials and ceramic insulation materials due to its high melting point, high electrical resistivity, low thermal expansion coefficient and excellent mechanical properties [1, 25-27]. The first discovery of this widely recognised polyhedral material can be traced back to 1789 when German chemist Martin Heinrich Klaproth accidentally discovered zirconia while heating a gemstone. Interestingly, the name “zirconium” is inspired by the Arabic word Zargon, meaning the colour of gold, paving the way for zirconia's colourful ceramic status [3, 28, 29]. Due to its excellent metallic lustre, zirconia was initially used for cosmetic purposes in accessories such as earrings, necklaces, and rings. Zirconia was greatly favoured by the public as it was deemed to exude a sense of nobility, similar to diamonds [30-32].

Early research on zirconia primarily centred on its high melting point and chemical stability as a structural ceramic, and therefore garnered limited attention and was primarily employed in industrial devices and as laboratory containers [2, 3]. It was not until 1972 that the ceramic engineering community confirmed the discovery of partially stabilised zirconia (PSZ). By doping with lower valence oxides, such as CaO, MgO, La_2O_3, and Y_2O_3, the high-temperature cubic (C) and tetragonal (T) phases were able to be stabilised at room temperature [4, 5, 33]. On the one hand, this breakthrough significantly enhanced the mechanical performance of zirconia (through the introduction of transformation toughening behaviour) [34, 35]. On the other hand, modifications to the composition of PSZ made it possible to improve its performance

and change its colour by adjusting the doping method, including the types and concentrations of cations incorporated. PSZ has since emerged as a promising engineering material and has received significantly greater research attention [1, 36-38].

As research on zirconia advanced, the distinctive transformation toughening characteristics of the material were uncovered in 1975 [39-41]. It was observed that zirconia, when subjected to external stress, could induce an internal transformation from the tetragonal phase to the monoclinic phase, thereby enhancing its fracture toughness [42, 43]. This series of studies further enhanced the understanding of the mechanical properties of zirconia. In combination with zirconia's high hardness, thermal stability, and biocompatibility, these qualities have made zirconia an ideal biomaterial for implantation. Zirconia-based materials have continued to be widely utilised as dental implant materials since the late 20th century [44, 45].

In recent years, the remarkable advancements observed in the performance of black titanium dioxide (TiO_{2-x}), particularly in terms of enhanced light absorption and photocatalytic behaviour, have sparked substantial interest in the research on oxygen-deficient zirconia (ZrO_{2-a}) [13, 46]. This type of defect engineering involves the introduction of a large number of oxygen vacancies into the crystal structure of zirconia, resulting in the creation of donor energy levels between the conduction and valence bands [47, 48]. As a result, the electronic bandgap of black zirconia is significantly reduced, creating an opportunity for this material's use for photocatalytic and light-absorption applications [49, 50]. This capacity opens up a promising avenue for various metal oxides to play a pivotal role in photocatalysis, facilitating solar-driven water splitting for hydrogen generation and providing alternative approaches to address the escalating concerns surrounding the future energy crisis.

2.2 Structure and properties of zirconia

2.2.1 Crystalline structure of zirconia

Zirconia primarily exists in three crystallographic phases: monoclinic (M), tetragonal (T), and cubic (C). The equilibrium phase diagram of zirconia with varying oxygen content and at different pressures is shown in Figure 2-1.

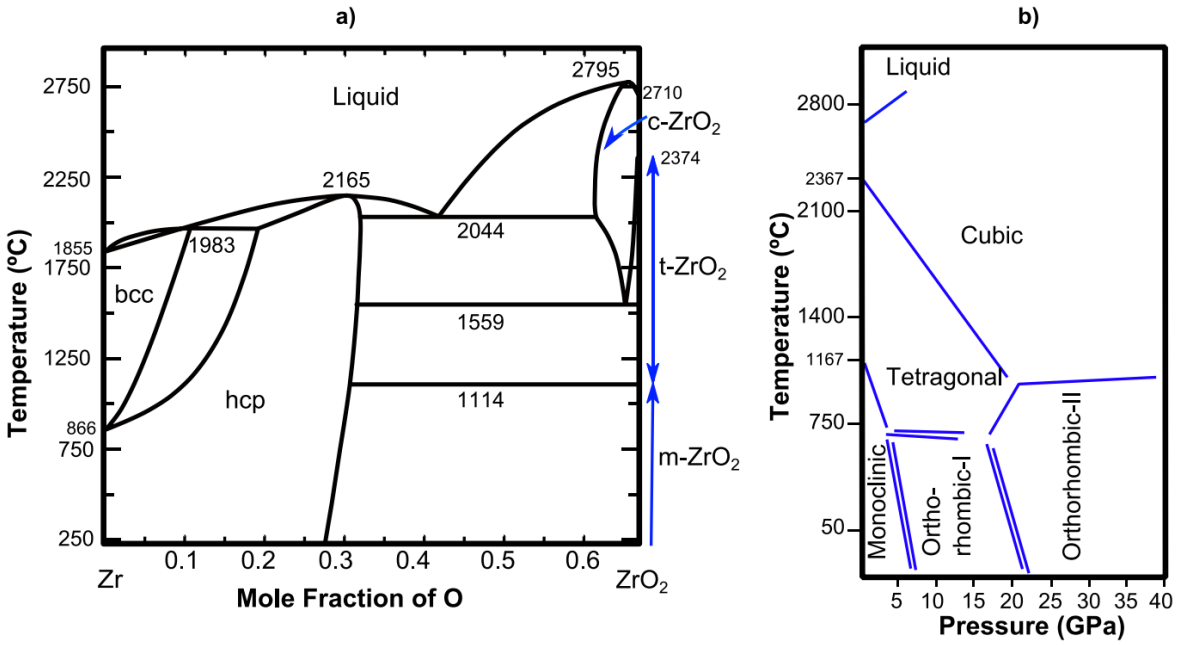

Figure 2-1 (a) Equilibrium phase diagram of the binary system Zr-O at atmospheric pressure. (b) Temperature-pressure phase diagram of pure zirconia [51].

As the most common zirconia phase, the M-phase typically exists between room temperature (RT) and 1170 °C under normal atmospheric pressure [52]. As implied by the name, the crystal lattice exhibits monoclinic symmetry, and its unit cell has different dimensions along the different orientations [53]. Additionally, in the M-phase, each zirconium cation is coordinated with only 7 oxygen atoms, resulting in a lower lattice density of 5.83 (mg/m^3) compared to the other two phases [54]. Due to its irregular structural nature, the crystal lattice of monoclinic zirconia often exhibits the relatively low mechanical properties and fragile reliability of pure monoclinic zirconia

demonstrates. Moreover, under high-temperature and/or high-pressure, the M-phase zirconia readily transforms to either the T, C and orthorhombic I phase and has the potential to lead to component failure, thus limiting the industrial and biomedical applications of monoclinic zirconia [52, 55].

As one of the typical high-temperature zirconia phases, the T-phase of zirconia exists within the temperature range of 1170 °C and 2370 °C, and possesses tetragonal symmetry [41, 53]. In this crystal structure, the lengths of the a and b lattice parameters are equal, both measuring 3.64 Å, while the length of the c-axis is larger at 5.27 Å, and its lattice density is 6.10 (mg/m^3) [56]. Within the T-phase, each zirconium atom is surrounded by eight oxygen atoms, classifying its structure as a body-centred tetragonal lattice, which imparts a degree of mechanical stability. Usually, the T-phase cannot be retained at room temperature (RT), even with rapid quenching [55]. However, it is possible to maintain the T-phase at RT with the introduction of various stabilisers and further enhancing the mechanical performance of zirconia, as will be detailed in the following chapters.

The C phase is another high-temperature zirconia phase, typically found at temperatures ranging between 2370 °C and 2680 °C [53]. This phase is not commonly found in nature, but can be stabilised (like the T phase) through the addition of stabilisers. The unit cell forms a perfect cube in this phase, exhibiting cubic symmetry. All three crystal axes are entirely equal, measuring 5.12 Å, and the unit cell density is 6.09 (mg/m^3) [56]. It's worth mentioning that stabilised cubic zirconia often exhibits high light-transmitting properties, unlike the tetragonal and monoclinic phases, which are typically white [55]. This transparency makes it an ideal choice for various applications. Due to its excellent hardness and chemical stability, it is widely used in synthetic jewellery and has become a popular alternative to diamond. A table (listed

below) has been compiled containing information on the three typical zirconia phases and their key lattice parameters.

Table 2-1. Summary of the structural characteristics of ZrO2 phases at the atmospheric pressure.

ZrO_2 phase	Space group	Lattice parameters (Å)	Zr coordination number	Density (Mg/m^3)
M	$P2_1/c$	a=5.16, b=5.19, c=5.30	7	5.83
T	$P4_2/nmc$	a=b=3.64, c=5.27	8	6.10
C	Fm3m	a=5.12	8	6.09

When subjected to high pressures, the M-phase of zirconia can undergo two phase transitions: above 750 °C, the M-phase transforms into the T phase, while below 750°C, it transforms into the orthorhombic phase 1 (O1) [56-58]. The pressure requirements for the M-O1 transition decrease as the temperature increases: at RT, the transition requires a pressure of 7.5 GPa, whereas, at temperatures near 750 °C, the pressure requirement decreases to only 3.75 GPa, approximately half the pressure needed at RT. If the environmental pressure rises to 22.5 GPa at room temperature, zirconia undergoes two transitions to the orthorhombic phases 2 (O2) [57]. It's worth noting that the O2 phase is the only one in zirconia that has the potential to transform directly into the T and C phases. While the O1 and O2 phases are not very common, their existence enriches the research background of zirconia, providing a foundation for understanding zirconia's phase transitions and mechanical properties at different temperatures. Moreover, they are significant for the development of specific zirconia-based materials for tailored applications.

In addition, a diagram showing the three normal phase transformations of zirconia is shown below (Figure 2-2). Due to the disparity in density between the M and T phases of zirconia, a significant volume change occurs during the phase transition from M to T, resulting in a volumetric contraction of approximately 3-4% [58, 59]. Conversely, a volume expansion of approximately 5% occurs during the phase transition from T to M [60]. This phenomenon first leads to the development of microcracks within the material, and ultimately leads to macroscopic cracking and total material failure.

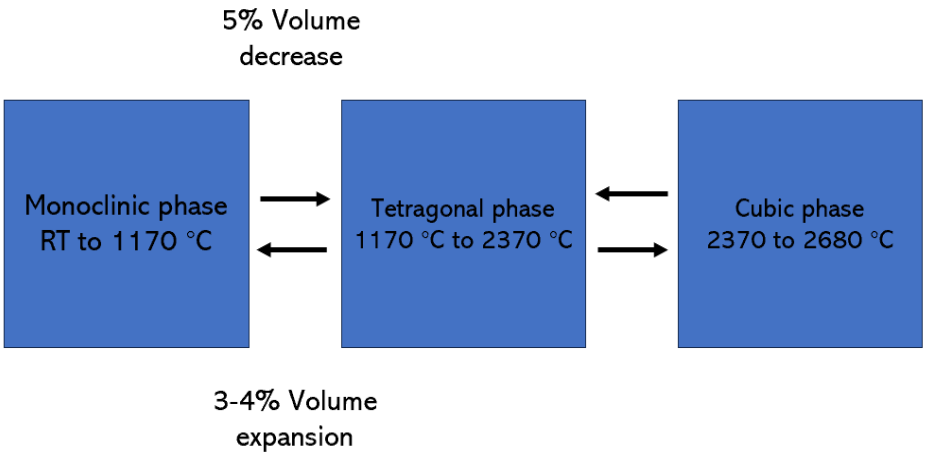

Figure 2-2 Temperature-related phase transformation of zirconia (adapted from [1]).

2.2.2 PSZ (partially stabilised zirconia)

To overcome the mechanical limitations of the M-phase in zirconia, researchers have discovered that doping with metal oxides can stabilise the high-temperature phases of zirconia at room temperature [4, 61]. Partially stabilised zirconia (PSZ) ceramics typically exhibit a biphasic organisational structure that is characterised by the coexistence of cubic ZrO_2 (C phase) and a portion of tetragonal ZrO_2 (T phase) [4, 5, 62]. The recognition of the "absorption of energy" during the room temperature T to M phase transformation in zirconia was identified as a strengthening mechanism as early as 1975 [63]. Unlike the stable C-phase, the T-phase is metastable and can undergo a martensitic transformation to form the M-phase under the influence of external force,

and therefore can contribute to the development of toughening behaviour in the material (to be further discussed in Section 2.2.3).

In these partially stabilised ceramics, intragranular precipitates of T-ZrO_2 exist within a matrix of stabilised C-ZrO_2. Commonly used dopant elements include Mg, Ca, Sc, Y, and Nd. Mg and Y are the most frequently employed, typically in concentrations (2%-8%) lower than those required for full C-ZrO_2 stabilisation [34, 63, 64]. These materials intentionally avoid achieving complete stabilisation, and thus give rise to the term "partially stabilised zirconia" or PSZ, often with the relevant dopant appended to the name (e.g., Ca-PSZ, Mg-PSZ, Y-PSZ) [62].

The primary method currently employed for the successful manufacture of bulk PSZ materials is high-temperature sintering. This process involves the uniform mixing of powdered zirconia with stabiliser powder, followed by sintering of the mixture at elevated temperatures to form bulk PSZ [61, 65, 66]. The primary method currently employed for the successful manufacture of bulk PSZ materials is high-temperature sintering. This process involves the uniform mixing of powdered zirconia with stabiliser powder, followed by sintering of the mixture at elevated temperatures to form bulk PSZ [67]. This phase transition has left a disastrous mark in the history of YSZ applications, with some medical Y-TZPs remembered as catastrophic failures due to spontaneous fractures [68, 69]. Numerous studies have attributed the main source of failure to the concentration of Y^{3+} ions around cubic grains after sintering at 1500 °C, which differs from the nearly homogeneous distribution of Y^{3+} ions when sintered at 1300 °C. [68, 70, 71]. Where the Y^{3+} ions are segregated, the cubic phase starts to form from grain boundaries and triple junctions. The enrichment of cubic grains with Y^{3+} ions leads to nearby yttrium-depleted regions, and therefore creates less stable tetragonal grains and acts as nucleation sites for the (t → m) transformation [5, 71].

Furthermore, depending on the ratio of stabiliser doping, there are numerous PSZ variations, each possessing distinct physicochemical properties and corresponding applications [72, 73]. Using the dopant Y_2O_3 as an example, two prevalent types of zirconia emerge with different amounts of stabiliser: 3YSZ (97 mol% ZrO_2 3 mol% Y_2O_3) and 8YSZ (92 mol% ZrO_2 8 mol% Y_2O_3). The primary phases in zirconia for these two types are the T-phase (milky white) and the C-phase (transparent), respectively. Among PSZ variants, 3YSZ has been demonstrated to possess outstanding mechanical properties and is primarily employed in cutting tools, biomedical implants and electrons of SOFC (Solid oxides fuel cells). Conversely, 8YSZ, owing to its remarkable enhancements in ionic conductivity and high-temperature resistance compared to pure zirconia, enjoys widespread utilisation in fuel cell electrolyte materials, turbine blades, and bullet-proof ceramics [74, 75]. The variety of properties achievable has led to the widespread use of partially stabilised zirconia as both engineering ceramics and biomedical materials. As the core material of this project, the relevant values of 3YSZ have been summarised and incorporated into the following table as a groundwork for the subsequent studies.

Table 2-2. Summary of the Key Performance Characteristics for 3YSZ.

	Average crystallite size (nm)	Vickers hardness (GPa)	Indentation fracture toughness (MPa $m^{1/2}$)	Density (g cm^{-3})	Young's modulus (Gpa)	Conductivity (at 700 °C) Ω^{-1} cm^{-1}
3YSZ	41	12.7	5.8	5.9	217.46 ± 20	0.0037

Depending on the varying charges of the doping ions, partially stabilised zirconia also demonstrates distinct properties and stability. It is well-known that Zr ions are generally tetravalent. When dopant cations are also tetravalent, such as Ce^{4+} and Ge^{4+}, they replace Zr^{4+} ions in a one-to-one ratio while maintaining charge neutrality and not generating oxygen vacancies or free electrons [76-78]. However, as the ionic radii of the dopant metal ions differ, PSZ is still found to exhibit different lattice distortions and residual stress. The situation becomes more complex when the dopant metal ions are trivalent, such as Y^{3+}, Ga^{3+}, and Gd^{3+}. Figure 2-3 illustrates the doping process using Y^{3+} and cubic zirconia crystalline as an example. Two Y^{3+} ions occupies two original Zr^{4+} ion position, and to maintain charge neutrality, one oxygen vacancy is generated in response to the Y^{3+} ions. The ionic radius of Y^{3+} is also larger than that of Zr^{4+} and leads to lattice distortion and compressive stress generation after entering the zirconia lattice. Many studies have shown that this distortion effectively counteracts the tendency of zirconia to undergo T-M phase transitions in response to external forces, thereby maintaining lattice stability [79-82]. Another method involves co-doping trivalent and pentavalent metal ions, such as Y^{3+} and Nb^{5+}. The resulting PSZ is found to exhibit superior thermal insulation properties and greater stability than traditionally doped PSZ [83, 84].

Another necessary consequence of the zirconia stabilisation with aliovalent cations, particularly trivalent cations like Y^{3+}, is the production of oxygen ion vacancies in the zirconia lattice. At high temperatures, oxygen ions diffuse through the vacancies, generating new vacancies and producing solid electrolytes with oxygen ion conductivity. The ionic conductivity strongly depends on the amount of oxygen vacancies in the materials, which is controlled by the dopant concentration.

In recent studies, it has been suggested that future investigations will primarily concentrate on three key aspects. Firstly, given that many stabilisers are relatively costly, a primary research focus is on cost reduction to facilitate large-scale production. Secondly, enhancing the resistance of partially stable zirconia to low-temperature degradation to improve its reliability and stability as a biomedical implant. Thirdly, while maintaining the fundamental physicochemical properties, improving the electronic conductivity of PSZ to expand its applications in electrochemical devices such as fuel cells [5].

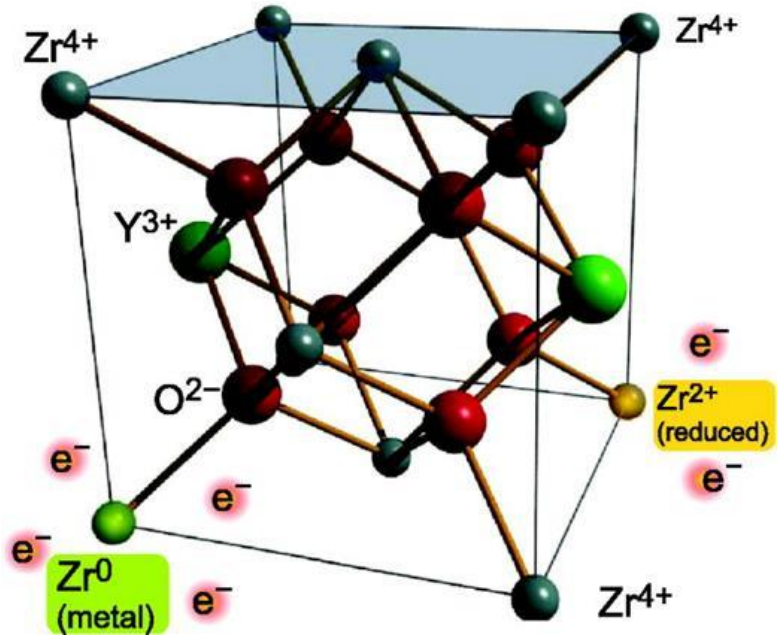

Figure 2-3 Schematic diagram of yttrium-stabilised cubic phase zirconia crystal structure [85].

2.2.3 Transformation toughening

As mentioned in Section 2.2.1, the practical applications of pure M-phase zirconia are limited due to the inability to produce solid M-phase zirconia components. This catastrophic failure of pure zirconia components arises from the volume expansion of the material in the T-M phase transition when cooling down, which introduces cracks

throughout the material that break the solid component into powder. Therefore, stabilising the tetragonal and cubic phases at RT and preventing phase transformation during cooling is crucial for utilising zirconia in industrial applications. The concept of "Transformation Toughening" in ZrO_2 was initially introduced in a paper titled "Ceramic Steel?" by Garvie, Hannink, and Pascoe [63]. The deliberate choice of this title aims to underscore the similarities between ZrO_2-based alloys and steel alloys. This comparison develops as both systems undergo martensitic transformations at relatively low temperatures. Similar to the formation of martensite in steels, the T ⟶ M-phase transformation in ZrO_2 can be leveraged to enhance the strength and fracture toughness of zirconia by modifying the compositions to control the microstructure [86].

Transformation toughening is especially effective in zirconia material that contains metastable tetragonal phase (t-phase) zirconia particles that are evenly distributed within a matrix. This matrix could consist of cubic zirconia in the case of PSZ, or other ceramic phases such as Al_2O_3 [86]. When subjected to high stress concentrations of stress, such as those near crack tips, the t-phase particles tend to undergo martensitic transformmation to the monoclinic phase. This transformation results in volume expansion, generating a compressive stress field around the particles. This compressive stress impedes crack propagation and may even lead to crack closure, thereby enhancing the material's mechanical toughness as demostrated in Figure 2-4. The degree to which toughness is improved relies on a multitude of factors. Among these, the transformation potential of the metastable tetragonal particles plays a crucial role, which is intricately linked to their size and structure [87]. Additionally, the structure of the matrix is a pivotal determinant, and it is influenced by various factors such as the type and concentration of the stabiliser, particle size, presence of residual

impurities in the precursor zirconia, and precise temperature control throughout processing stages like heating, sintering, and cooling [5, 63, 88].

The stabilisation of zirconia has two significant effects on its physical properties. Firstly, it greatly enhances the toughness of zirconia ceramics with specific microstructures. Secondly, it improves the oxygen ion conductivity of zirconia ceramics at high temperatures [44]. The same martensitic transformation from tetragonal to monoclinic phase, which degrades the mechanical properties of pure zirconia, actually leads to a significant improvement in the mechanical properties of stabilised zirconia. Stabilising metastable phases of zirconia at room temperature has opened up a plethora of engineering applications. Partially stabilised zirconia, owing to its exceptional mechanical properties and unique functional behavior, has emerged as one of the most vital industrial ceramic materials for advanced structural and functional applications [44].

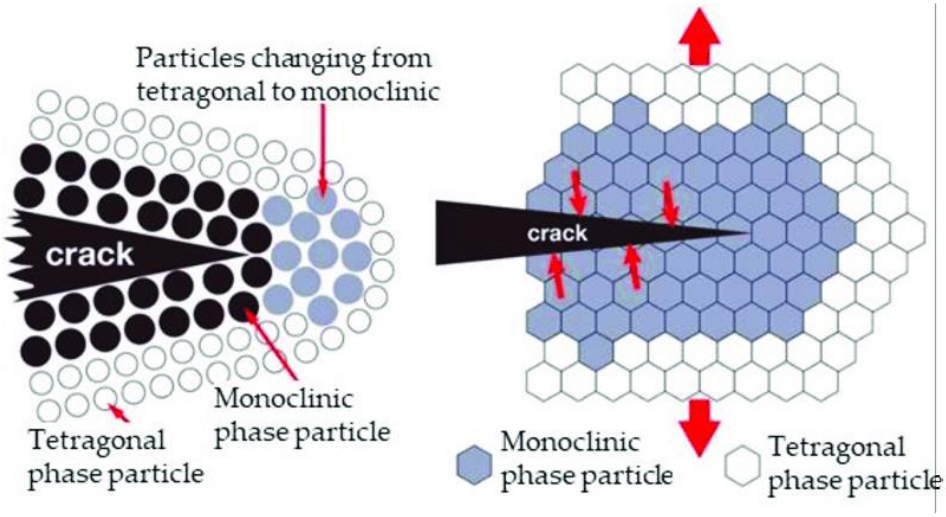

Figure 2-4 Process of fracture toughening promoted by t ⟶ m martensitic phase transformation induced by an external stress resulting from crack propagation in a PSZ material [89].

2.3 Black zirconia

The black zirconia encompasses two distinct types: oxygen-deficient zirconia and aesthetically coloured zirconia. They are often confused since they both appear black, leading to the assumption that they are of the same type. However, it is crucial to note that they possess intrinsic differences: aesthetically coloured zirconia typically involves the addition of a colouring agent to zirconia without any structural changes occurring, it can still be written as ZrO_2. Meanwhile, oxygen-deficient zirconia has an insufficient oxygen content, hence it can be denoted as (ZrO_{2-a}). Additionally, this chapter will also delve into the general characterisation methods of oxygen-deficient zirconia, which holds practical significance in distinguishing between ZrO_{2-a} and coloured zirconia as experimental products.

2.3.1 Aesthetically coloured zirconia

As a widely form of commercial zirconia, stained zirconia holds a significant position in the jewellery, ceramic and watch industries. Leveraging its inherent excellent mechanical performance and chemical stability, stained zirconia achieves a wide range of colours by utilising specialised dyeing processes, typically involving the incorporation of different rare earth elements such as yttrium, erbium, and cerium [90]. The colour range is extensive, encompassing blue, green, red, and black [91-93].

Interestingly, the colours of the commonly encountered 3 wt% yttria-stabilised zirconia (3YSZ) and 4 wt% yttria-stabilised zirconia (4YSZ) predominantly appear milky white. However, as the yttrium (Y) content increases to around 8-10 wt%, researchers have observed a transformation in the partially stabilised high-temperature phases of YSZ, in which the primary high-temperature phase shifts from the tetragonal phase to the cubic phase [67]. The most conspicuous change resulting from this transformation is

a gradual transition in the colour of the zirconia body from milky white to transparent, exhibiting considerable translucency around a Y content of 10 wt% [94-96]. Zirconia has a relatively lower cost, good mechanical properties and translucency as compared with diamond. Therefore, zirconia has served as a noteworthy alternative to diamonds in the jewellery industry for a long time. Additionally, its chemical stability, as opposed to traditional gemstones, makes it resistant to corrosion and discolouration, enhancing the durability of jewellery and making zirconia a significant choice in producing numerous high-end products [2, 97, 98].

2.3.2 Oxygen-deficient zirconia (ZrO_{2-a})

Oxygen-deficient zirconia, as the name suggests, refers to zirconium oxide crystals with an insufficient oxygen content within the crystal lattice. The relationships in the zirconium-oxygen system were first in detail reported around 1954 (possibly even earlier, but the earliest report found through literature indexing is from 1954) by R. F. Domagala [99]. He initially constructed a binary phase diagram from zirconium to zirconium dioxide by arc melting and heat treating zirconium iodide. He found that Oxygen additions to zirconium raise the transformation temperature as well as the melting point. Subsequently, the phase diagram of the oxygen-zirconium system was further refined around 1961 through the work of Aronson [100]. He fully investigated the efficiency of oxygen-deficient zirconia to fully re-oxidise at different temperatures and pressures.

However, many researchers believe that the attention to the oxygen-deficient zirconia (ZrO_{2-a}) study was influenced by the significant improvement in the photocatalytic performance of oxygen-deficient titania (TiO_{2-x}) [13, 14]. Since the introduction of titania (TiO_2) for photocatalysis in 1972, various semiconductors have been employed

for photocatalytic water splitting, with TiO_2 remaining one of the most effective photocatalysts [101, 102]. Although zirconia's electronic bandgap exceeds 5 eV, which generally precludes its use as a photocatalyst, its value as an irreplaceable vital metal oxide within the same group as TiO_2 in the periodic table has already been proven by its significance for material coatings, sensors, energy conversion, and biomedical applications. Moreover, the introduction of oxygen vacancies in metal oxides is widely recognised as a method for producing low-bandgap photocatalysts [103-105]. As the approaches for introducing oxygen vacancies into metal oxides became increasingly mature since 2000, there was a growing interest in reducing the bandgap of zirconia. This material is now being widely explored for its potential applications in photocatalysis. Researchers have gradually begun to explore various feasible methods for the active synthesis of different types of deoxidised zirconia.

Zu et al. [17] obtained oxygen-deficient zirconia through a process of molten lithium reduction, involving heating, washing, and sonication (described in further detail in Section 2.2.3). The resulting oxygen-deficient zirconia powder exhibited a characteristic black colour, as shown in Figure 2-5. The XRD patterns of their black zirconia and pristine zirconia share the same characteristic peaks, with no discernible presence of secondary phases or impurities, which aligns with various studies [12-15]. Zu et al. [17] also claimed that the grain size of black zirconia obtained through molten lithium reduction was slightly increased, which is inconsistent with most studies. Grain size reduction has also been reported during the formation of black zirconia. The magnesium-thermal reduction strategy demonstrated in the study by Sinhamahapatra et al. [13] revealed a smaller grain size in oxygen-deficient zirconia, as compared with the untreated material. Another example of grain size reduction following the formation of oxygen-deficient zirconia is the Wang et al. study, which utilised a high-pressure

torsion method to modify zirconia [15]. Although differing grain size changes were reported, all of the studies were in agreement with the development of lattice distortion in black zirconia, which has been attributed to the formation of oxygen vacancies in the material.

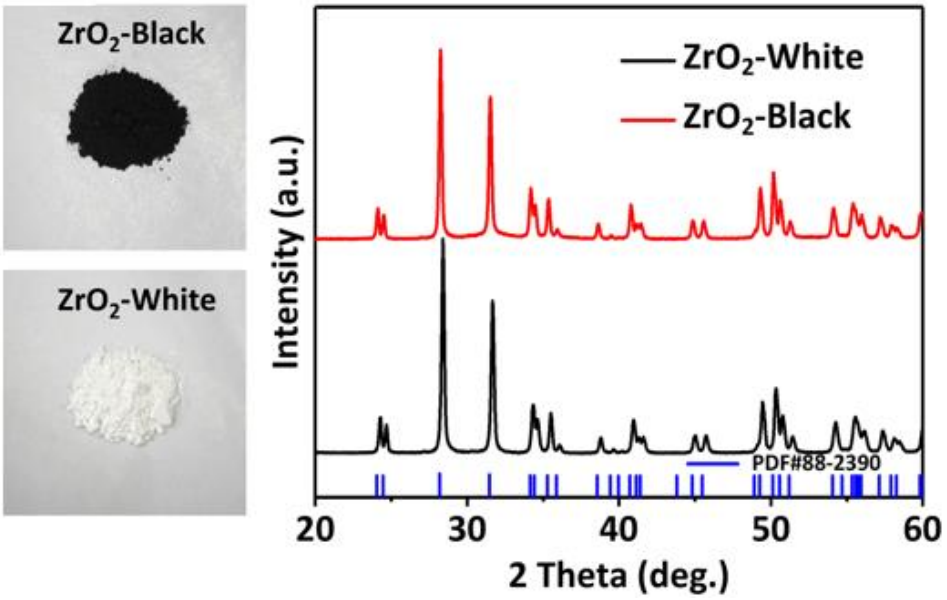

Figure 2-5 Photograph of the white and black samples indicating the colour and XRD patterns [17].

2.3.2.1 Characterisation of ZrO_{2-a}

The key focus for determining whether black zirconia synthesised under various laboratory conditions can be classed as an oxygen-deficient form, which has the potential to be used for certain photocatalytic applications, lies in the identification of the presence of oxygen vacancies within its lattice.

Since the concept of oxygen vacancies (OVs) was first introduced in 1960, it has been continually studied in areas involving gases in contact with solid surfaces [106]. It wasn't until 2000 that researchers, utilising theoretical calculations and experimental characterisations, gradually discovered that oxygen vacancies might be one of the

most reactive sites on metal oxides' surfaces and that oxygen vacancies can alter its crystalline structure and modify the electronic and chemical properties of the surface [107-110]. Subsequent extensive research has also demonstrated the significant promoting effect of oxygen vacancies on the photocatalytic performance of metal oxides [111-113]. This primarily results in the broadening of the absorption spectrum and narrowing of the bandgap of the metal oxide. These changes in performance are attributed to the formation of structural defects, which can reduce the total bandgap value of the metal oxide by introducing impurity bands within the gap. It is worth noting that when oxygen atoms are removed from a material (creating vacancies), it introduces a charge imbalance in the crystal lattice. In response to the charge imbalance caused by the oxygen vacancies, electrons (or sometimes other charge carriers) within the material move to new energy levels that emerge within the bandgap. These energy levels are often referred to as mid-gap levels because they are located between the valence and conduction bands. By occupying these mid-gap energy levels, it will balance the charge disparity caused by the absence of oxygen atoms [104, 105].

The characterisation methods for oxygen vacancies are diverse. Currently confirmed effective methods include electron paramagnetic resonance (EPR), X-ray absorption fine structure (XAFS), positron annihilation lifetime spectroscopy (PALS), X-ray photoelectron spectroscopy (XPS), Raman spectroscopy, high-resolution SEM and TEM, and thermogravimetric analysis (TG) [114]. Based on current research, most of the oxygen vacancy characterisation methods are still qualitative (i.e., capable of distinguishing between the presence and absence of oxygen vacancies). Quantitative methods that allow for the rapid identification of the position, amount and defect types of oxygen vacancies still need to be developed further [114].

The majority of the current research on the characterisations of oxygen-deficient zirconia remains relatively limited, primarily involving qualitative analyses to infer the presence and estimate the quantity of oxygen vacancies. For instance, in thermogravimetric analysis, heating oxygen-deficient zirconia under oxygen conditions may result in re-filling oxygen vacancies, especially at high temperatures [115]. This difference in mass can be detected through TGA. In a study conducted at a heating rate of 10 °C/min under air conditions for both black (oxygen-deficient zirconia) and white zirconia (pristine zirconia), it was observed that the mass of oxygen-deficient zirconia began to significantly increase around 200 °C, reaching its peak at 300 °C, exceeding the weight percentage of pristine zirconia in the same temperature (same heating stage) by 1.5% [13]. The researcher claimed this increase was due to the re-filling of oxygen vacancies in the oxygen-deficient zirconia, a perspective corroborated by similar studies [12, 115].

Furthermore, EPR is employed as a technique to ascertain unpaired electron spins in materials. In the case of pure monoclinic zirconia, the EPR spectrum of oxygen-deficient zirconia is commonly identified with a distinct signal at approximately $g = 2.002$, with a minor peak at $g = 1.977$, corresponding to oxygen vacancy and Zr^{3+}, respectively, while the pristine sample is not found to exhibit any significant EPR signal [13, 50, 116]. However, for partially stabilised zirconia, such as YSZ, the mere presence of dopant atoms introduces a non-negligible quantity of oxygen vacancies. If oxygen-deficient zirconia is synthesised from partially stabilised zirconia, the EPR analysis will become considerably more complex, as compared to pure M-phase zirconia [12, 14].

2.3.2.2 Properties and applications of ZrO_{2-a}

The emergence of oxygen-deficient zirconia has created many potential opportunities in various fields, such as photocatalysis, pollution degradation, and tumour therapy [7, 9, 13, 16]. Its application value comes from the change intrinsic change in properties of oxygen-deficient zirconia. The most direct enhancement is found in the light absorption behaviour of ZrO_{2-a}. Studies on the Ultraviolet-Visible-Near Infrared (UV-VIS-NIR) reflection spectra (200-1400 nm) of oxygen-deficient zirconia reveal impressive results [15, 17, 117]. Owing to the wide bandgap (above 5.0 eV) of pristine zirconia (white zirconia), strong absorption is only found in the short-wave ultraviolet region (<280nm), while relatively weak absorption occurs in the remaining spectrum. In contrast, oxygen-deficient zirconia (black zirconia) demonstrates increased light absorption across the entire spectrum, particularly in the visible and near-infrared regions, as illustrated in Figure 2-6a [17].

In addition to the studies on the band structure of oxygen-deficient zirconia, experiments on the photocatalytic hydrogen evolution activity more intuitively demonstrate its potential as an energy material [117-120]. Figure 2-6b illustrates a typical time course of hydrogen generation in the full solar spectrum [17]. Results from the study by Zu et al. [17] indicated that the hydrogen-evolving capacity of oxygen-deficient zirconia increased by approximately five times from the untreated material, a relatively uncommon phenomenon in hydrogen catalytic materials. In agreement, the study by Sinhamahapatra et al. [13] also shows a similar performance change of pure monoclinic-phase oxygen-deficient zirconia, which is found to exhibit a significant hydrogen-evolving capacity increase, with untreated samples showing limited hydrogen generation [13]. In studies involving partially stabilised zirconia as experimental samples, the hydrogen-evolving capacity of oxygen-deficient zirconia is generally 3-6 times greater than that of untreated samples [14-16].

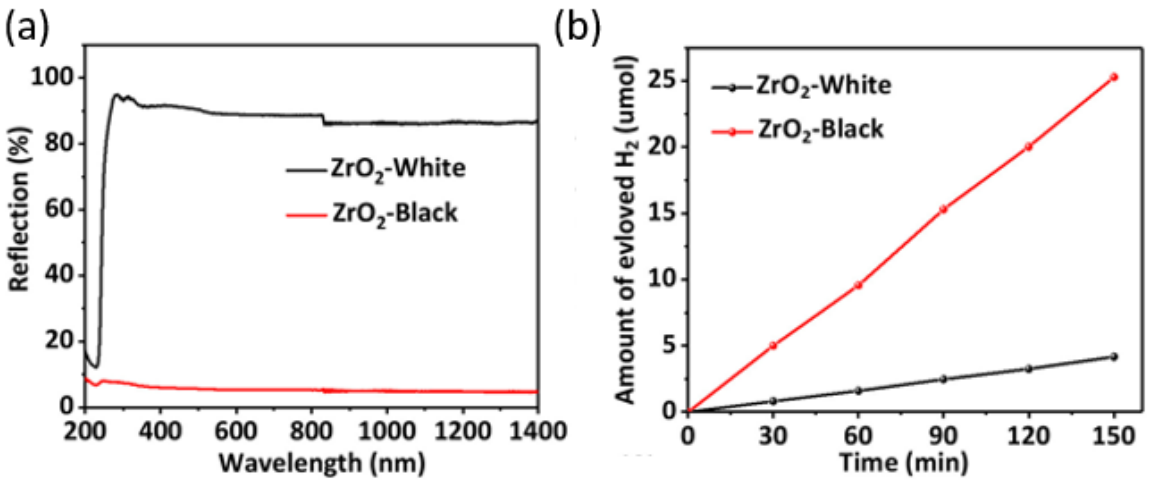

Figure 2-6 (a) UV–Vis-NIR diffuse reflectance and the (b) photocatalytic hydrogen generation of white ZrO_2 and black ZrO_2 nanoparticles [17].

In addition, another noteworthy performance enhancement in oxygen-deficient zirconia (black zirconia) is the increase in electrical conductivity [15]. An in-depth analysis of the change in conductivity was performed in a study from Ana, and in addition to the change in colour (shown to be able to go from white to black and back to white again), and found that black (anoxic) zirconia has elevated conductivity. This was obtained by simultaneously observing the current values while applying a voltage of 50 V to the zirconia poles. When DC-reduction started, a current of more than 650 mA was observed for oxygen-deficient zirconia, while no current signal was observed for untreated zirconia under the same conditions [121]. More importantly, the deoxygenation (reduction) process has been found to be rapid and reversible under certain conditions, such as flash sintering [122, 123], and the electrical conductivity of black zirconia (reduced) is observed to significantly differ from that of white (unreduced) zirconia. Currently widely used as electrode materials for SOFC are YSZ (both 8YSZ and 3YSZ), which can also appear as solid electrolytes. Given that oxygen-deficient zirconia was shown to have a more active conductivity than YSZ, it is believed that it also has some potential in the SOFC domain in the future, as well as a sensor for

oxygen or humidity, and as a high-temperature material [123-130]. However, demonstrations of the potential of oxygen-deficient zirconia for these applications are predominantly at the laboratory testing stage, and the feasibility and scalability from theory to practice require broader and more in-depth research.

2.3.2.3 Manufacture of ZrO_{2-a}

Given the immense potential of oxygen-deficient zirconia across various fields, research on the synthesis routes has seen attracted significant interest in recent years. However, to fully exploit the superior performance of oxygen-deficient zirconia, the primary consideration is the selection and optimisation of manufacture. This relates to the crystalline structure and basic physical properties of the produced oxygen-deficient zirconia and directly influences its performance for application. Table 2-3 summarises the primary reported and notable synthesis methods, providing outlaying information on the raw materials, manufacture steps, reaction conditions, cycles, treatment/total (treatment + post-processing) duration and products of each published approach. These details can assist researchers in gaining a better understanding of various methods for preparing and serving as valuable references for future studies, fostering continuous exploration and innovation in this field, especially as no published reviews have been reported on this topic thus far.

Based on current research, many methods can successfully synthesise oxygen-deficient zirconia, demonstrating improved performance in various fields. However, most of these methods have significant limitations, including long production cycles, use of hazardous chemical reagents, low efficiency, high energy consumption, and environmental concerns (e.g., disposal of chemical reagents). For instance, a significant portion of these methods, especially those primarily based on reduction

processes, involve the use of strong acids (such as hydrochloric acid). Consequently, traditional chemical treatment procedures like impurity removal, residual cation detection, deionised water washing, and ultrasonic cleaning become unavoidable, making synthesising oxygen-deficient zirconia complex. Additionally, most of the reduced black zirconia manufactured under these approaches are in powder form and require sintering into bulk components for applications demanding structural integrity, specific geometries and resistance to mechanical stresses. Re-oxidation is difficult, if not impossible, to avoid when sintering oxygen-deficient zirconia, limiting the use of the material in the powder form. More importantly, many methods demand harsh reaction conditions involving high temperatures, high pressures, or extremely low pressures, which undoubtedly impede the large-scale industrial production of zirconia. Therefore, exploring a more efficient, cost-effective, and environmentally sustainable approach is worth investigating.

Table 2-3. The Main Synthesis Approaches for Black Zirconia (Oxygen-deficient Zirconia).

Treatment method	Raw material	Gas	Temperature (°C)	Pressure (mbar)	Treatment duration (h)	Post-processing procedure	Total duration (h)	Product form	Reference
Magnesiothermic reduction	Monoclinic nano ZrO_2	5% H_2/Ar	650	1013	4	Etch in HCl solution, wash and dry	52	Nanoparticles	[13]
High-pressure torsion	Y_2O_3 powder	Air	26.85-400	$6*10^7$	0.05	-	0.05	Dishes	[14]
Molten lithium reduction	PSZ powder	Ar	400	1013	0.5	Wash with HCl solution, deionised water and ethanol; then ultrasonication and dry.	2	Nanoparticles	[17]
High-pressure spark plasma sintering	8%mol Y_2O_3 powder	Vacuum	1000-1200	39516	0.05	Anneal 4 hours in air	4.05	Disks	[131]
Fe_2O_3 doping	3 & 8 mol% Y_2O_3 power	Air	1150	1013	2	Mix with α-Fe_2O_3 powder, disperse into ethanol, and electrophoretic deposition.	5	Disks	[132]
Ti powder interfacial reaction	8%mol Y_2O_3 powder	Vacuum	1100	$4.9*10^{-6}$	2	Mix with Ti powder and then react it at 1000 °C for 2 h	4.5	Powder	[15]
Electrochemical blackening	12%mol Y_2O_3 powder	Vacuum	800	1013	24	Apply a voltage of 100 V and hold T at 500 °C for 5 h	30	Bulk	[133]

Sol-gel	Zirconium oxychloride oxtahydate solution	Liquid	450	1013	24	Wash with HCl solution, deionised water and ethanol; then ultrasonication and dry.	30	Film	[134]
Silver doping	Tetrapropyl zirconate	Liquid	80	1013	10	Dry in the oven at 100 °C for 12 h and calcine at 600 °C	32	Powder	[117]
DC plasma treatment	3 mol% Y_2O_3 cylindrical sample	100% H_2	500	3	5	-	5	Bulk	[12]

2.4 Plasma & Low-pressure plasma treatment

Given that the primary experimental technique in this project is low-pressure plasma treatment, it is imperative to have a comprehensive understanding of plasma composition with different types; plasma formed in laboratory settings due to the action of electric fields includes formation conditions, maintenance methods, energy propagation processes, as well as various low-pressure plasma treatment setups and their limitations. These three aspects will also serve as the main topics of this chapter.

2.4.1 Plasma

As the fourth state of matter, distinct from gases, liquids, and solids, plasma is a highly ionised state characterised by the loss or gain of electrons by atoms or molecules in gases or materials, forming a gaseous mixture of ions, neutral particles and free electrons [135]. When gases are subjected to high temperatures, strong potentials or strong magnetic fields, free electrons present within the gasses are accelerated. The collision of these accelerated electrons with neutral particles in the gas results in the removal of electrons from the neutral particles, thus forming new free electrons and ionising the neutral particles [136]. The electric field further accelerates the separated free electrons, therefore giving rise to further collisions with neutral species, leading to a cascade of interactions. This cascade effect strongly relies on the initially accelerated (and newly generated) free electrons gaining enough kinetic energy before collisions to be able to ionise the elements/molecules [137]. The formation of positive ions generates an equal amount of negative charge during this process, which ensures that the net charge of negative and positive ions remains consistent at all times, resulting in a charge of zero on a large scale [135]. This is this state referred to by researchers as “plasma”.

This high-energy state is typically generated under elevated temperature conditions through gas discharge, laser radiation, strong electric fields, or intense radiation [138-140]. These harsh conditions make plasma less common in nature than the other three forms of matter (solid, liquid, and gas); their occurrences are typically brief yet captivating, such as lightning (Figure 2-7a) and aurora (Figure 2-7b) phenomena [141, 142]. Each lightning strike, usually lasting less than 1 second, releases currents of up to 30,000 amperes at voltages around 100 million volts. The plasma temperature during a lightning discharge can reach as high as 28,000 K [143, 144]. Auroras, typically observed in high-latitude regions as a celestial phenomenon resulting from the interaction between the earth's atmosphere and solar winds, can be understood as large-scale discharges around the earth [145]. When charged particles from the Sun approach the Earth, the Earth's magnetic field guides a portion of them along magnetic field lines to concentrate at the North and South Poles [146]. As these particles enter the atmosphere, they collide with atoms and molecules, forming plasma and releasing light. Due to the different types of atoms involved in the collisions, auroras exhibit various attractive and distinct colours; for example, oxygen radiation often produces green and reddish-brown colours, while nitrogen radiation tends to appear blue and purple [144].

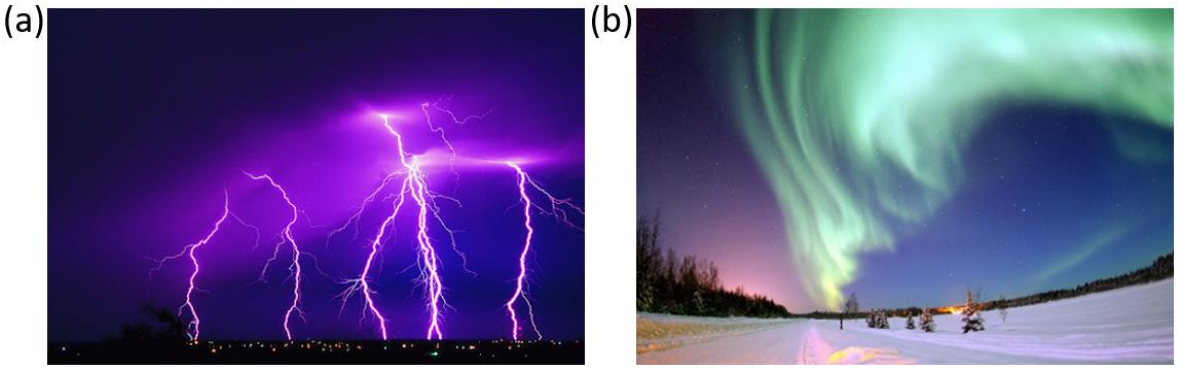

Figure 2-7 Natural plasma in the form of (a) lightning and (b) auroras phenomena.

Compared to the grandeur and magnificence of plasmas in nature, the generation of plasmas under laboratory conditions often necessitates precise control. To sustainably and reliably generate and maintain plasma, numerous environmental parameters such as temperature, pressure, power, and gas mixture must be carefully controlled. Depending on the working gas pressures, laboratory-generated plasmas are typically categorised into two broad types, atmospheric-pressure plasmas and low-pressure plasmas [143].

Under atmospheric pressure, the arc generated by the lab condition is a good example, as shown in Figure 2-9a. When a voltage is applied to dielectric gases (insulators), the electric field generated by the voltage pulls negative charges towards the anode and positive charges towards the cathode [147]. As the voltage increases, When gas experiences electrical breakdown and continues to form plasma, it allows current to flow through an insulating medium that would typically not conduct electricity (in this example, gas, but it could also be liquid), resulting in the formation of an electric arc [148, 149].

The specific breakdown voltage can be calculated using Paschen's Law, which specifically explains that the breakdown voltage for the arc formed between two electrodes is a function of the product of gas pressure and electrode distance, expressed as $V = apd/ln(pd)+b$. Here, 'a' and 'b' are constants associated with the gas composition [150]. At standard atmospheric pressure, a = 43.66 and b = 12.8 [151, 152]. Additionally, 'p' represents the gas pressure, and 'd' denotes the electrode distance. Subsequently, he investigated the breakdown voltage of different gases between parallel metal plates as the gas pressure and gap distance varied, and obtained Paschen curves as illustrated in Figure 2-8, indicating that, with a constant

gap length, the voltage required for arc formation across the gap decreases as the pressure decreases, then gradually increases, surpassing its original value [152].

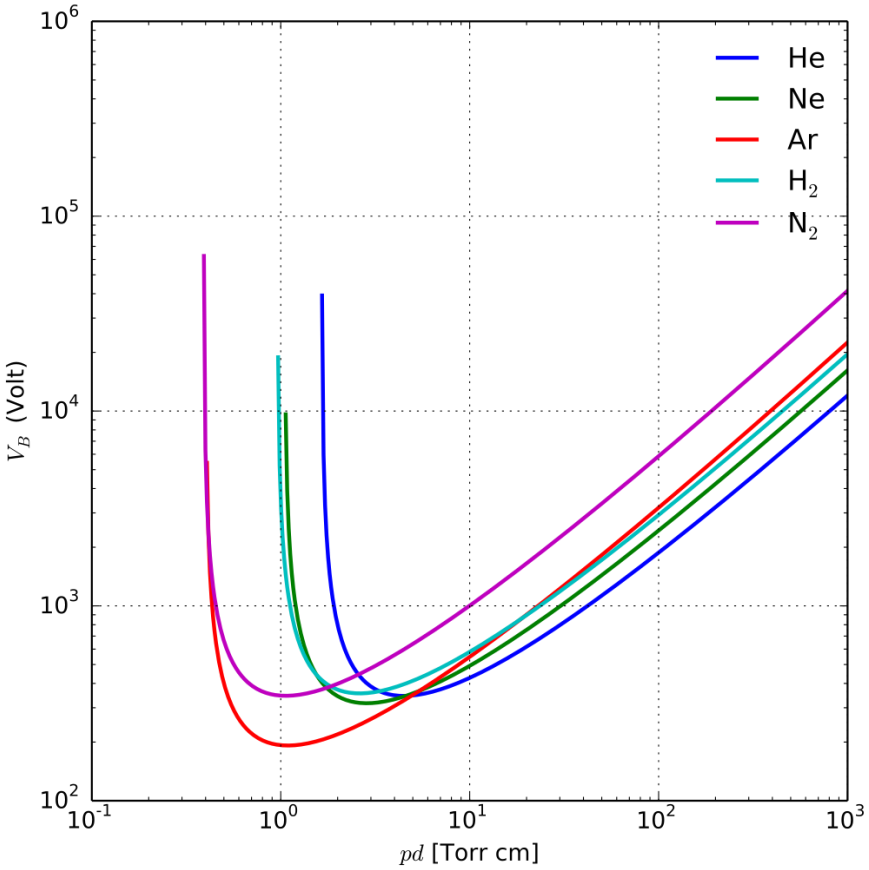

Figure 2-8 The Paschen curves for Helium, Neon, Argon, Hydrogen, and Nitrogen (adapted from [153]).

The average mean free path of molecules in a gas is the average distance between collisions with other molecules. At a given constant temperature, this is inversely proportional to the gas pressure. On the right side of the Paschen minimum point (high-pressure), there are more collisions in the electron path between the electrodes. These collisions reduce the energy of the electrons, making it more difficult for them to ionise molecules, thereby increasing the difficulty of initiating the avalanche effect [154]. Meanwhile, on the left side of the Paschen minimum point (lower pressure), the Pd product is small, allowing the electron mean free path to increase. In this scenario,

electrons may acquire a significant amount of energy, but the frequency of ionising collisions is lower [152]. Therefore, at low pressures conditions, triggering an avalanche by applying a higher voltage to ensure sufficient gas molecule ionisation can also successfully facilitate the emergence of plasma. A fluorescent lamp, illustrated in Figure 2-9b, is a prime example of a uniform direct current or alternating current being used between two metal plates, ionising inert gases such as argon or neon, producing light with various characteristic colours [155].

Due to plasmas' wide range of temperature and density, they find applications in various academic, technological, and industrial domains. Examples include extractive metallurgy, laser technology, mass spectrometry, space propulsion, plasma surface treatment methods, microelectronics etching, medical applications, and nuclear fusion research [142].

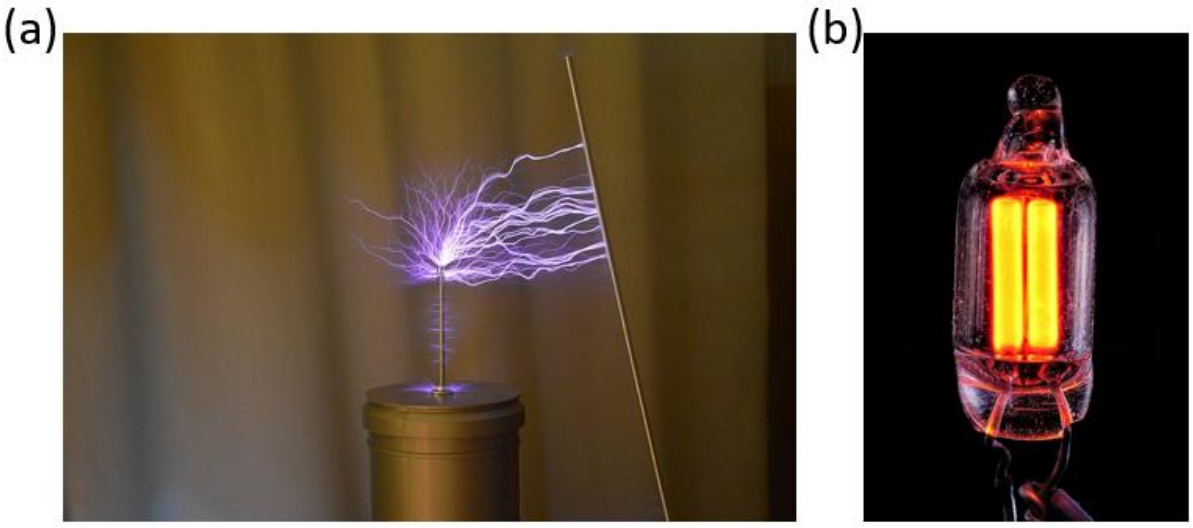

Figure 2-9 (a) a filamentary discharge pattern generated by a Tesla coil through plasma and (b) a neon gas fluorescent lamp, showcasing the phenomenon of ionisation and visible light emission in neon gas when electrified [155, 156].

2.4.2 Low-pressure plasma treatment

In low-pressure plasma processing, the formation and control of plasma occur at relatively low pressures, typically within the range of tens to hundreds of pascals. This processing technique finds extensive applications for surface modification of materials, thin-film deposition, surface cleaning, and material synthesis [142]. During the treatment, interactions between plasma and material surfaces commonly occur through excitation and ion bombardment, leading to changes in surface chemical and physical properties. Precise control over material can be achieved by adjusting plasma parameters and processing conditions, catering to diverse application requirements [157]. Consequently, plasma and low-pressure plasma processing play indispensable roles in modern technology, providing essential tools and methods for research and applications across various fields, including semiconductor manufacturing, thin-film technology, biomedical sciences, and energy-related domains [157].

As one of the significant applications of low-pressure plasma, plasma carburising and nitriding hold prominent positions in the field of surface engineering, providing more efficient and precise means to enhance the surface performance of metals [142]. Early methods for carburising and nitriding typically involved placing metal samples in a target atmosphere, using solid carbon sources or liquid suspension containing carbide salts for carburising, and ammonia or nitrogen gas atmosphere for nitriding.

Typically, to overcome the surface activation energy barrier, these processes normally require elevated temperatures, the carbon penetration efficiency also depends on it, which might cause high energy consumption [158]. The development of low-pressure plasma surface treatment technologies has made carburising and nitriding more convenient and efficient. In this approach, plasma treatment begins by ionising the

target gases into target ions and free electrons. Subsequently, the target ions are accelerated and implanted into the sample surface through an electric field, facilitating deeper penetration of nitriding; at the same time, ion bombardment during plasma treatment also leads to sputtering of surface material, reaction with the nitrogen-containing environment and formation, redeposition onto the surface and inward diffusion of M_xN_y compounds [159, 160].

Compared to traditional methods, low-pressure plasma treatment offers several advantages. It requires lower reaction temperatures, reduces energy consumption, activates the surface through plasma, facilitates self-cleaning in nitriding/carburising processes, and enables uniform and controlled surface modification [158]. This helps prevent excessive overheating and material deterioration, ensuring a uniform and controlled surface modification. Consequently, the development of low-pressure plasma surface treatment technologies leads to the formation of a more uniform and dense nitrided layer on metal surfaces, thereby significantly enhancing both nitriding and carburising processes.

It is worth mentioning that the evolution of low-pressure plasma treatment reactors has traversed a long period, dating back to the initial report on plasma processing by Wehnheldt in 1932 [161]. Through successive advancements in stability and plasma processing intensity, Bernard Berghaus and Wehnheldt collaborated in the joint development of Klöckner Ionon around 1970, serving as the primary equipment for ion nitriding since that time (equipment used within this study are from the same manufacturer used; as depicted in section 2.4.2.3). Although the focus of this study is the use of such plasma treatments for zirconia ceramics, these commercial plasma devices were originally developed for metal nitriding and carburising [161, 162].

2.4.2.1 Glow discharge and arcing

In the field of low-pressure plasma processing, phenomena such as glow-discharges, arcing, and hollow cathode formations are commonly found and can play important roles in the outcomes of plasma treatments of materials. Glow discharge is a phenomenon normally observed when generating plasma under low-pressure conditions; it typically manifests as a continuous glow emitted from the gas discharge region [163, 164]. The colour of the glow is characteristic of the composite of the gas undergoing excitation and ionisation, with diverse colours formed including blue (Xenon), purple (Argon), orange (Neon), purple (Nitrogen), yellow (Helium), and green (Krypton).

The simplest type of glow-discharge is DC glow-discharge; it has a fixed cathode and anode in the working tube or furnace, and a target gas such as neon or argon is normally present. A potential difference exists between the two electrodes, leading to the ionisation of a small fraction of the atoms in the target gas [165]. Simultaneously, electrons in the target gas are accelerated by the electric field between the cathode and the anode, gaining additional kinetic energy [139, 166]. As these electrons move towards the anode, they can collide with other ions or neutral particles in the way, and in doing so, they can transfer impart kinetic energy to the impacted particles. When the electric field strength reaches a certain level, the kinetic energy of these electrons surpasses a threshold, potentially enabling them to liberate additional electrons from the impacted particles. Then, these newly formed free electrons are, in turn, also accelerated and can contribute to the release of further electrons. This initiates a rapid avalanche-like process throughout the entire space (known as the Townsend avalanche, as shown in Figure 2-10), leading to a rapid increase in the electron and ion density throughout the processing space [166].

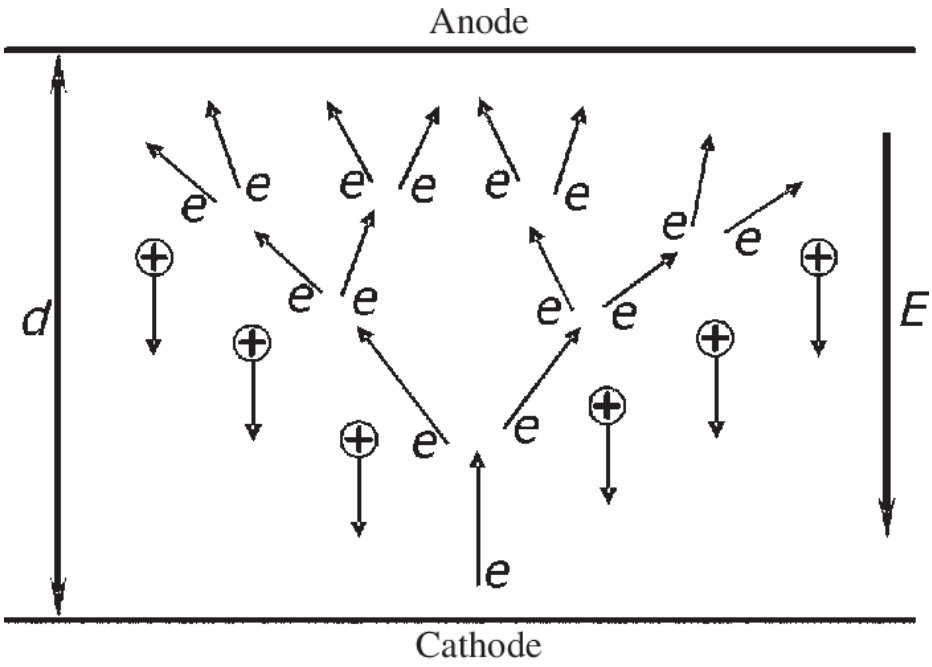

Figure 2-10 Townsend avalanche event with cascades of electron-induced ionisation events [139].

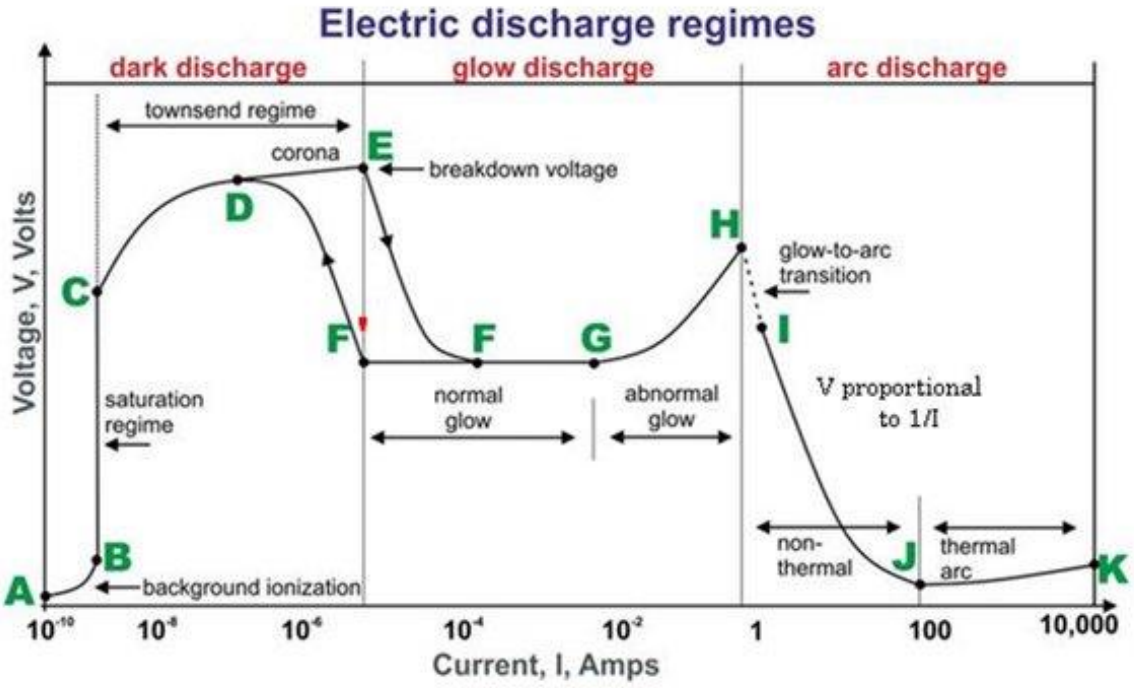

Figure 2-11 Typical current-voltage plot for different electric-discharge regimes [139].

This cascading process ultimately leads to the formation of a plasma. Before point E, it is known as the dark discharge, where the current is very low, and the discharge phenomena are not visible to the naked eye. Only a small amount of corona discharge and breakdown phenomena exist, with most charged particles accumulating near the cathode (positive ions) and the anode (free electrons) [139, 167].

After point E, the voltage has reached the breakdown voltage, and breakdown events at the electrodes dissipate the accumulated potential. Therefore, from E to F, a decrease in voltage and an increase in current intensity is observed. Notably, the low-current plasma only forms on a very limited portion of the cathode. As the current increases from F to G, the plasma begins to saturate the entire surface of the cathode (including recesses and edge regions), and at point G, a brighter and wider glow-discharge becomes visible to the naked eye. From point G to H, complete saturation of the cathode surface is already achieved, and the potential difference between the electrodes begins to increase. Consequently, increases in a current density lead to direct increases in the potential difference (referred to as abnormal glow discharge). Low-pressure plasma technologies such as plasma nitriding and carburising are typically employed within this region [167-169].

As the voltage continuously increases, the cathode is bombarded by the plasma, gradually raising the temperature. After point H, the electrode becomes hot enough to emit electrons thermally. With further increasing voltage, arc-discharges replace the glow-discharge. Since arc-discharges are more intense than glow-discharge and can generate many charges with each arc, resulting in a significant voltage drop and an increase in current (V proportional to 1/I) [168].

In the plasma treatment, arc-discharges can develop from the build-up of charge in a localised area (The presence of organic material (oil) due to poor cleaning or dust), leading to the electrical breakdown of the medium [170, 171]. This leads to electrical discharge from the charged region to the ground or anodic electrode. Long time arc discharge generates extremely high temperatures, causing the metal material in that area to melt or sputter, which may lead to the failure of the workpiece. While plasma treatment equipment typically comes equipped with rapid automatic arc detection devices, which commonly utilise current-limiting resistors combined with LC oscillation (a type of electrical oscillation occurring in a circuit containing an inductor (L) and a capacitor (C), it is still essential to enhance the pre-cleaning of the workpiece surface, including degreasing and dust removal, in order to minimize workpiece arcing during plasma treatment [172, 173].

2.4.2.2 Hollow Cathode Effect

The hollow cathode effect refers to the phenomenon that the cathode surface is not uniformly covered by a negative glow in a low-pressure plasma environment, especially refers to the formation of a higher-density plasma region near the cathode when a current passes through a cathode with a hollow or a hollow-like structure [174-176]. This high-density region is generally believed to accelerate the efficiency of plasma processing.

In the stage from point G to H (Figure 2-11), where the plasma has uniformly covered the entire cathode surface, the hollow cathode effect will persist between closely assembled components (components are put closer enough but larger than the location where the negative glow plasma forms) or on irregularly shaped workpieces (or sharp corners, such as those found at the edges of samples or in small holes).

Taking small holes as an example, the hollow cathode effect occurs because the negative glow regions around the hole walls overlap, leading to a rapid increase in the glow current density within the overlapping regions. This results in a significant temperature rise in the overlapping regions, and therefore, greater radiation of heat towards nearby surfaces. In the case of small holes, this leads to higher temperatures near the holes and lower temperatures away from the holes. The formation of hollow cathodes on samples can sometimes lead to deformation of samples, unwanted phase transformations and potentially melting of the material. Therefore, in the plasma processing of workpieces with complex geometries, measures are typically taken to pre-cover areas prone to the formation of hollow cathodes before plasma treatment. However, this practice can sometimes contribute to increased overall processing time, reduced yield of treated materials, and increased cost [172].

Despite their ambiguous name, the presence of hollow cathode phenomena can indeed be directly observed in plasma furnaces. Figure 2-12 illustrates the formation of hollow cathodes on an active screen lid used for active screen plasma nitriding. A metal-made active screen is positioned within the plasma furnace, enabling the observation of a stable glow discharge within the furnace. For each small hole on the active screen, as seen in the top-down view (bottom right corner in the figure), a small dense region is noticeable at the very centre, indicating the presence of the hollow cathode.

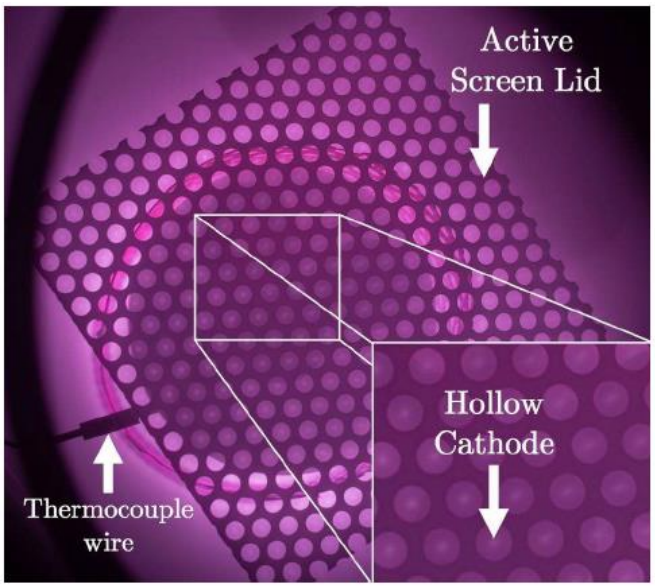

Figure 2-12 Hollow cathode formation on active screen [177].

However, with precise control, the hollow cathode effect can be also employed to expedite plasma processing. Many studies have devised highly efficient and simple solutions (similar to the plate as shown in Figure 2-13a) to boost processing efficiency in the DC plasma treatments [175, 178-180]. Concurrently, hollow cathode gas plasma sources with an inherent hollow cathode structure have been extensively developed as well, taking the FHC (fused hollow cathode) as an example (as depicted in Figure 2-13b), When there is gas and the lines/holes are given a cathodic potential, hollow cathodes form due to the interaction of the negative glow regions of adjacent plates/holes. These have emerged as alternatives to inductively coupled plasma (ICP) and microwave plasma (MP) sources, employed in plasma-enhanced atomic layer deposition (PE-ALD) and plasma-enhanced chemical vapour deposition (PE-CVD).

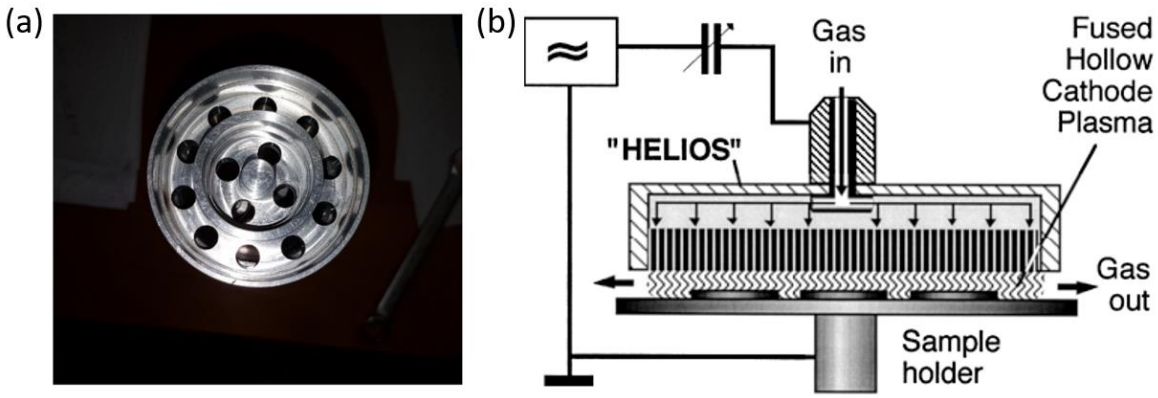

Figure 2-13 shows (a) An aluminium hollow cathode plate with 2.5 cm diameter of each hole; (b) Schematic diagram of the fused hollow cathode cold atmospheric plasma system with the rectangular electrode cartridge — HELIOS (hollow electrode linear integrated open structure) [178].

2.4.2.3 DC and AS Plasma

In this research, two types of low-pressure plasma treatments have been extensively explored, namely the DC (direct current) treatment and AS (active screen) plasma configurations (as illustrated in Figure 2-14). As both technologies are fundamental to this study, it is valuable to provide a background into the underlying principles and applications of the technologies.

Under DC plasma configurations, samples to be treated are directly in contact with the cathodic worktable of the furnace, and therefore (as illustrated in Figure 2-14a held at a cathodic potential (i.e., samples are extensions of the cathode). Alternatively, under AS plasma configurations, samples are electrically isolated from the worktable (i.e., held as a floating potential) while a conductive mesh cage and screen, connected to the cathodic worktable, surrounds the samples within the furnace (as illustrated in Figure 2-14b). Due to the traditional use of AS plasma treatments for nitriding or carburising of stainless steel materials, the mesh cage and screen (also commonly referred to as the active screen cage and lid) are composed of AISI 316 austenitic

stainless steel (although other materials can also be used such as Titanium) [181]. A distance of 20 mm was normally kept between the sample surface and the active screen lid. Under both DC and AS plasma configurations, the inner chamber walls of the furnace act as the anode electrode [18, 21, 181, 182].

As one of the traditional processes in plasma-assisted surface engineering, low-pressure DC plasma nitriding has been widely accepted within the industry for the nitriding of ferrous-based materials over the past four decades. It has found numerous advantages compared to alternative nitriding methods such as gas and salt bath nitriding, such as reducing energy consumption (as previously described in section 2.4.2) [183-185]. However, as samples to be treated are held at a cathodic potential during DC plasma treatment, plasma is generated and maintained near the surface of the samples. Although this direct contact with the plasma species enables in-situ cleaning of sample surfaces and brings the species necessary for the treatment of the surface (through ionic bombardment), it also creates some undesirable conditions. These disadvantages include potential damage to the sample due to the formation of arcs directly on the sample surface, inhomogeneous working temperature across the sample surface, electrically conductive sample surface requirement, and potential hollow cathode formations on samples (e.g., at sharp corners) (as mentioned in section 2.4.2.1 & 0). As an approach to overcome these barriers, AS plasma was developed in the 1990s to treat samples without the formation of the glow-discharge on the sample surface [18].

In AS plasma treatments, a mesh frame that connects to the cathode is used, while the sample is isolated using electrically insulating materials such as mica crystals or alumina (Al_2O_3) [18]. In this way, the sample can be maintained at a floating potential or lower bias voltage, thereby shielding it from direct ion bombardment. At the same

time, a high cathodic potential is generated on the metal screen, causing positively charged ionised particles in the furnace to bombard the mesh. Since this cage is a mesh, this leads to two crucial events: (1) the ions pass directly through the gaps in the mesh and are accelerated towards the sample surface, or (2) they impact the active screen and induce particles to sputter away and then fall (or travel through the gaps) and deposit onto the sample surface. In both cases, it results in the deposition of the materials, and for certain materials, can allow for the diffusion of light elements (e.g. nitrogen) into the material surface, thereby forming a modified surface layer [183, 184, 186].

However, the application of AS plasma treatment is encumbered by several limitations. Primarily, it operates under a line-of-sight principle, wherein predominantly the areas directly facing the AS lid receive treatment which means that the sample edges/surroundings will not equally be treated like DC [181, 184]. Meanwhile, the distance between the sample surface and the lid exerts a significant influence on the outcomes. The proximity of the sample to the lid may result in heightened ion penetration through the screen during plasma treatment, thereby inducing undesirable effects reminiscent of DC-related issues. Additionally, proximity to the screen may precipitate rapid heating of the sample, attributed to thermal radiation emanating from the screen. Conversely, distancing the sample too far from the lid is posited to impede the desired nitriding effect. Furthermore, during the carburising processing, it tends to engender a layer of soot on the surface, impeding deposition and diffusion [186, 187].

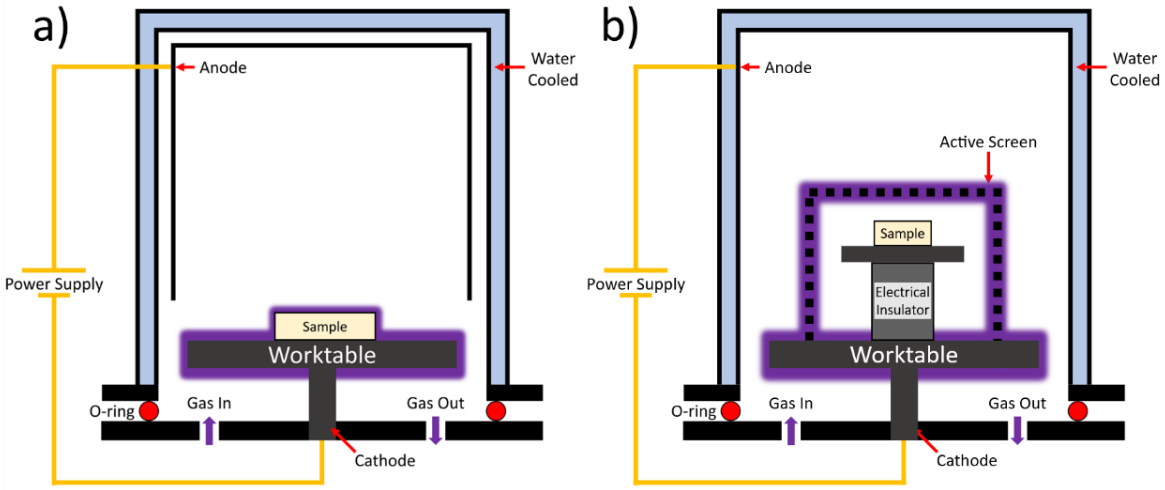

Figure 2-14. Schematic diagram of (a) DC and (b) AS plasma treatment setups [18].

Chapter 3 Experimental Work

This chapter is dedicated to the core experimental techniques that span across the three following research studies as reported in Chapter 4 to Chapter 6, and include sample preparation, plasma treatment, imaging, X-ray diffraction (XRD), and Raman spectroscopy. It is worth noting that more characterisation methods were used as described in the subsequent chapters; however, they only appear within their respective chapters, and detailed descriptions of them are provided within their respective chapters (Section 3.2 and 3.4 in this chapter were adapted from the work previously published in Journal of Materials Research and Technology (Vol 29, Pages 3759-3770) [18] and Acta Materialia (Vol 262, 119457) [12]).

3.1 Materials and sample preparation

The raw material utilised in this project is High purity 3 mol.% Yttria Partially Stabilised Zirconia (3YSZ), which was provided by Precision Ceramics (UK) through a high-temperature sintering process.

Table 3-1 The core data of the 3YSZ original specimens.

Properties	Values
Density [g/cm³]	6.05
Young's Modulus [GPa]	200
Hardness HV 0.5 [GPa]	13.5
Fracture toughness KIc [MPa/m²]	8
Thermal shock resistance [ΔT °C]	250
Thermal conductivity [W/mK]	2

Yttria-stabilised (3 mol%) zirconia (3YSZ) rods (10 mm diameter) were abrasion cut (Struers Accutom 50) using cubic boron a nitride cutting wheel to produce 3 mm thick cylindrical samples. Samples were subsequently flattened and ground (up to #4000 grit size) using SiC abrasive paper. Prior to plasma treatment, samples were polished using diamond suspensions (from 9 µm down to 1 µm). Ultrasonic cleaning using liquid detergent and acetone was carried out to remove contaminants between each stage.

Following plasma treatment, sample surfaces were polished using 1 µm diamond suspensions for approximately 10 seconds to remove the deposition layer formed during the plasma process and to return the surface to a smooth finish.

3.2 Plasma treatment

Plasma treatments were conducted using a Klöckner Ionon 40 kVA DC (direct current) plasma furnace at a treatment temperature RT-500 °C using the following parameters of voltage (< 600V), current (<5A), 100% H_2 or N_2 gas atmosphere, and working gas pressure of 3 mbar (300 Pa). Zirconia samples were positioned directly onto the stainless-steel worktable (cathode) and treated for 0.5-10 hours (Figure 3-1).

The anode of the power supply was connected to the interior furnace wall of the plasma chamber (as indicated by the yellow line in the diagram), the inner wall of the furnace can be considered as the anode. The cathode of the power supply was connected to the worktable where the samples were placed, so the worktable and the samples (when they become electrically conductive) can be directly considered as extensions of the cathode once the plasma is on. Due to the typically high-temperature environment inside the furnace during plasma treatment (in contrast to room temperature), circulating cooling water between the inner and outer walls of the

furnace to keep the walls cool and aids in cooling down once the treatment is completed.

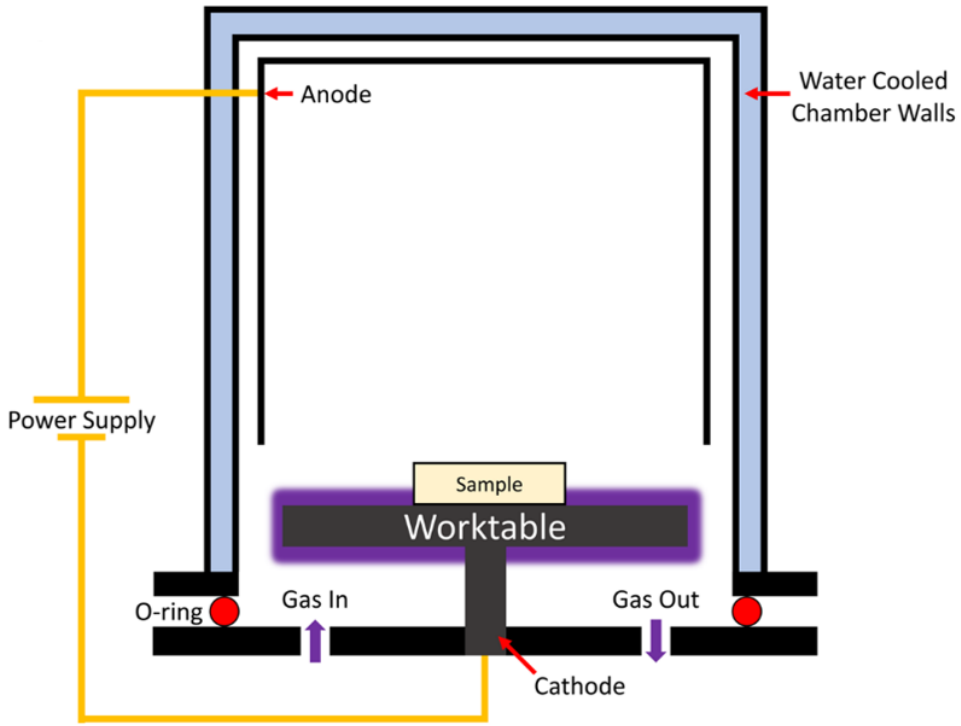

Figure 3-1 Schematic diagram of the DC plasma treatment configuration.

3.3 Imaging

In this project, the images provided can be categorised into two types. The first type comprises images displaying the appearance of samples at a large scale to demonstrate colour variations at the bottom, top, and cross-sections of the samples (primarily in chapters 4 and 5). The second type consists of magnified images showcasing the surface morphology/indentations of the samples (mainly in Chapter 6).

For the first type of image: polished samples were placed under good optical conditions (six 60 W daylight bulbs provided adequate illumination from different angles), and the background where the samples were placed provided a grid of

standard dimensions (10 mm x 10 mm) to allow the formation of a scale bar. The images of the samples were captured using a mobile phone camera.

For the second type of images: optical images near the indentation were obtained using a Axioskop 2 Zeiss optical microscope. The illumination setting was adjusted to 2, while the grating remained in its original mode. To capture comprehensive images accommodating various indentation sizes, 5x, 10x, and 20x objectives were utilised as needed.

It is worth noting that the acquisition of the surface morphology images of the samples exclusively employed optical instruments instead of SEM (scanning electron microscope). This is because zirconia itself is a non-conductor, and during the testing process, the accumulation of excess charge on the sample surface leads to poor imaging quality. Although the quality of SEM images can be partially improved by techniques such as gold coating (sputter coating process), using silver powder and silver paste, and employing conductive sample holders, discerning disparities between ZrO2 and ZrO_{2-x} remains elusive under SEM. Therefore, only surface topography information can be obtained - which is not information that is particularly valuable for this study.

3.4 XRD and Raman

Crystallographic phase analysis was performed using a Proto AXRD benchtop X-ray diffractometer fitted with a Cu radiation source (Kα = 0.15406 nm). Measurements were performed between the 2θ values of 20 ° and 80 ° using step increments of 0.01493 °. XRD spectra were analysed using the PANalytical Highscore Plus and Jade 6.5, followed by further optimisation and presentation using the OriginLab OriginPro software package.

Identification of the near-surface chemistry, phase structure (tetragonal to monoclinic transformation) and light absorption capabilities of the zirconia materials were performed using a Renishaw inVia Raman microscope fitted with a 532 nm excitation laser source and groove density of 1800 l/mm. Raman spectra were collected in the Raman shift range of 100–800 cm^{-1}. Decomposition of the Raman spectra was performed using the Renishaw WiRE software package to determine peak centre positions and FWHM (full width at half maximum) of each component before and after plasma treatment of the zirconia. Light absorption capability calculations were derived by comparing the area of each deconvoluted component of the spectra obtained from untreated and plasma-treated zirconia, utilising the CasaXPS software package. Subsequently, data were further optimised and presented using the OriginLab OriginPro software package.

Chapter 4 Plasma Defect-Engineering of Bulk Oxygen-Deficient Zirconia

Note: The work presented in this chapter has been published in the peer-reviewed journal **Acta Materialia** (Vol 262, 119457) [12].

Contribution: (Conceptualization: Supporting; Data curation: Lead; Formal analysis: Equal; Investigation: Lead; Methodology: Supporting; Validation: Equal; Writing – original draft: Lead; Writing – review & editing: Equal).

Abstract

Oxygen-deficient zirconia (ZrO_{2-a}) has recently emerged as a promising material for light absorption and photocatalytic applications. However, the economic and environmentally friendly manufacture of bulk ZrO_{2-a} remains challenging and has limited widespread adoption. In this study, we present a novel low-pressure (300 Pa) plasma treatment (H_2 gas at 500 °C for 5 hours) capable of producing fully-dense bulk ZrO_{2-a} without significant structural modifications. EPR (electron paramagnetic resonance) and XPS (X-ray photoelectron spectroscopy) characterisation of the plasma treated zirconia indicate the formation of Zr^{3+} ions $^{+}$ ($V_O^{\cdot\cdot}$) centres. The increase of oxygen vacancies is also supported by the greater exothermic heat flow and relative mass gain observed through TGA (thermogravimetric analysis) and DSC (differential scanning calorimetry) analyses. Diffuse reflectance spectroscopy (DRS) reveals a substantial enhancement in light absorption, with an average increase of 66.2% and >65% absolute absorption across the entire spectrum (200-3000 nm). XPS and DRS measurements suggest a significant reduction in both direct (from 4.84 to 2.61 eV) and indirect (from 3.19 to 1.45 eV) bandgap transition. By effectively enhancing the light absorption capability, reducing bandgap transitions, and maintaining the structural integrity of zirconia, low-pressure plasma treatments offer a promising and scalable approach for the environmentally friendly production of next-generation ZrO_{2-a} materials.

4.1 Introduction

Semiconductor-based technologies hold great promise for meeting the increasing demands for renewable and green energy. Significant research efforts have been directed towards developing future solutions, at both material and device levels, capable of harvesting or producing energy from sustainable sources [188-190]. Numerous studies have already demonstrated the potential for semiconducting materials to act as solar energy harvesters or photocatalytic materials, for instance for the efficient generation of hydrogen from water [191, 192]. However, when compared to commonly studied materials such as silicon and titanium dioxide, pristine zirconia is not typically considered an attractive solution for energy applications. The relatively wide bandgap of zirconia (approximately 5-6 eV) does not readily facilitate the initiation or catalysis of typical reactions involved in these applications [193-198]. Fortunately, recent breakthroughs using defect-engineering techniques have demonstrated the possibility to reduce the bandgap of zirconia by introducing large densities of oxygen vacancies (e.g., down to 2.52 eV in a study by Sinhamahapatra *et al.* [199]). Such modifications can create new donor energy levels between the valence and conduction bands (known as mid-gap states), and consequently, transforms the electrically insulating zirconia into an n-type semiconducting material [200]. The narrow bandgap of oxygen-deficient zirconia (ZrO_{2-a}) enables the absorption of photons with longer wavelengths, which also increases the photocatalysis range of the material. This has generated substantial interest for the use of ZrO_{2-a} as a future photocatalytic material for the splitting of water to generate clean hydrogen, for the decomposition of CO_2 to reduce greenhouse gases, and for the formation of reactive oxygen species (e.g., superoxide ions, hydroxyl radicals and peroxides) [201-205].

Although oxygen-deficient zirconia has many encouraging properties, the challenges to efficiently produce oxygen vacancies in zirconia have limited its widespread adoption. This barrier corresponds to the high energy requirements, of the order of 7.8-9.1 eV (753–880 $kJmol^{-1}$), to dissociate Zr-O bonds [199, 206-210]. Consequently, oxygen deficient zirconia has largely been confined to research environments, where significant efforts have been dedicated to developing new highly efficient and cost-effective manufacturing routes. Two promising approaches are the Zu *et al.* [200] and Wang *et al.* [211] methods, both of which make use of zirconia particle/powder precursors. In the Zu *et al.* [200] method, oxygen-deficient zirconia nanoparticles are produced through molten lithium reduction of pure zirconia disks at 400 °C under high-purity argon gas. Once the zirconia turns black, impurities are removed by repeated washing with HCl, ethanol, and deionised water, followed by ultrasonication to return them to nanoparticles. The Wang *et al.* [211] approach produces black oxygen-deficient zirconia through high-pressure torsion straining (6 GPa for 2 turns at 400 °C) of yttria-stabilised zirconia powders, which forms a thin, dense, and highly distorted layer of material (due to plastic deformation, lattice defects and phase transformation events).

In addition to the above mentioned approaches, various other techniques have also been explored for introducing oxygen vacancies into zirconia, including electric (or flash) sintering,[196, 212, 213] high-temperature carbon reduction,[214] cationic doping,[215-217] Ar^+ bombardment,[218] magnesiothermic reduction,[199, 202] and electrochemical reduction [219-225]. Each of these methods offer alternative pathways to reduce the bandgap of zirconia and improve its photocatalysis property. It is important to note that, other than the electrochemical reduction methods, the other listed approaches have only been demonstrated to work with zirconia in the form of

powders, nanotubes, or disks. This can create significant barriers for use of dense oxygen-deficient zirconia in future industrial applications. Moreover, many of the listed approaches involve demanding processing conditions such as high pressures and temperatures or the use of strong reducing agents (e.g., acids), thereby creating environmental concerns about their safe usage and proper disposal if such methods were to be upscaled [199, 226].

Electrochemical reduction techniques, which can form oxygen vacancies in solid zirconia, have shown promising results for rapidly forming dense sheets of oxygen-deficient zirconia. By applying a voltage difference at two ends of the material, it is possible to generate oxygen vacancies at the anode-facing end and propagate them towards the cathode-facing end [23, 196, 213, 219, 222]. As the electrodes must be in direct contact with the ends of the material, this can generate a tri-layer junction across the specimen when applying large potential differences, leading to the potential development of n-type conductivity at the cathode-end, p-type conductivity at the anode-end, and a largely unchanged bulk [227, 228]. High-temperature electrochemical reduction methods utilising voltage biases and manipulating boundary conditions have been shown to be able to effectively bypass this tri-layer configuration [229]. The major advantage of the electrochemical reduction approach is the ability to utilise commercially available solid zirconia sheets for the transformation into identically shaped and sized oxygen-deficient zirconia sheets. In this way, it is more convenient and cost-effective to showcase the potential of oxygen-deficient zirconia, as well as to significantly reduce the barriers to future upscaling and industrial adoption. In addition, the direct production of solid products bypasses the challenges related to the efficient sintering of oxygen-deficient zirconia powders without re-oxidation. However, existing electrochemical reduction routes pose challenges for the

homogeneous treatment of components with complex geometries (non-uniform potential difference) or the low-temperature formation of fully n-type or p-type semiconducting oxygen-deficient zirconia (due to the directional growth and the potential tri-layer structure).

Low-pressure direct current (DC) plasma treatments, which are traditionally used to modify the surfaces of metallic materials,[19-21] also involve the use of a potential difference across an anode and a cathode. In the case of low-pressure DC plasma treatments, this potential difference leads to the formation of a conductive gas medium (plasma), which completes the circuit, and enables the acceleration of positive ions (towards the cathode) and electrons (towards the anode). As the gas medium can carry the charge across the cathode and anode, there are no requirements for the physical connection of the electrodes [22]. Therefore, low-pressure DC plasma treatments can be considered a unique form of electrochemical treatment that has the potential to bulk-reduce zirconia materials under certain conditions (such as pressure, gas mixture, and power) [23, 24]. However, as electrically conductive materials are traditionally required for DC plasma treatments, no studies have explored the feasibility of DC plasma treatments to transform pristine zirconia into oxygen-deficient zirconia [22].

Thus, the aim of this study is to investigate the potential of low-pressure DC plasma treatments to reduce solid polycrystalline zirconia into oxygen-deficient zirconia. As the feasibility of the plasma treatment and the comprehensive characterisation of the treated material is the focus of this study, a simple plasma treatment protocol has been chosen (100% hydrogen plasma treatment under a fixed temperature of 500 °C and gas pressure of 300 Pa).

4.2 Methods

4.2.1 Sample Preparation

Yttria-stabilised (3 mol%) zirconia rods (10 mm diameter; Precision Ceramics UK) were abrasion cut (Struers Accutom 50) using cubic boron nitride cutting wheels to produce 3 mm thick cylindrical samples. Samples were subsequently flattened and ground (up to #4000 grit size) using SiC abrasive paper. Prior to plasma treatment, samples were polished using diamond suspensions (down to 1 μm). Ultrasonic cleaning using liquid detergent and acetone was carried out to remove contaminants between each stage.

4.2.2 Low-pressure DC Plasma treatment

Plasma treatments were conducted using a Klöckner Ionon 20 kVA DC plasma furnace at a treatment temperature of 500 °C using the following parameters of 550 V, ≈1 A, 100% H_2 gas atmosphere, and working gas pressure of 3 mbar (300 Pa). Zirconia samples were positioned directly onto the stainless-steel worktable (cathode) and treated for 5 hours (Figure 4-1). After the plasma treatment, samples were gently polished using 1 μm diamond suspensions to remove loose deposited material (due to sputtering from the worktable).

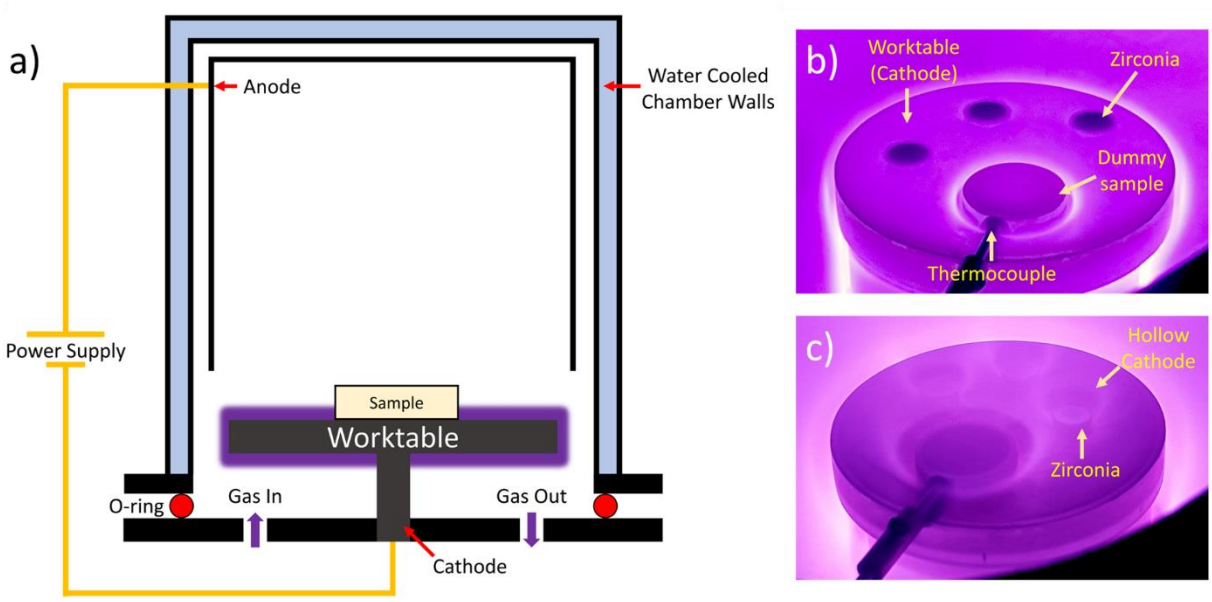

Figure 4-1 Schematic diagram of the DC plasma treatment configuration (a). Initially, the glow-discharge plasma only forms on the cathodic worktable (b). However, as the treatment progresses, (c) the glow-discharge also begins to form on the zirconia specimen (as indicated by the hollow cathode formation).

4.2.3 X-ray diffraction (XRD)

Crystallographic phase analysis was performed using a Proto AXRD benchtop X-ray diffractometer fitted with a Cu radiation source (Kα = 0.15406 nm). Measurements were performed between the 2θ values of 20 ° and 80 ° using step increments of 0.01493 °. XRD data was analysed using the PANalytical Highscore Plus software (with the ICDD PDF-2 database).

4.2.4 Raman spectroscopy

Identification of the near surface chemistry, phase structure (tetragonal to monoclinic transformation) and light absorption capabilities of the zirconia materials was performed using a Renishaw inVia Raman microscope fitted with a 532 nm excitation laser source and groove density of 1800 l/mm. Raman spectra were collected in the Raman shift range of 100–800 cm^{-1}. Decomposition of the Raman spectra was

performed using the Renishaw WiRE software package to determine peak centre positions and FWHM (full width at half maximum) of each component before and after plasma treatment of the zirconia. Light absorption capability calculations were obtained by comparing the area of each deconvoluted component of the spectra obtained from untreated and plasma treated zirconia (using the CasaXPS software package). The relative change in area under the curve for each fitted component following plasma treatment was compared with untreated zirconia to calculate the average percentage change in total emitted light.

4.2.5 Electron paramagnetic resonance (EPR) spectroscopy

Paramagnetic centres in the zirconia were investigated using EPR spectroscopy (ELEXSYS-II EPR spectrometer) at room temperature using an N_2 atmosphere at an X-band frequency of 9.84 GHz, modulation amplitude of 1 G (0.1 mT) and microwave power of 3.99 mW. Patterns were generated around a 3500 G central magnetic field, with a sweep width of 150 G and sweep time of 30 s.

4.2.6 X-ray photoelectron spectroscopy (XPS)

Changes in the bonding environment of Zr and O atoms within the zirconia samples following plasma treatment were investigated using XPS spectroscopy (Thermo Scientific Nexsa XPS) fitted with a monochromatic Al X-ray Kα (1486.6 eV) X-ray source. Valence band (VB) energy levels of the zirconia samples were revealed by low energy XPS spectroscopy (up to 10 eV with an energy step size of 0.1 eV). High resolution scans (energy step size of 0.05 eV) were used to characterise the bonding environment of Zr 3d (178-188 eV) and O 1s (526-538 eV) electrons. C1s (284.6 eV) scan correction was performed for all spectra to account for the charging of the samples. Deconvolution and analysis of XPS spectra were performed using the

CasaXPS software package. Monte Carlo error analysis was used to test the validity of the modelled components and to calculate the standard deviation of the area compositions. Further information regarding the fitting parameters and error analysis can be found in section 4.5 of the supplementary information.

4.2.7 Thermal analysis

Simultaneous thermal analysis (STA) measurements were carried out to determine the mass and heat flow changes of the samples upon heating. Both thermogravimetric analysis (TGA) and differential scanning calorimetry (DSC) data were measured on untreated and plasma treated zirconia (recorded simultaneously) using a Netzsch STA 449F3. STA measurements were performed in air using plate samples of dimensions of 2 mm in length, 2 mm in width and 0.5 mm in thickness (placed in a platinum crucible). Samples were heated to 500 °C at a heating rate of 10 °C/min, and then held at 500 °C for 10 hours, before passively cooling down to room temperature. An empty run was performed to account for the background noise contributions of the measurements (e.g., due to weight and heat flow errors within the system). To reduce the initial influence of contaminants (e.g., adsorbed moisture) during the heating up process, relative mass change was normalised to the measured mass at 100 °C for the heating up stage and to the measured mass at the beginning of the holding stage (at 500 °C).

4.2.8 Optical absorption measurement

The photon absorption behaviour of untreated and plasma treated zirconia were measured by diffuse reflectance spectroscopy (DRS) across the UV-Vis-NIR-SWIR (ultraviolet – visible – near-infrared – shortwave infrared) range with a Shimadzu SolidSpec-3700 spectrophotometer fitted with an integrating sphere. DRS was utilised

to bypass the opaque nature of the material, with spectra being obtained between wavelengths of 200-3000 nm, using a step size of 1 nm and medium scan speed. As suggested by several recent studies,[230-232] a combination of the Tauc method and Kubelka-Munk function were used to determine the allowed direct and indirect transitions (further information regarding the method and justifications are provided in section 4.5.3 of the supplementary information).

4.3 Results and Discussion

Dense sintered oxygen-deficient zirconia with a small bandgap has tremendous potential to create new opportunities for the development and expansion of zirconia as an energy harvesting and oxygen sensing (particularly at lower temperatures) material of industrial interest. To explore the potential for low-pressure DC plasma treatments to bulk reduce dense 3 mol% yttria-stabilised zirconia, the findings of this study structured to discuss (1) the visual, crystallographic, and structural characteristics of the plasma treated zirconia, (2) to confirm the formation of oxygen vacancies and the reduction of the zirconium ions, and (3) to characterise the electronic band structure and light absorption capability of the plasma treated zirconia.

4.3.1 Visual, crystallographic, and structural changes

The complete colour transformation of the zirconia, going from a pure white to a metallic black, is the most striking visual modification following plasma treatment (Figure 4-2). The through-depth nature of the blackening process (i.e., entire transformation of the sample) was revealed by cross-sectional observations (Figure 4-2b2). The gradient of blackening, with darker colours near the bottom surface (cathode-facing), suggests a similar directional growth route as other electrochemical reduction approaches (growth from the cathode towards the anode) [219]. The colour variations between the centres and edges of the sample also suggest a preferential transformation mechanism during the treatment, potentially arising due to electrical potential variations across the cathode-facing surface. Although the distinct colour transformation of zirconia implies that oxygen-deficient zirconia has formed, more direct confirmation of the transformation was revealed via EPR, XPS and DSC/TGA analysis can be found in section 4.5 [233].

Despite the remarkable morphological change in colour, no formation of new phases could be identified under XRD analysis (Figure 4-3a). The varying densities of oxygen vacancies across the untreated and plasma treated zirconia samples gave rise to different localised stoichiometries (i.e., ZrO_{2-a}, where x varies but remains <2), which could not be wholly indexed by any single XRD reference pattern. However, no unidentifiable (or satellite) peaks belonging to structures other than tetragonal phase zirconia or yttria-stabilised zirconia were found. Moreover, no significant large shift in d-spacing or broadening of peaks were observed, with no change or only minor change of the long range order developed following the plasma treatment of zirconia [200, 211, 234].

The Raman spectra of the untreated and plasma treated zirconia (Figure 4-3b) indicated no detectable change in the chemical structure, formation of new peaks, or significant displacement of existing peak centres. Both untreated and plasma treated zirconia only exhibited characteristic peaks assigned to the different vibrational modes of 3 mol% yttria-stabilised zirconia (Figure 4-3b), including three E_g modes (260.2, 464.8, 642.7 cm^{-1}), two B_{1g} modes (147.0, 323.0 cm^{-1}) and one A_{1g} mode (609.2 cm^{-1}), which all belong to the $P4_2/nmc$ space group [217, 235]. Deconvolution and fitting of the spectra suggests no consistent or obvious displacement or broadening of the peaks (outlined in section 4.5 of the supporting information) and suggests that there is no significant long-range distortion of the lattice, which aligns with the XRD measurements [236]. The most noticeable difference between the two zirconia samples is the significant reduction in reflected light intensity observed in the plasma treated sample, which will be discussed in 4.5.

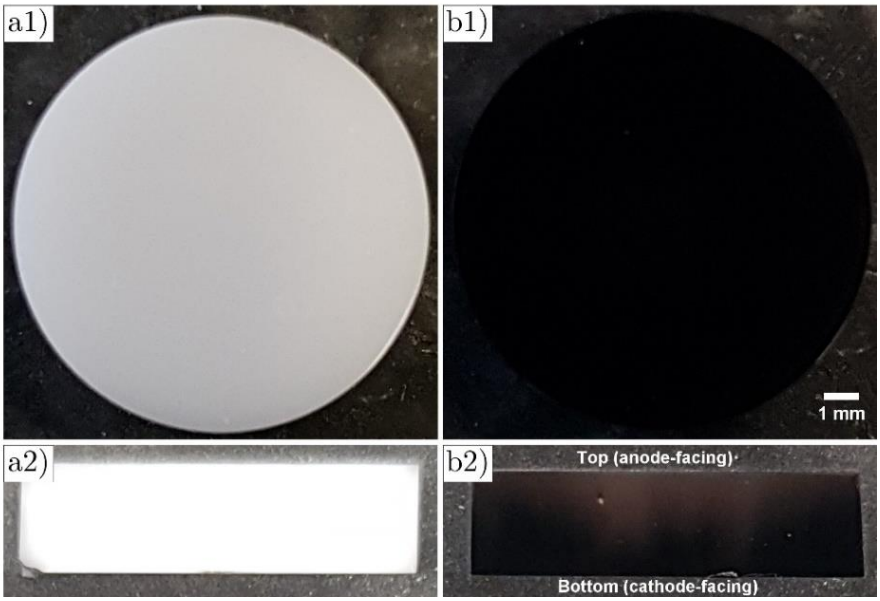

Figure 4-2 Camera images of (a) untreated and (b) plasma treated zirconia from the bottom surface (labelled 1) and cross-sectional (labelled 2) views are shown. The bottom surface images (a1 and b1) clearly illustrate the complete transformation of zirconia from white to black after plasma treatment. The cross-sectional views reveal an internal colour gradient, with the bottom surface facing the cathode appearing darker and the top surface facing the anode appearing lighter.

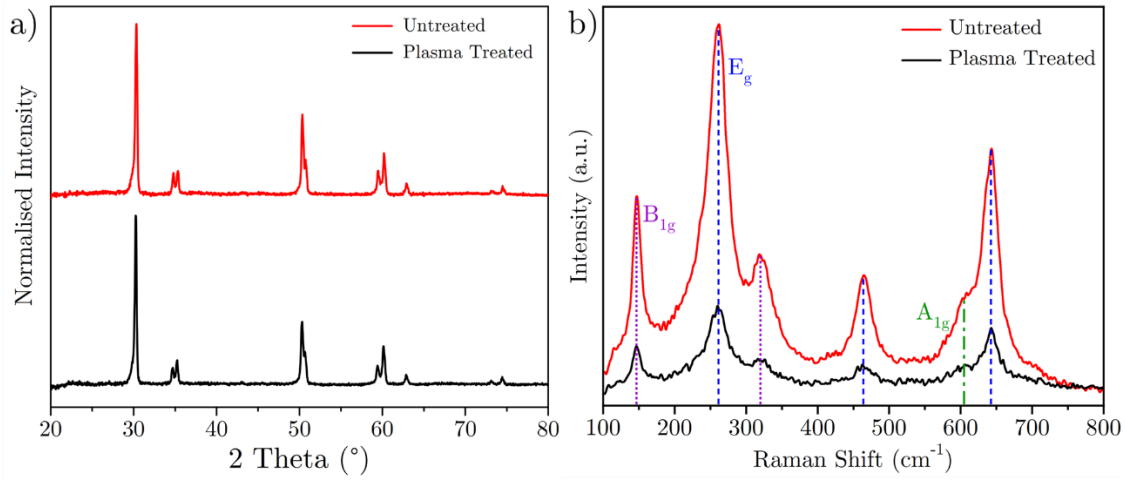

Figure 4-3 The (a) XRD and (b) Raman spectra of untreated and plasma treated zirconia are shown. The typical locations of the B_{1g} (dotted), E_g (dashed), and A_{1g} (dotted and dashed) vibrational modes of zirconia are indicated within the Raman spectra. No change in structure

or peak shift can be observed under either XRD or Raman spectroscopy. However, the measured light intensity under Raman spectroscopy is significantly reduced following plasma treatment, resulting in a poor signal-to-noise ratio under the same settings.

4.3.2 Confirming the oxygen-deficiency of plasma treated zirconia

4.3.2.1 EPR detection of F centres & reduced zirconium

Oxygen vacancies are common phenomena in many oxides, with their formation giving rise to properties such as increased ionic conductivity and light absorption capability. Despite their classification as a crystallographic point defect of the material, the controlled existence of vacancies can give rise to beneficial physical and mechanical properties, zirconia doped with yttria (Y_2O_3) being an excellent example [208]. The difference in oxidation states of zirconium (Zr^{4+}) and the yttrium (Y^{3+}) ions means that, for every two yttrium ions that displace zirconium ions ($2Y'_{Zr}$), an oxygen vacancy ($V_O^{\cdot\cdot}$) must be formed in the lattice to preserve charge neutrality (Equation 4-1) [237]. The combination of the larger ionic radii of yttrium and the reduction of interlaminar stresses (due to the vacant oxygen sites) gives rise to the "pinning" of the tetragonal or cubic phase at room temperature [238]. The stability (or metastability) of these high temperature phases give rise to many of the advantageous properties (e.g., high fracture toughness) that differentiate zirconia to other ceramics.

$$Y_2O_3 \xrightarrow{ZrO_2} 2Y'_{Zr} + V_O^{\cdot\cdot} + 3O_O^X \quad \text{(Equation 4-1)}$$

Due to the profound influence that these oxygen vacancies have on the overall colour of the material, such defects are typically called F centres or colour centres [225]. F centres are primarily identified according to their relative charge (as compared with the occupation of the site with an O^{2-} ion), and therefore three main configurations

exist: the F^{2+} ($V_O^{\cdot\cdot}$; 0 trapped electrons), F^{+} ($V_O^{\cdot}$; 1 trapped electrons), and F centres (V_O^X; 2 trapped electrons) [224]. Further subcategorisation of the F centres can also be performed depending on the location (e.g., surface or bulk), vicinity to other vacant sites (e.g., neighbouring oxygen vacancies), and the displacement of neighbouring cationic sites [239].

Electron paramagnetic resonance (EPR) spectroscopy presents as the most commonly used method to identify F centres; however, as EPR signals depend on the presence of unpaired electrons, only paramagnetic F^{+} centres with single trapped electrons can be measured, while F and F^{2+} centres remain invisible to EPR [198, 223, 240, 241].

Depending on the oxidation state of neighbouring cations, EPR spectra can also help to detect the presence of cations with unpaired electrons. In the case of zirconia, this can allow the presence of Zr^{3+} ions to be detected. Although there are many more pathways for forming Zr^{3+} ions (dehydration of OH^- groups), we showcase 2 possible routes for their formation in the presence of F^{+} (equation 4-2) and F^{2+} (equation 4-3) centres [196, 214, 233].

$$ZrO_2 \rightarrow Zr^{3+} + O_O^X + V_O^{\cdot} + \frac{1}{2}O_2 \quad \text{(equation 4-2)}$$

$$2ZrO_2 \rightarrow 2Zr^{3+} + 3O_O^X + V_O^{\cdot\cdot} + \frac{1}{2}O_2 \text{ (equation 4-3)}$$

Figure 4-4 displays the EPR spectra, and reveals significant formation of new paramagnetic centres after plasma treatment of the zirconia. The decomposition of the spectra indicates the presence of two underlying signals at g-tensor values of $g_\perp$= 1.9785 (signal 2) and $g_\parallel$ = 1.9763 (signal 3). These values closely align with previous reports of Zr^{3+} ions (d^1 ion) within bulk tetragonal phase zirconia [198, 211, 223, 234,

242-246]. Moreover, both untreated and plasma treated zirconia exhibit an isotropic peak (signal 1) at g-tensor values of 2.0040 (g_1(U)) and 2.0039 (g_1(PT)), respectively. EPR studies on zirconia in powder form typically associate signals close to this g-factor with surface adsorbed superoxide ions (O_2^-), which can result from the oxidation of Zr^{3+} back to Zr^{4+} (equation 4-4). If this signal corresponded to superoxides, an increase of the signal would be expected following the reduction of the zirconium ions after plasma treatment. Therefore, as this trend is not observed, this suggests that the signal does not correspond to the adsorption of superoxides. Furthermore, superoxides usually exhibit a set of three peaks at g-factors approximately equal to 2.0336 (g_{zz}), 2.0096 (g_{yy}), and 2.0034 (g_{zz}), which are also not found in the zirconia samples of this study [198, 244].

$$Zr^{3+}{}_{(surf)} + O_{2}{}_{(gas)} \rightarrow Zr^{4+}{}_{(surf)} + O_2^-{}_{(ads)} \qquad \text{(equation 4-4)}$$

F^+ centres have also been suggested to exhibit peaks between g-tensor values of 2.002 and 2.004 and can be expected to form following the plasma treatment of zirconia (equation equation 4-2) [216, 244, 247, 248]. The lack of an increase in signal 1 can be explained by the preferential formation of diamagnetic F^{2+} centres under plasma treatment (equation equation 4-3) [249]. These F^{2+} centres would give rise to EPR-elusive vacancies that would not contribute to the intensity of the measured spectra. However, given the significant increase in Zr^{3+}, this suggests that F^{2+} centres must form in the bulk of plasma treated zirconia, while F^+ centres are confined to defect sites on the surface or in the bulk (e.g., grain boundaries) of the material [247].

As signal 1 is present (and at a similar intensity) in untreated zirconia, the conversion of any pre-existing F^+ centres to F^{2+} centres would be expected to result in a reduction of signal 1. However, no noticeable change in signal 1 is observed following plasma

treatment of the zirconia. This suggests that either the site of the paramagnetic centres corresponding to signal 1 are not affected by the plasma treatment or they are re-established when the samples are exposed to atmospheric conditions [250]. This supports the idea that these paramagnetic centres correspond to surface defects (especially as both tested sample types have similar surface areas). However, a more in-depth evaluation of these paramagnetic sites is necessary to identify the origin of these signals (e.g., by way of scanning tunnelling microscopy or environmentally controlled EPR measurements).

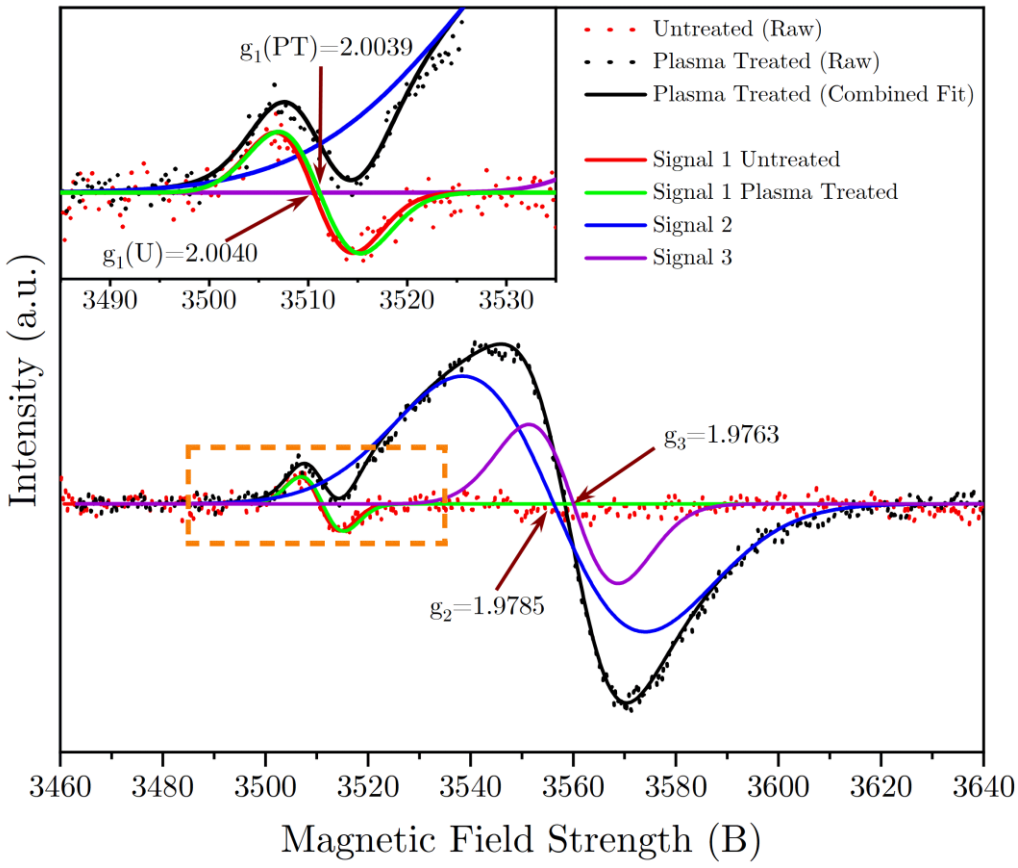

Figure 4-4 EPR spectra of untreated and plasma treated zirconia are displayed, showing the raw data as dots and the fitted data as lines. In both untreated and plasma treated zirconia, a peak (signal 1) is observed near the g-tensor of a free electron (g_e) with fitted g-factors of 2.0040 (g_1(U)) and 2.0039 (g_2(PT)), respectively. The inset in the top left provides a magnified view of the dashed region corresponding to this signal. Following plasma

treatment, new paramagnetic centres (signals 2 and 3) associated with the formation of Zr^{3+} are detected at g-tensors of 1.9785 (g_2) and 1.9763 (g_3). The similar intensity of signal 1 for both untreated and plasma treated zirconia suggests that the reduction process preferentially leads to the formation of diamagnetic F^{2+} centres, as indicated by equation equation 4-3.

4.3.2.2 XPS evaluation of oxygen and zirconium bonding environment

In agreement with the EPR analysis, the XPS (X-ray photoelectron spectroscopy) measurements also suggest the reduction of zirconium ions ($Zr^{4+} \rightarrow Zr^{3+}$) and the increased formation of oxygen vacancies.

Deconvolution of the O 1s spectra in Figure 4-5 reveals the presence of three distinct peaks, labelled as O1, O2, and O3, for both untreated and plasma treated zirconia [200]. Consistent with the literature, which is reviewed in section 4.5 of the supporting information, these peaks have been assigned to specific components. Specifically, O1 corresponds to lattice oxygen in zirconia, O2 corresponds to surface adsorbed hydroxyl groups, and O3 corresponds to surface adsorbed molecular water.

Non-dissociative adsorption of water occurs through hydrogen bonding with occupied zirconia lattice sites and is not typically associated with the reduction (or oxidation) of the adsorption site. On the other hand, in the presence of oxygen vacancies, molecular water can undergo dissociation, resulting in the formation of a hydroxyl group that occupies the vacant site and a hydrogen atom that bonds with a nearby lattice oxygen, thereby forming another hydroxyl group. This dissociative adsorption of water onto zirconia surfaces containing oxygen vacancies ($V_{\dot{O}}$ and V_O^X) can lead to the reduction of zirconium ions, as shown in equations 4-5 and 4-6, respectively [250].

Under ambient conditions, dissociative adsorption of water is energetically more favourable than non-dissociative adsorption. Therefore, surfaces with higher densities of oxygen vacancies are expected to exhibit lower amounts of adsorbed molecular water (O3) but higher concentrations of surface adsorbed hydroxyl groups (O2) and Zr^{3+}. Therefore, when analysing oxygen vacancies using XPS, it is important to consider changes in both the oxygen and zirconium bonding environments [251].

$$Zr_{Zr}^{X} + V_{O}^{\cdot} + O_{O}^{X} + H_2O \rightarrow 2(OH)_{O}^{\cdot} + Zr_{Zr}^{\prime} \qquad (4\text{-}5)$$

$$2Zr_{Zr}^{X} + V_{O}^{X} + O_{O}^{X} + H_2O \rightarrow 2(OH)_{O}^{\cdot} + 2Zr_{Zr}^{\prime} \qquad (4\text{-}6)$$

The analysis of the fitted components of the O 1s spectra for both untreated and plasma treated zirconia samples shows no significant positional shift, with binding energy displacements of 0.1 eV for O1, 0.1 eV for O2, and 0.2 eV for O3. This observation is consistent with other published findings on modified zirconia [252, 253]. Additionally, the error analysis of the fitted components also indicates the good validity of the models, with a maximum area composition standard deviation of 0.26%.

Figure 4-5 and Table 4-1 illustrate the most significant difference between the O 1s spectra of untreated and plasma treated zirconia, which lies in the concentrations of the different components (O1, O2, and O3). While the O1 component remains relatively unchanged, with a slight increase from 18.7 ± 0.3% to 19.5 ± 0.2% following plasma treatment, notable modifications arise in the O2 and O3 components. The O2 component shows a significant increase from 25.5 ± 0.2% to 37.8 ± 0.2%, which represents a 12.3% increase, whereas the O3 component decreases from 55.8 ± 0.3% to 42.7 ± 0.3%, indicating a 13.1% decrease. Therefore, this combined change in composition, along with the corresponding changes observed in the Zr 3d spectra (discussed in the following paragraphs), demonstrates an overall increase in surface

hydroxyl groups (O2) and a decrease in surface adsorbed water (O3) following plasma treatment.

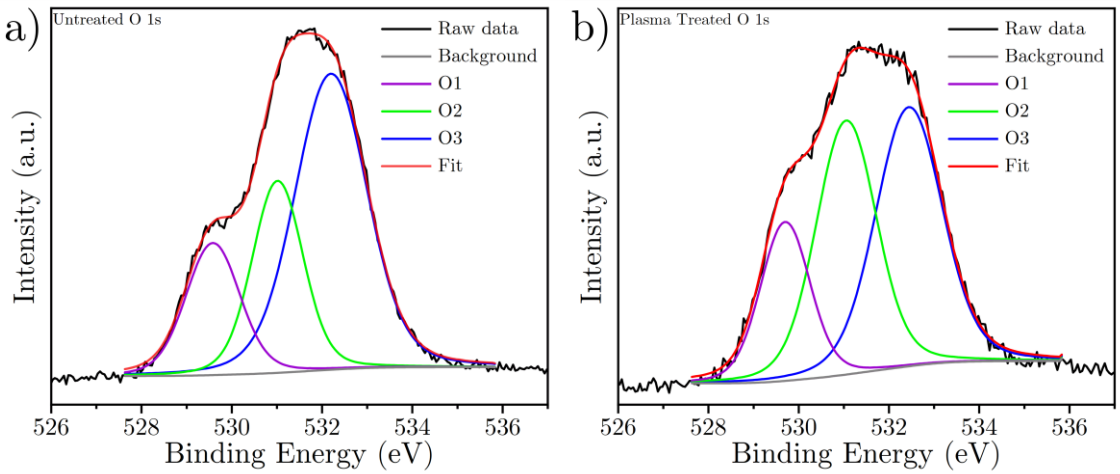

Figure 4-5 Oxygen O 1s spectra of (a) untreated and (b) plasma treated zirconia. After plasma treatment, there is a notable increase in the intensity of adsorbed surface hydroxyl groups (O2) and reduction of molecular water (O3), which suggests that more oxygen vacancies are present on the surface of the plasma treated zirconia.

Table 4-1 Normalised compositions of the different fitted components of the O 1s and Zr 3d spectra of untreated and plasma treated zirconia.

Spectra and Component		Composition (%)	
		Untreated	Plasma Treated
O 1s	O1	18.7 ± 0.3	19.5 ± 0.2
	O2	25.5 ± 0.2	37.8 ± 0.2
	O3	55.8 ± 0.3	42.7 ± 0.3
Zr 3d	Zr^{4+}	59.6 ± 0.1	30.7 ± 0.1
	Zr^{3+}	40.4 ± 0.1	69.3 ± 0.1

The Zr 3d spectra (Figure 4-6) exhibits two sets of doublet peaks ($3d_{3/2}$ and $3d_{5/2}$) corresponding to Zr^{4+} and Zr^{3+} in both untreated and plasma treated zirconia [23, 200, 224, 234]. Consistent with previous studies, the Zr $3d_{3/2}$ peak is observed at an energy approximately 2.4 eV higher than the Zr $3d_{5/2}$ peak for both oxidation states and sample types. Error analysis using Monte Carlo simulations demonstrates a high quality of fit, with a maximum deviation in area composition of 0.09% across all the modelled components for both spectra. The Zr^{4+} $3d_{5/2}$ peak remains relatively unchanged, with binding energies measured at 181.9 eV and 182.1 eV for untreated and plasma treated zirconia, respectively. Similarly, the Zr^{3+} $3d_{5/2}$ peak shows no significant shift, with fitted binding energies at 181.6 eV and 181.5 eV for untreated and plasma treated samples, respectively. As indicated under Table 4-1, the proportion of Zr^{3+} significantly increases following plasma treatment of the zirconia, shifting from 40.4 ± 0.1% (i.e., more Zr^{4+} than Zr^{3+}) to 69.3 ± 0.1% (more Zr^{3+} than Zr^{4+}) at the surface.

In combination with the observations from the O 1s spectra, these results indicate that the concentrations of Zr^{3+} and O2 increase, while the concentration of O3 decreases, which all suggest a substantial increase in oxygen vacancies on the surface of zirconia after plasma treatment.

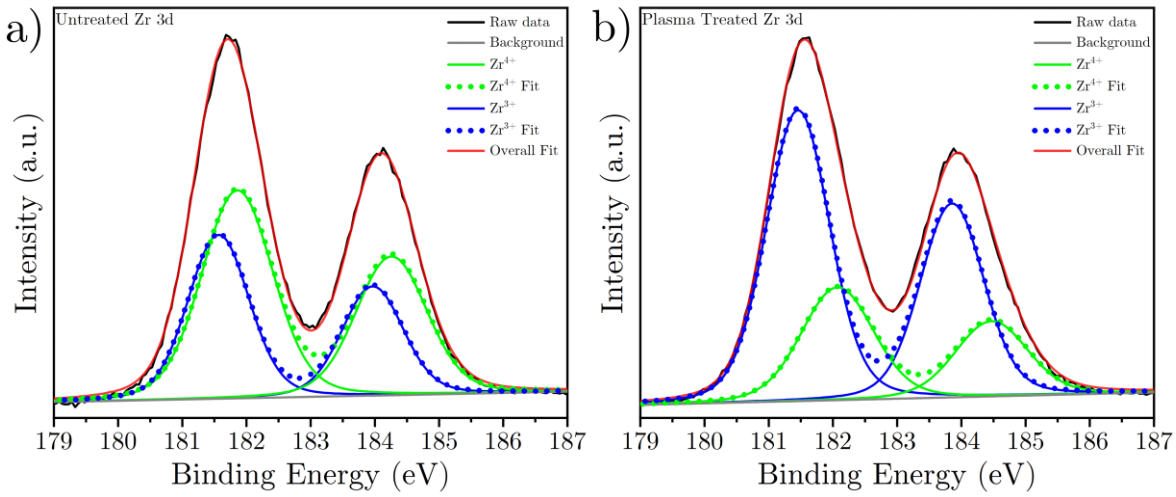

Figure 4-6 Zirconium Zr 3d spectra of (a) untreated and (b) plasma treated zirconia are exhibited, and reveal a significant shift in surface composition of Zr^{4+} and Zr^{3+}, with the reduced state dominating after plasma treatment. Consistent with the observations in Figure 4-5, the increased concentration of the Zr^{3+} components corroborate with the increase of oxygen vacancies.

4.3.2.3 Thermal analysis of oxygen-deficiency

The oxygen-deficient nature of the plasma treated zirconia was investigated using simultaneous TGA and DSC analysis in two consecutive stages: (1) heating from 100 to 500 °C and (2) isothermal holding at 500 °C for 10 hours. The thermal gravimetric (TG) curves during the heating process (Figure 4-7a) exhibit distinct differences between untreated and plasma treated zirconia. The untreated zirconia shows a simple trend with a linear increase in relative mass up to 425 °C, followed by a sharp reduction. In contrast, the plasma treated zirconia demonstrates a more complex curve

composed of a linear increase up to 240 °C, a slight plateau up to 300 °C, a further increase up to approximately 400 °C, before a final flattening of the curve close to 500 °C.

The corresponding heat flow curves (Figure 4-7a) closely reflect the relative mass changes of both samples. For the untreated zirconia, the heat flow remains predominantly flat (or slightly negative) up to 410 °C, corresponding to the linear mass gain region of the TG curve, followed by a gradual exothermic increase up to 500 °C (aligned with the reduction of relative mass). The mass loss and exothermic heat flow between 410-500 °C in the untreated sample can be attributed to the reduction (oxygen removal) of zirconia at elevated temperatures [254, 255].

On the other hand, the heat flow trend of the plasma treated zirconia remains (mostly) flat up to 275 °C, followed by an endothermic reaction between 275-400 °C and a subsequent plateau up to 500 °C. The presence of the endothermic reaction and reduction in relative mass between 275-400 °C is consistent with published phase diagrams of 3 mol% yttria-stabilised zirconia, indicating a monoclinic-to-tetragonal phase transformation within this temperature range [238, 254-256]. It is worth noting that no monoclinic phase was identified in the XRD or Raman analysis (Figure 4-3), and the limited deflection of the heat flow curve suggests the formation of only localised monoclinic crystals during the plasma treatment process, which may be buried within the noise of the XRD and Raman spectra. Further detailed analysis and identification of these findings in future studies could provide valuable insights into the reduction mechanism of plasma treatment, but it is beyond the scope of the current study.

Comparable thermal gravimetric (TG) and heat flow curves are obtained for both untreated and plasma treated zirconia during the isothermal holding at 500 °C for 10 hours (Figure 4-7b). Both sample types exhibit an initial reduction in mass, followed by a gradual increase for the remainder of the testing period. The untreated zirconia undergoes a larger reduction (0.85% loss at 75 minutes) and remains below the initial mass for a longer duration (6 hours) compared to the plasma treated zirconia (100 minutes, with a maximum loss of 0.21% at 45 minutes).

The heat flow curves for both samples remain relatively flat, indicating steady and continuous oxidation of the zirconia specimens at the higher temperature. However, the heat flow of the plasma treated zirconia is measured to be 520 ± 25% more exothermic across the final 5 hours of the holding stage, with an average heat flow of 0.0304 ± 0.0010 $mW.mg^{-1}$ (as compared with the 0.0049 ± 0.0005 $mW.mg^{-1}$ heat flow of the untreated zirconia). This suggests that significantly more oxidation (or re-oxidation) of the plasma treated zirconia takes place during the holding stage (i.e., $ZrO_{2-a} \rightarrow ZrO_{2-a+d}$, where d is the stoichiometric equivalent addition of oxygen) [233, 256].

This hypothesis is further supported by the greater final mass (101.00 ± 0.01% for plasma treated and 100.44 ± 0.01% for untreated zirconia) measured across the final 20 minutes of holding, as well as the more limited initial mass reduction of the plasma treated zirconia. Extrapolating the steady negative heat flow gradient of the plasma treated zirconia over the final 5 hours (Figure 4-7b; -1.04×10^{-5} $mW.mg^{-1}.min^{-1}$) suggests that approximately 38.24 additional hours of holding at 500 °C (for a total of 48.24 hours) are necessary for the plasma treated zirconia to reach the same heat flow as the untreated zirconia. On the other hand, the untreated zirconia reaches the final stable heat flow value of 0.0049 $mW.mg^{-1}$ after approximately 4 hours of

isothermal holding at 500 °C. This indicates that the plasma treated zirconia is approximately 12.1 times more oxygen-deficient than the untreated zirconia.

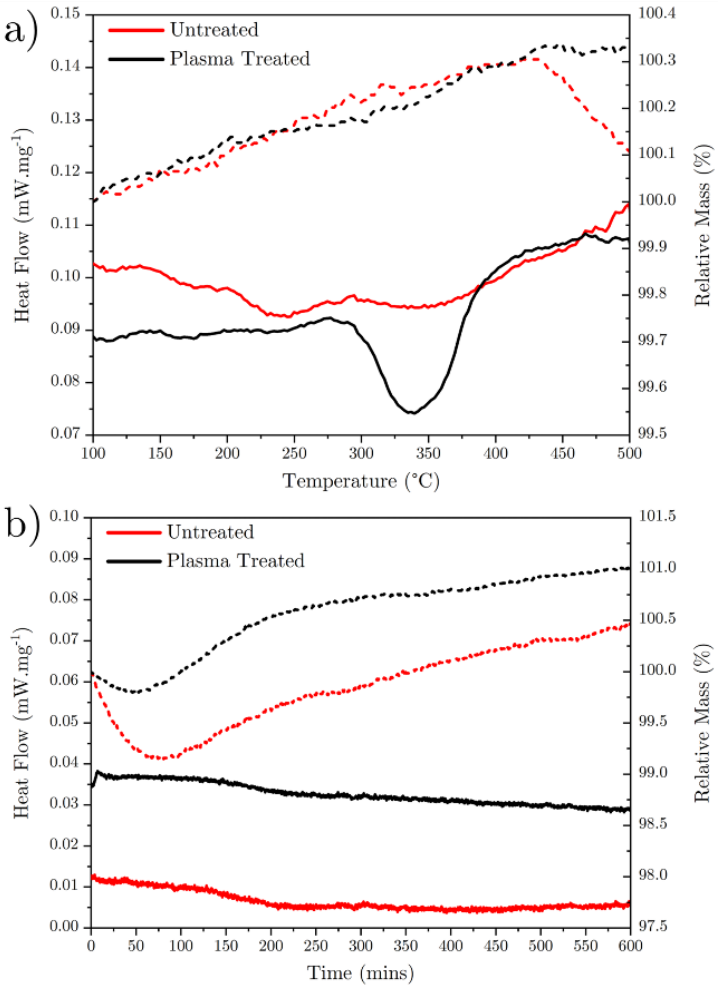

Figure 4-7 Heat flow (line) and thermogravimetric (dotted) curves for (a) non-isothermal heating to 500 °C and (b) isothermal holding at 500 °C of untreated and plasma treated zirconia. The plasma treated zirconia exhibits a more pronounced and sustained increase in mass under both testing methods. Additionally, an endothermic reaction (275-400 °C) is observed for the plasma treated zirconia during the heating up stage, which corresponds to a monoclinic-to-tetragonal phase transformation. The relative mass is normalised with respect to the measured mass at the start of each respective stage.

4.3.3 Optical absorption capability and electronic band structure

In the case of oxygen-deficient zirconia (ZrO_{2-a}), the introduction of oxygen vacancy defects has shown potential for modifying the intrinsic electronic characteristics, and thus, influencing the electronic band structure, the bandgap (E_g) and the Fermi level (E_f) of the material [199, 211, 257]. By creating oxygen vacancies with 0 or 1 trapped electrons (i.e., F^{2+} and F^{+} centres, respectively), nearby Zr^{4+} ions can be reduced to Zr^{3+} to maintain charge neutrality (as demonstrated in equations 4-equation 4-2 and 4-equation 4-3). This reduction of zirconium cations results in the occupation of the 4d energy level in Zr ions, raising the lowest occupied energy level. Due to the various interatomic interactions (e.g., orbital hybridisation, changes in electrostatic potential), this reduction of zirconium cations significantly affects the electronic properties of the bulk material.

Density functional theory (DFT) studies have indicated that this reduction leads to the formation and occupation of new energy states, primarily originating from Zr 4d orbitals, which are approximately 1.2-1.6 eV below the conduction band (CB) of pristine zirconia [198, 206, 208, 211, 216, 234, 242, 249, 257]. Consequently, this shifts the E_f to a higher energy, reducing the bandgap between the top edge of the valence band (VB) and the bottom edge of the CB. This reduction of the bandgap transforms electrically insulating zirconia into an n-type semiconductor capable of absorbing visible light [252]. Moreover, these newly formed states within the bandgap primarily interact with the conduction band, leading to the trapping of electrons near the CB (trap-assisted recombination). This, in turn, reduces the recombination rates between excited electrons in the CB and holes in the lower energy states of the VB [201, 216, 258]. Consequently, the electron's lifetime in the conduction band is prolonged,

allowing for enhanced absorption of photons across a wider range of energies [208, 214, 234, 239].

Consistent with previous studies on oxygen-deficient zirconia, the plasma treated zirconia in this research exhibit excellent light absorption properties, as observed through both Raman analysis (Figure 4-3b) and diffuse reflectance spectroscopy (DRS; Figure 4-8) [199, 200, 211, 216, 234, 239, 242, 249]. Although Raman analysis was conducted using monochromatic light at 532 nm, the average area of each deconvoluted component of the plasma treated zirconia demonstrated a significant enhancement in light absorption, with an average area reduction of 79.6 ± 3.6% compared to untreated zirconia. Furthermore, the plasma treated zirconia exhibited an average light absorption of 73.2 ± 5.7% across the entire DRS range (200-3000 nm), whereas the untreated zirconia only absorbed 44.1 ± 8.5% of the light. This corresponds to a 66.2% increase in light absorption capability of the plasma treated zirconia throughout the natural sunlight spectrum.

Moreover, the untreated white zirconia only exhibited notable optical absorption capability in the short-wave ultraviolet (UV) region (Figure 4-8), with maximum absorption at approximately 240 nm (equivalent to ≈5.1 eV), consistent with previous studies on the bandgap of zirconia [197, 198, 242]. In contrast, the black plasma treated zirconia demonstrated excellent (>65%) absorption across the entire spectrum, including the shortwave infrared (SWIR) range. This represents a significant enhancement in light absorption capability for the plasma treated zirconia, surpassing the performance of oxygen-deficient zirconia reported in other studies, many of which focused on the absorption capabilities of their zirconia materials at wavelengths below 700 nm (UV and visible range). It is worth noting that while UV and visible radiation carry higher energy density compared to near-infrared (NIR) or SWIR radiation, natural

sunlight is comprised of only 5% UV (300-400 nm) and 43% visible (400-700 nm), with the remaining 52% consisting of the different categories of infrared (700-2500 nm) radiation. Therefore, the sustained absorption across the entire solar spectrum holds tremendous potential for future efficient solar energy harvesting (i.e., high yield) using plasma generated oxygen-deficient zirconia.

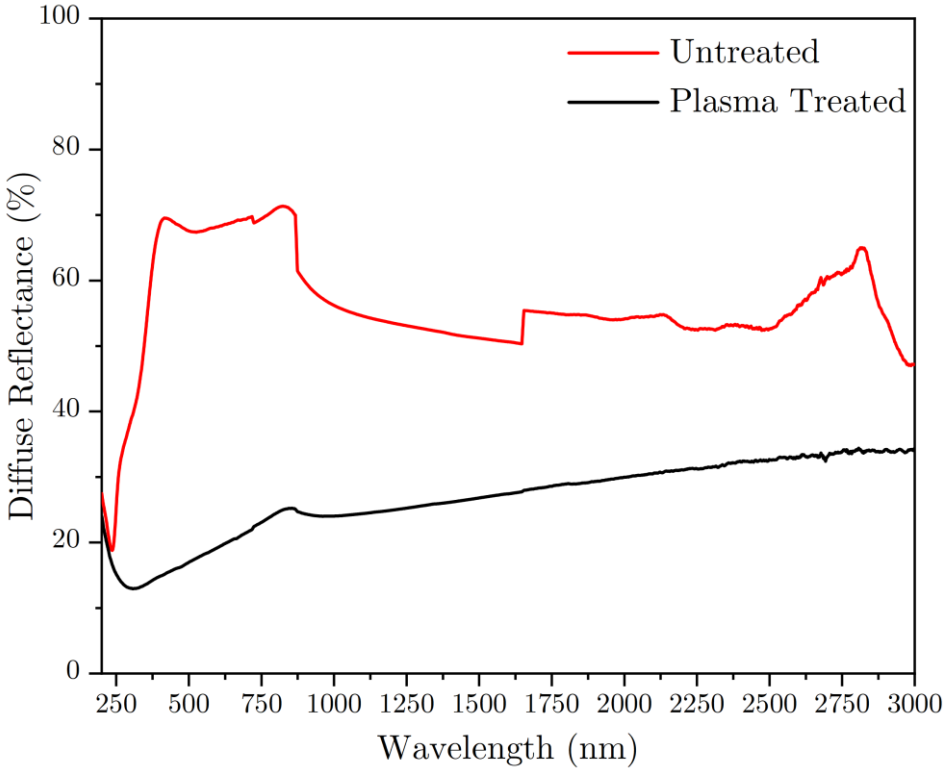

Figure 4-8 Diffuse reflectance spectroscopy of untreated and plasma treated zirconia in the wavelength range of 200-3000 nm. The reflectance spectrum of untreated zirconia demonstrates strong reflection (indicating weak absorption) at longer wavelengths, while only exhibiting pronounced absorption at approximately 240 nm (corresponding to a bandgap of ≈5.1 eV). In contrast, plasma treated zirconia exhibits a substantial decrease in reflected light (indicating strong absorption), with less than 35% reflection observed across the entire spectrum.

By applying the Tauc method and Kubelka-Munk function (as described in section 4.5.3 of the supporting information), the $(F(R)h\nu)^{1/\gamma}$ values were calculated for both

untreated and plasma treated zirconia (Figure 4-9a & b) [232, 259]. This analysis revealed the direct (γ = ½) and indirect (γ = 1) bandgaps of the untreated and plasma treated zirconia. Consistent with previous literature, the untreated zirconia of this study was extrapolated to have a direct bandgap of 4.84 eV and an indirect bandgap of 3.19 eV [234, 260-262]. In contrast, the plasma treated zirconia demonstrated significantly reduced direct and indirect bandgaps, measuring 2.61 eV and 1.45 eV, respectively. These findings align with the expected formation of new bandgaps resulting from the introduction of oxygen vacancies and reduction of zirconium cations. It is important to note that the plasma treated zirconia did not exhibit a complete plateau or zero absorption value under both direct and indirect curves, indicating the presence of a complex band structure (beyond what is depicted in Figure 4-10) that could be ascribed to increased trap-assisted recombination events [201, 214, 239]. As proposed by Qi *et al.* [242], the generation of interstitial zirconium (I_{Zr}) defect sites can also contribute to the reduction of the bandgap. Furthermore, Qi *et al.* [242] also suggested that I_{Zr} defects primarily enhance longer-wavelength light absorption, such as in the NIR range, while oxygen vacancies promote light absorption across a broad spectrum, with the greatest enhancement in the UV and visible regions [217]. Considering the strong light absorption of the plasma treated zirconia across the wide spectrum (including the SWIR region) and the complex electronic band structure, it is plausible that the plasma treatment of zirconia gives to simultaneous formation of oxygen vacancies and interstitial zirconium migration. However, further investigations are needed to explore this hypothesis in detail.

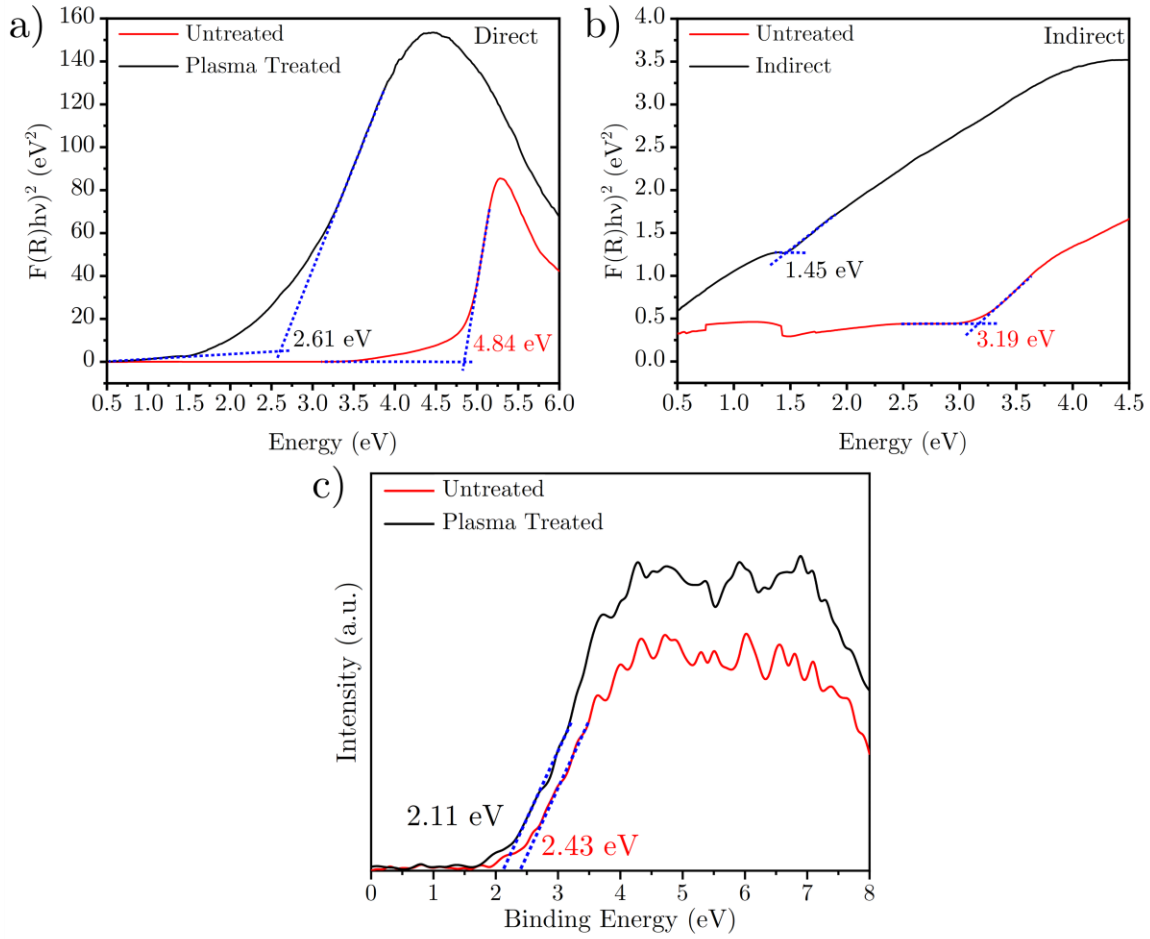

Figure 4-9 (a) Direct bandgap (Eg), (b) indirect bandgap, and (c) valence band positions of untreated and plasma treated zirconia. The E_g values are approximated using a combined Tauc method and Kubelka-Munk function, plotted against photon energy. Plasma treated zirconia exhibits significant reductions in both direct bandgap (from 4.84 eV to 2.61 eV) and indirect bandgap (from 3.19 eV to 1.45 eV) compared to untreated zirconia. The absence of a complete plateau or zero absorption value indicates a complex band structure with localised bandgaps that vary considerably. Additionally, the valence band positions of zirconia shift upward towards the conduction band (i.e., lower binding energy) following plasma treatment.

Low binding energy XPS measurements (Figure 4-9c) were conducted to determine the VB positions of untreated and plasma treated zirconia. The results showed that

the top edge of the VB for untreated zirconia was at 2.43 eV, while for plasma treated zirconia, it was at 2.11 eV (vs. normal hydrogen electrode (NHE)) [263]. By combining these VB energies with the previously measured direct (Figure 4-9a) and indirect (Figure 4-9b) bandgap energies, it was possible to estimate the energy of the bottom edges of the CBs and construct energy band diagrams, as shown in Figure 4-10. The bottom edges of the CBs for untreated zirconia were measured to be at -2.41 eV (direct) and 0.76 eV (indirect), while for plasma treated zirconia, they were found to be at -0.50 eV (direct) and 0.66 eV (indirect). The observed rise of the VB (-0.32 eV) and the significant tailing of the bottom edge of the CB (1.91 eV for direct and 1.42 eV for indirect bandgaps) in plasma treated zirconia indicate a relative shift of the E_f towards the CB. These findings are consistent with previous studies on oxygen-deficient zirconia, both theoretical and experimental, that suggest the formation of a new donor intra-bandgap level (close to the CB) following the transformation of zirconia due to increasing oxygen-deficiency and reduction of Zr cations [242, 258, 264].

It has been observed that untreated zirconia lacks intra-bandgap states between the VB and the CB, and the top of the VB is primarily composed of electrons in the oxygen 2p (O 2p) orbital [198, 199]. However, plasma treatment of zirconia leads to the creation of vacant oxygen sites, reducing the availability of O 2p orbitals for electron occupation or hole formation. Simultaneously, the reduction of zirconium results in electron occupation of the zirconium 4d orbital, forming an intra-bandgap state close to the bottom of the CB and causing the upward movement of the E_f [242, 249]. The reduced bandgap between the Zr 4d energy level and the CB leads to a higher electron density in the CB and an increased density of holes in the Zr 4d energy level (resulting from excitation of Zr 4d electrons into the CB).

Due to the occupation of Zr 4d orbitals and the limited availability of O 2p orbitals, electrons tend to be trapped near the CB and recombine with holes in the VB at a slower rate (due to continuous excitation and relaxation events between the Zr 4d orbital and the CB). This results in a reduced formation of holes in the VB and an increased occupation of electrons in the CB, leading to n-type conductivity in plasma treated zirconia (where electrons predominantly carry electrical current) [24, 208, 255, 258].

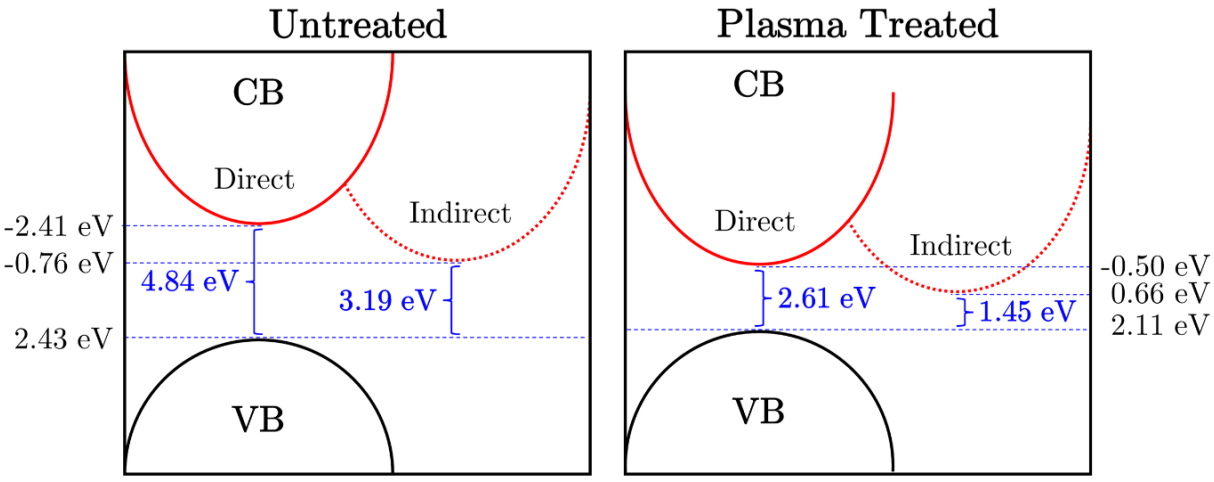

Figure 4-10 Calculated energy band diagrams (vs. NHE) of untreated and plasma treated zirconia (using values measured in Figure 4-9). Following plasma treatment of the zirconia, the combined downwards movement of the conduction bands (CB) and the slight upwards shift of the valence band (VB) give rise to significantly smaller bandgaps (approximately halved) for both direct (going from 4.84 eV to 2.61 eV) and indirect (going from 3.19 eV to 1.45 eV) transitions.

4.3.4 Future perspective of plasma defect-engineering of zirconia

The significant capability and efficiency of plasma treatments for modifying the electronic band structure and optical properties of fully dense zirconia offer promising

prospects for scalable, cost-efficient, rapid, and environmentally friendly production of n-type semiconducting zirconia. The adaptability and close control of plasma treatments also open avenues for future optimisation and expansion of this production route. By adjusting various treatment parameters such as temperature, gas mixture, gas pressure, electrode material, electrode power, and treatment configuration, tailored treatments can be developed for different applications, further improving upon the treatment method used in this study [22, 265-267]. It is important to note that the choice of hydrogen plasma treatment in this study was selected for its simplicity, with the primary objective of demonstrating the potential of low-pressure plasma treatment to rapidly produce oxygen-deficient zirconia with a low bandgap.

One unique advantage of low-pressure plasma technologies, unlike traditional electrochemical methods, is the ability to physically separate the anode and cathode electrodes, even across large distances [22, 182]. This separation is facilitated by the continuous presence of an electrically conductive gas medium during the treatment process. This characteristic opens the prospect to overcome the layer separation phenomenon typically associated with equivalent electrochemical techniques for the formation of oxygen-deficient zirconia. In low-temperature electrochemical methods [228], there is a tendency to form a tri-layer configuration, consisting of (1) n-type conductivity (with high oxygen vacancy and cation reduction) at the cathodic side, (2) p-type conductivity (with high vacancy occupation and low cationic reduction) at the anodic side, and (3) a largely unmodified layer with ionic conductivity at high temperatures sandwiched between the layers (1) and (2).

Considering that, in low-pressure plasma treatments, the electrodes are physically separated, the electrical potential gradient across the anode and cathode is distributed over a larger distance. As a result, there is minimal electrical potential variation in the

vicinity of each electrode, which can enable the formation of solely n-type or p-type semiconducting zirconia, depending on the electrode in contact with the material. This has the potential to offer greater flexibility and control when producing semiconducting zirconia materials.

This study serves as a fundamental basis for future advancements in the field of low-pressure plasma treatments, specifically for the development of novel bulk transformed semiconducting zirconia materials. The findings and insights gained from this research can pave the way for the design and optimisation of more complex and industrially viable plasma treatments. The properties and structure of our material suggest that it could be a promising candidate for photocatalysis. However, dedicated experiments are necessary to prove this, which are beyond the scope of this paper and should be considered in future research. By building upon this study, it may also be possible to extend the application of low-pressure plasma treatments to other materials, opening new opportunities for innovative production and development of materials.

4.4 Conclusions

This study focuses on the novel hydrogen plasma treatment of 3 mol% yttria-stabilised zirconia and investigates its impact on light absorption capability and energy band structure. The research encompasses various analyses, including visual, magnetic, electronic, and thermal assessments, to examine the formation of oxygen vacancies, colour transformation, and structural characteristics of the plasma treated zirconia. The following conclusions can be drawn from this study:

After subjecting zirconia to hydrogen plasma treatment at 500 °C for 5 hours, a bulk transformation occurs, changing the colour from pristine white to metallic black.

Combined DSC and TGA analysis reveal the limited presence of the monoclinic phase in plasma treated zirconia, indicated by a monoclinic-to-tetragonal phase transition between 275-400 °C. However, no significant crystallographic or structural changes, such as atomic spacing or bonding environment, are observed across large regions.

EPR analysis shows the formation of two new signals corresponding to the presence of Zr^{3+} cations in plasma treated zirconia. The lack of change in signal at g-tensor value of ≈2.004 suggests that the reduction of zirconium primarily leads to the formation of diamagnetic F^{2+} ($V_O^{\cdot\cdot}$) centres.

XPS analysis demonstrates significantly increased concentrations of oxygen vacancies and reduced zirconium ions (Zr^{3+}) in plasma treated zirconia, as evidenced by changes in O 1s and Zr 3d spectra.

Thermal analysis using DSC and TGA shows continuous exothermic heat flow and mass gain in plasma treated zirconia. Extrapolated estimations indicate that re-oxidation of the zirconia back to its untreated state would require approximately 48

hours of holding at 500 °C in air. This corresponds to 12.1 times greater oxygen-deficiency in plasma treated zirconia.

Plasma treated zirconia exhibits significantly higher light absorption across the entire sunlight spectrum (200-3000 nm) compared to untreated zirconia. The average measured light absorption for plasma treated zirconia is 73.2 ± 5.7%, whereas it is 44.1 ± 8.5% for untreated zirconia. Moreover, plasma treated zirconia demonstrates >65% light absorption for all wavelengths within the tested spectrum.

Plasma treatment leads to a significant reduction in both the direct and indirect bandgap values of zirconia. The direct bandgap decreases from 4.84 eV to 2.61 eV, while the indirect bandgap decreases from 3.19 eV to 1.45 eV. Consistent with previous literature, these changes indicate an upward shift of the valence band edge and a downward shift of the conduction band edge.

Considering the notable benefits offered by low-pressure plasma treatments, such as their ability to accommodate various specimen geometries and minimal electrical potential gradient across the workpiece, we anticipate that our findings will facilitate the cost-effective and efficient production of oxygen-deficient zirconia for advanced energy materials. In future studies, it would be worthwhile to explore the influence of plasma treatment on the mechanical properties of zirconia, particularly fracture toughness and hardness, which are crucial performance indicators that distinguish zirconia from other ceramic materials. Such investigations will contribute to improving the understanding of the effects of plasma treatment on the overall performance of zirconia materials.

4.5 Supplementary materials

4.5.1 Raman Spectroscopy

The Raman spectra of both untreated and plasma treated zirconia were analysed by deconvolution to estimate the intensity contributions of the B_{1g}, E_g and A_{1g} vibrational modes. Table 4-2 presents a comparison of the peak centre, full width at half maximum (FWHM), and area measurements of the fitted components for each vibrational mode. Despite a substantial area reduction of each modelled component following plasma treatment (79.6 ± 3.6%), minimal changes were observed in the peak centre positions and FWHM values. This indicates a significant enhancement in the light absorption capability of plasma treated zirconia while maintaining its structural integrity.

Table 4-2 Peak centre, FWHM and area measurements of the deconvoluted Raman spectra of untreated (U) and plasma treated (PT) zirconia. Absolute difference (Δ) between the two sample types, as well as the averaged values and standard deviations for each component, are also provided.

		B_{1g}		E_g			A_{1g}
		1	**2**	**1**	**2**	**3**	**1**
Peak Centre (cm^{-1})	**U**	147	324	260	465	643	609
	PT	147	323	260	465	643	610
FWHM (cm^{-1})	**U**	6.8	12.3	14.7	15.2	13.4	23.2
	PT	6.7	12.8	14.8	14.1	11.8	24.1
Area (a.u.)	**U**	5798	4217	23290	8666	16589	8974
	PT	1379	1023	5028	1288	3125	1700
	Δ (%)	76.2	75.7	78.4	85.1	81.2	81.1

4.5.2 X-ray Photoelectron Spectroscopy (XPS)

4.5.2.1 Fitting Parameters & Validation

Shirley-type fitting was employed to account for the background contribution in all XPS spectra. The Zr 3d spectra were deconvoluted with strict fitting constraints, including a 2:3 area ratio of $3d_{3/2}$ to $3d_{5/2}$, equal FWHM of the doublet peaks, and fixed position constraints of the doublet peaks ($3d_{3/2}$ at 2.4 eV higher value than $3d_{5/2}$). Conversely, since the O 1s spectra only exhibits single peaks, no specific constraints were applied during the deconvolution process. However, careful consideration was given to reject any fitted O 1s models with unrealistic FWHM values. The FWHM of all fitted components in the study ranged between 1.3-1.9 eV, and comparable results were observed for both the untreated and plasma treated samples. To assess the potential influence of randomly generated noise on the fitted spectra and to validate the modelled components, Monte Carlo error analysis was conducted. The overall composition of each sample surface was evaluated by comparing the area contributions of each fitted component (individual components for O 1s and doublet components for Zr 3d) against the total area of all fitted components (using the same approach for O 1s and Zr 3d). Table 4-3 shows an overview of the final fitting parameters (including error estimates) and compositions of the O 1s and Zr 3d XPS spectra.

Table 4-3. Peak position, FWHM, area percentage of the deconvoluted O 1s and Zr 3d XPS spectra of untreated (U) and plasma treated (PT) zirconia.

Spectra	Component & Oxidation State		Modelled Peaks					
			Position (eV)		FWHM (eV)		Area (%)	
			U	PT	U	PT	U	PT
O 1s	O1	-	529.6	529.7	1.41	1.30	18.67 ± 0.26	19.48 ± 0.24
	O2	-	531.0	531.1	1.33	1.58	25.52 ± 0.15	37.81 ± 0.17
	O3	-	532.2	532.4	1.88	1.74	55.81 ± 0.25	42.71 ± 0.27
Zr 3d	$3d_{3/2}$	4+	184.3	184.5	1.31	1.33	23.84 ± 0.04	12.27 ± 0.06
		3+	184.0	183.9	1.12	1.17	16.16 ± 0.04	27.73 ± 0.06
	$3d_{5/2}$	4+	181.9	182.1	1.31	1.33	35.76 ± 0.06	18.41 ± 0.09
		3+	181.6	181.5	1.12	1.17	24.24 ± 0.06	41.59 ± 0.09

4.5.2.2 O 1s Peak Assignment

Deconvolution of the O 1s spectra reveals three distinct peaks in both untreated and plasma treated zirconia, denoted as O1, O2, and O3, respectively [200]. The O2 and, occasionally, O3 peaks in the O 1s spectra are assigned to the presence and density of oxygen vacancies in various metal oxides [253, 268]. However, the inability to directly detect photoelectron emissions from vacant atoms (i.e., oxygen vacancies) has raised doubts regarding the direct correlation of the O2 and O3 peaks with oxygen vacancies. Some studies have proposed that the appearance of the O2 and O3 peaks

may correspond to a shift of the O1 peak (towards higher binding energy) due to the altered electron cloud of oxygen atoms near a vacant oxygen site [269]. However, a recent density functional theory (DFT) study by Bosio *et al.* [251] on the changes in the O 1s binding energy of ceria under different conditions revealed only minor shifts in the O 1s peak following the formation of oxygen vacancies (and reduction of cerium ions), while substantial shifts occurred after modifying the chemical state of the surface (e.g., formation of hydroxyl or carbonate groups). This model is further supported by Lackner *et al.* [250], who observed similar shifts in the O 1s binding energy (via XPS) upon water adsorption on zirconia films. In their study, the O2 and O3 peaks were attributed to surface adsorbed hydroxyl groups (dissociated water) and molecular water (non-dissociated water) [249]. Consistent with these recent findings, the three components of the O 1s spectra in this study have been assigned to lattice oxygen in zirconia (O1), surface adsorbed hydroxyl groups (O2), and surface adsorbed molecular water (O3).

4.5.3 Optical Bandgap Calculation

To approximate the bandgap of the (relatively) thick zirconia material through diffuse reflectance spectroscopy (DRS) measurements, both the Tauc method (equation S 4-1) and the Kubelka-Munk function (equation equation 4-2) were utilised [230]. The Tauc method assumes a linear correlation (with a rate of B) between the degree of light absorption ($\alpha h\nu$) of a specific electronic transition type (e.g., direct allowed or indirect allowed) and the difference between the material's bandgap and the photon energy ($h\nu - E_g$), as long as $h\nu > E_g$. Thus, no light absorption is expected below the bandgap energy of the material. Experimentally, the Tauc plot can be used to estimate the bandgap by extrapolating the linear region to the base of the graph (i.e., $\alpha h\nu = 0$). However, the Tauc method was originally designed for thin films and does not account

for scattering effects. In thicker specimens, scattering becomes more significant and can lead to inaccurate extrapolated bandgap measurements.

According to the Kubelka and Munk theory, the reflectance spectra of an infinitely thick sample (R_∞, where R is typically >1 mm) can be converted to absorption spectra using the Kubelka-Munk function (F(R)). By replacing α in the Tauc method with F(R), it becomes possible to estimate the bandgap of relatively thick samples (equation 4-3). For direct allowed and indirect allowed (involving phonons) electronic transition bandgaps, the γ coefficient should be changed to ½ and 2, respectively [230, 231].

It is important to note that when multiple materials and/or phases/stoichiometries are present that can absorb light within the testing range, estimating the bandgap through linear extrapolation to the base of the graph is inaccurate and often leads to underestimation of the bandgap. As suggested by Makuła *et al.* [232], to overcome this limitation, the bandgap of the material can be predicted by identifying the intersection point between the linear regions below and above the bandgap transition energy. This can be achieved by using tangents of each linear segment to determine the point of intersection.

$$(\alpha \cdot h\nu)^{1/\gamma} = B(h\nu - E_g) \qquad \text{(S 4-1)}$$

where α is the absorption coefficient, h is Plank's constant, ν is the frequency of the photon, γ is selected following the electronic transition type (½ for direct allowed and 2 for indirect allowed), B is a constant, and E_g is the optical bandgap.

$$F(R) = \frac{(1-R_\infty)^2}{2R_\infty} \qquad \text{(S 4-2)}$$

where $F(R)$ is the Kubelka-Munk function and R_∞ is the measured reflectance value. By replacing α in equation S 4-1 with $F(R)$ obtained from equation 4-2, it is possible to obtain equation 4-3 for estimating the bandgap of thick specimens.

$$(F(R)h\nu)^{1/\gamma} = \frac{(1-R)^2}{2 \cdot R} \qquad \text{(S 4-3)}$$

Chapter 5 Processing Conditions and Mechanisms for The Plasma Defect-Engineering of Bulk Oxygen-Deficient Zirconia

Note: The work presented in this chapter has been published in the peer-reviewed **Journal of Materials Research and Technology** (Vol 29, Pages 3759-3770) [18]**.**

Contribution: (Conceptualization: equal; Data curation: Lead; Formal analysis: Equal; Investigation: Lead; Methodology: Supporting; Validation: Equal; Writing – original draft: Lead; Writing – review & editing: Equal).

Abstract

In recent years, the utilisation of oxygen-deficient zirconia ($ZrO_{2-\alpha}$), commonly referred to as black zirconia, has garnered considerable attention due to its potential applications for solid oxide fuel cells (SOFCs), gas sensors, biomedical implant materials, and photocatalysis. However, current methods employed to manufacture $ZrO_{2-\alpha}$ exhibit noticeable limitations regarding their scalability, environmental sustainability, and cost-effectiveness. Our recent work has successfully demonstrated the feasibility for bulk conversion of conventional white zirconia into oxygen-deficient black zirconia through direct current (DC) plasma treatment (i.e. plasma blackening). This study elucidates the conditions for plasma blackening and provides a unique mechanism for the bulk transformation of zirconia. A systematic investigation of different plasma technologies (DC, active-screen plasma), treatment configurations (contact conditions, cathode material, and cathode potential), and treatment parameters (voltage, temperature, duration) uncover the crucial variables that influence the feasibility and rate of the reduction process. The reduction of zirconia is shown to initiate from localised contacting points at the cathode-facing surface and grow, with a hemispherical shape, towards the anode-facing surface. A series of development stages are proposed for the process, namely: bulk oxygen vacancy conductance, surface activation, oxygen vacancy generation and a moving cathode front. The findings of this study provide insights into the underlying mechanisms involved in the bulk-reduction of zirconia and help to pave the way towards future scalable and cost-effective generation of oxygen-deficient zirconia.

5.1 Introduction

The reported photocatalytic behaviour of black titanium oxide (TiO_{2-x}) has led to a surge of interest in equivalent black zirconia, known as oxygen-deficient black zirconia ($ZrO_{2-\alpha}$), as a potential alternative next-generation photocatalytic material [270]. The desirable photocatalytic properties of these defect-engineered metal oxide materials have been attributed to an abundance of oxygen vacancies, which generate new mid-gap states around the Fermi level and are accompanied by the remarkable change in optical properties (e.g., change of colour) [8, 15]. This approach widens the application range and potential value of black oxygen-deficient ($ZrO_{2-\alpha}$) as an energy harvesting material, for the generation of hydrogen, for the decomposition of pollutants, and for medical applications (e.g., tumour therapy) [7, 9, 14].

The phenomenon of colour change is particularly prevalent in specific metal oxides, such as zirconia and titania, renowned for their remarkable capacity to exhibit diverse colours in the presence of cationic dopants [91, 271-275]. Consequently, early research has focused on controlling and fine-tuning the colours of these materials by manipulating the types and concentrations of dopants using various methods, including high-temperature sintering, sol-gel processes, and coprecipitation [132, 276, 277].

Subsequent investigations have revealed that the augmentation of optical absorption intensity and photocatalytic activity of zirconia is intimately linked to the presence of surface oxygen vacancies [275, 278-283]. Consequently, this has directed researchers to focus on the effective reduction of zirconia. Although zirconium has a relatively strong affinity for oxygen, a diverse array of elements (e.g., calcium, iron, yttrium) do exist that can extract oxygen from zirconia, while simultaneously reduce zirconium

ions (Zr^{4+} to Zr^{3+}) [8, 284]. Different approaches have been explored, including chemical reduction using methods such as molten lithium reduction, magnesiothermic reduction in the presence of 5% H_2/Ar, reduction of zirconium (IV)-n-propoxide (ZrP) solution through sol-gel synthesis and high-pressure torsion [14, 17, 270, 285-289]. However, these methods for generating blackened zirconia are characterised by several inherent limitations, including long production cycles, use of hazardous chemical reagents, low efficiency, high energy consumption, and environmental concerns (e.g., disposal of chemical reagents). Furthermore, the majority of the reduced black zirconia manufactured under these approaches are in powder form and require sintering into bulk components for applications demanding structural integrity, specific geometries and resistance to mechanical stresses. Re-oxidation is difficult, if not impossible, to avoid when sintering oxygen-deficient zirconia, and therefore predominantly limits the use of the material to its powder form [8, 17, 290].

To address these technological and environmental challenges, the authors of this study have recently successfully reported a novel approach employing low-pressure plasma to produce bulk oxygen-deficient zirconia with excellent broad spectrum light absorption capability [12]. However, as only a single DC plasma treatment condition (500 °C at 300 Pa for 5 h in 100% H_2) has been reported thus far, the underlying mechanisms involved, and the influence of different treatment conditions are not yet established.

Consequently, this study aims to investigate the underlying mechanisms involved through systematic evaluation of the role of different treatment parameters on the generation of oxygen-deficient zirconia. These parameters include different types of plasma technologies (DC plasma and active-screen plasma), DC plasma treatment configurations (contact conditions and cathode material), and plasma treatment

conditions (voltage, temperature and duration). It is expected that the outcomes of this investigation will both advance scientific understanding of the mechanism involved in the plasma blackening of zirconia and contribute to the future development and optimisation of this novel, cost-effective, and environmentally friendly plasma defect-engineering manufacturing route.

5.2 Methods

5.2.1 Sample preparation

The samples used in this study were cut from 3 mol-% yttria-stabilised tetragonal zirconia rods into cylindrical coupons with a thickness of 3 mm and a diameter of 10 mm using a Struers Accutom 50 machine and a cubic boron nitride cutting wheel. The cylindrical coupon samples were ground to #1200 grit size SiC paper before polishing using diamond suspensions with particle sizes of 6, 3, and 1 μm.

5.2.2 Plasma treatment configurations

The plasma treatments were performed using a Klöckner Ionon 40 kVA plasma furnace. Specific overviews of the difference treatment setups, treatment parameters and treatment configurations utilised in this study are described in the following sections.

5.2.2.1 Plasma treatment setups

To investigate the effect of direct cathode power of the worktable (where the sample is placed), both DC (direct current) plasma and active-screen (AS) plasma setups were employed. The samples were placed directly onto the worktable connected to the cathode in the DC plasma treatment setup (Figure 5-1a), while the samples were electrically isolated from the cathode (i.e., at a floating potential) in the AS plasma treatments. An AISI 316 austenitic stainless steel mesh cage and a screen connected to the cathode, known as the active screen, were placed around the isolated sample in the AS plasma treatment (Figure 5-1b). A distance of 20 mm was kept between the sample surface and the active screen lid. Both DC and AS plasma treatments were carried out at 500 °C for 5 h in H_2 gas at 3mbar (300Pa).

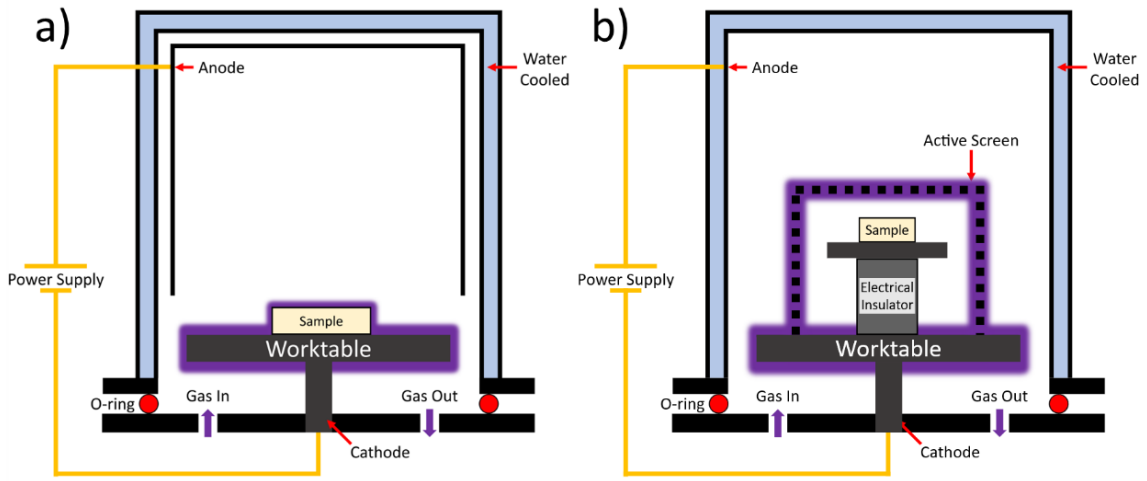

Figure 5-1. Schematic diagram of (a) DC and (b) AS plasma treatment setups [186].

5.2.2.2 Plasma treatment parameters

The effect of DC plasma treatment parameters on the blackening of zirconia were systematically studied using a range of the treatment temperatures (ranging from 100 to 500 °C) and treatment durations (30 and 300 min).

Investigations related to the effect of treatment voltages were carried out between 370 and 450 V. Given that the furnace voltage and the chamber temperature are inherently linked (with larger temperatures requiring larger DC voltages), it was necessary to incorporate auxiliary heating sources to isolate the two key variables. Consequently, a secondary DC power supply (TRUMPF TruPlasma DC 3005) was employed to enable the initial heating up ramp to be conducted without any power to the sample and to compensate for the varying thermal power provided by the different applied voltages. In this approach, the furnace power was used as an auxiliary heating source (indirectly heating samples and maintaining the chamber temperature), while the secondary DC power source acted as the main cathode power source (Figure 5-2).

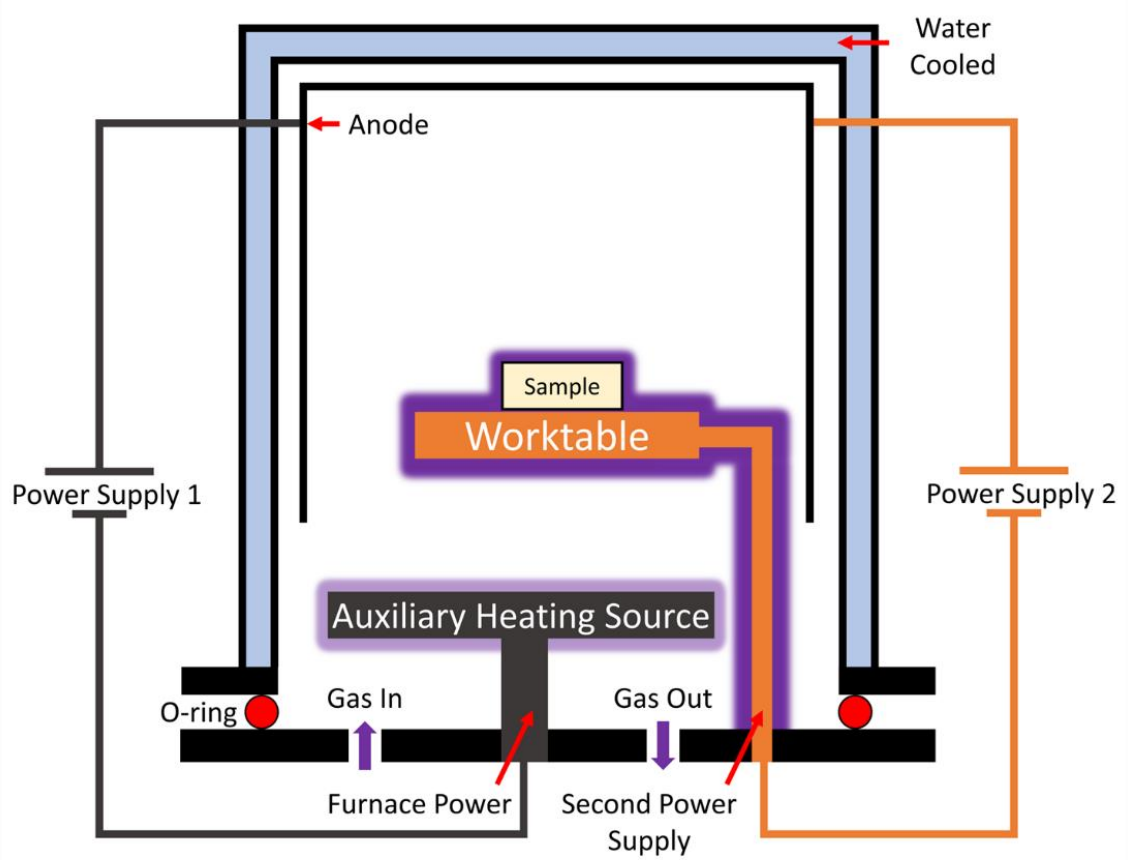

Figure 5-2. Schematic diagram of the plasma treatment setup with two DC power sources.

5.2.2.3 Plasma treatment configurations

To verify whether the cationic doping from the metallic ions in the steel worktable was dictating the treatment of zirconia, separate plasma treatments were performed (at 500 °C for 5h) using worktables composed of zirconium (Zr 702) and AISI 316 stainless steel (as shown in Figure 5-3).

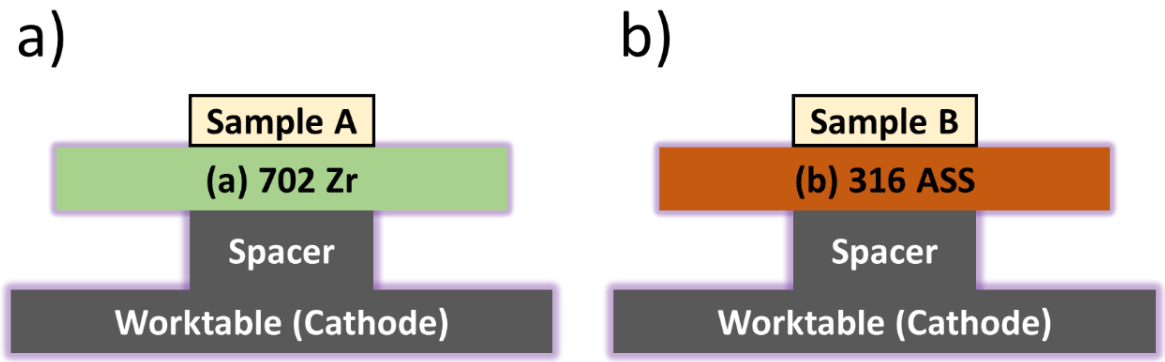

Figure 5-3. Schematic diagram of DCP treatment with different sample worktable materials: (a) Zr702 and (b) AISI 316 stainless steel.

Similarly, to study the influence of contact conditions on the initiation of the black spots on the cathode-facing surface, two different AISI 316 stainless steel base samples were designed with and without blind holes (as depicted in Figure 5-4). The diameter of each stainless-steel block was chosen to match the size of the sample (to limit the formation of hollow cathodes at the bottom edges of the samples). The temperature was set at 200 °C, and the durations chosen were 30 and 300 min.

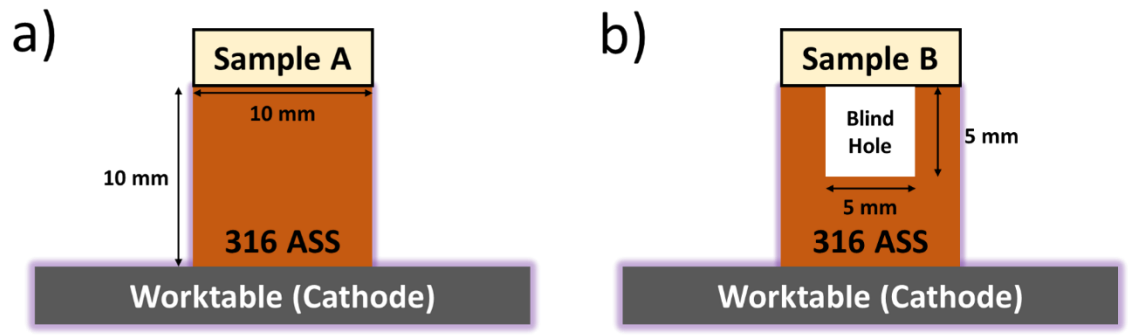

Figure 5-4. Schematic design and configuration of the DC plasma treatment with (a) normal and (b) blind hole contact conditions.

Furthermore, to investigate whether the black regions always grow from the bottom to the top of the material, or whether they grow from the cathode-facing surface towards the opposite-facing surface (denoted as anode-facing surface), a treatment configuration was employed where the contact point of the zirconia sample with the cathode was changed to be at the top surface (as shown in Figure 5-5).

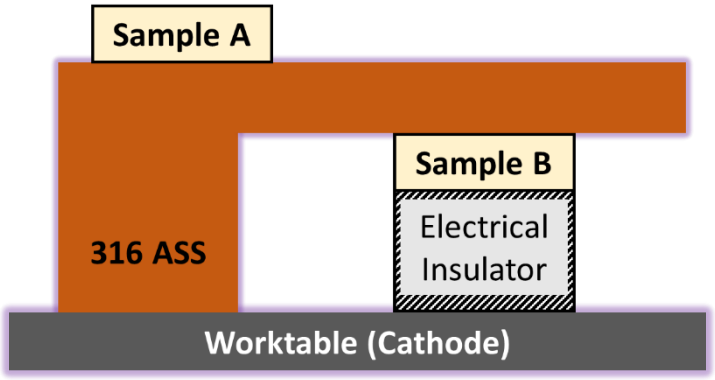

Figure 5-5. Schematic diagram of the plasma treatment configuration investigating the direction of growth. Sample A was placed with the bottom surface in contact with the cathode (AISI 316 austenitic stainless steel). Sample B was placed with the top surface in contact with the cathode.

5.2.3 Raman mapping

Raman scanning was conducted using a Renishaw inVia Raman microscope fitted with a 532 nm excitation laser source and groove density of 1800 l/mm. Raman reflectivity was employed to characterise the bulk modification of zirconia. The data was processed using Casa XPS for deconvolution of the spectra (into the 3 E_g and 1 A_{1g} modes of the tetragonal phase). The data was finally analysed by accumulating the area contributions of all 4 tetragonal phase peaks into intensity maps across the depth of the samples.

5.2.4 X-ray diffraction (XRD)

Crystallographic phase analysis was performed using a Proto AXRD benchtop X-ray diffractometer fitted with a Cu radiation source (Kα = 0.15406 nm). Measurements were performed between 2θ angles of 20 - 80 ° using a step increment of 0.01493 °.

5.3 Experimental results

5.3.1 Effect of the different plasma setups (DC and AS)

As described in Section 5.2.2, both DC plasma (DCP) and AS plasma (ASP) treatment configurations were employed to study the impact of direct cathodic potential on the plasma blackening of zirconia.

Figure 5-6 reveals that the white zirconia could only be completely transformed to black under the DCP-treatment whilst the ASP treated samples have no appreciable transformation in colour. Therefore, this confirms the need for direct power to the sample for the successful plasma blackening of zirconia (which will be further discussed in section 5.4).

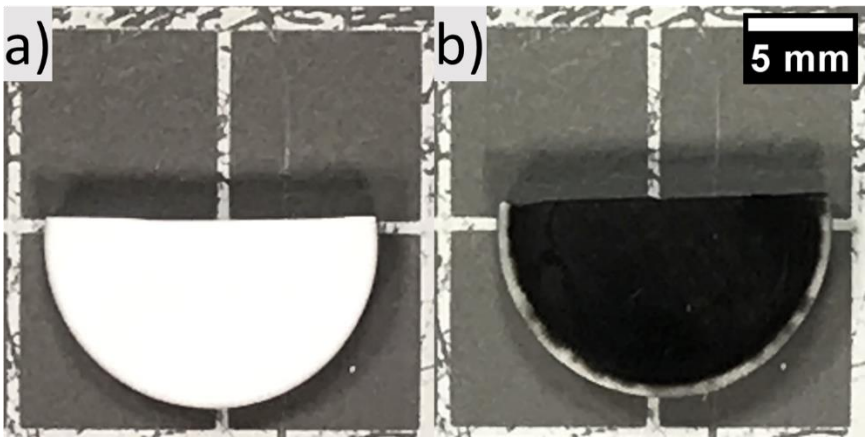

Figure 5-6. Surface images of (a) ASP-treated and (b) DCP-treated zirconia.

5.3.2 Effect of plasma treatment parameters

Given that only DCP treatments were able to modify the zirconia (Figure 5-6), all subsequent investigations were exclusively performed under DCP treatment conditions. The key parameters considered in these experiments were the treatment temperatures (100, 200, 300, and 500 °C), durations (30 and 300 minutes) and applied cathodic potential (370 – 450 V).

5.3.2.1 Temperature & Duration

Figure 5-7 reveals a positive correlation between the degree of plasma blackening for both treatment temperature and duration. As evidenced in Figure 5-7a1 and a2, there is no appreciable blackening when treatment was performed at 100 °C, even when the sample was treated for 5 hours. Colour transformation (blackening) was observed to initiate when the temperature was increased to 200 °C, appearing to grow from the bottom cathode-facing surface of the samples. Moreover, a significant increase in the depth of the black transformed region was found when the treatment duration was extended from 30 min to 5 hours (Figure 5-7b1 and b2).

A significant increase in the degree of blackening was observed when the treatment temperature was increase to 300 °C. Figure 5-7c1 and c2 clearly illustrate that the samples become almost entirely black, even when treated for only 30 minutes. The initially discrete black spots on the surface of the sample are found to merge, forming a continuous black surface. Internally, striations of lighter and darker regions are found to develop across the sample, forming columns that traverse from the bottom to the top of the sample. Additionally, the colour of the material close to the bottom (cathode-facing) surface is found to be darker than the top (anode-facing) surface, with a gradual change of colour, going from black to reddish-brown, within each column. At 500 °C, these colour variations are not as visible, with both surfaces presenting with a deep and uniform black colour (Figure 5-7d1 and d2). The only notable difference between the samples treated at 500 °C for 30 minutes and 5 hours is the transformation (blackening) of minor regions near the edges of the top surface.

Overall, these observations signify that the treatment temperature has a substantial effect on the feasibility and degree of plasma blackening of zirconia, while the

treatment duration appears to only have an accumulative effect on the degree of plasma-induced blackening.

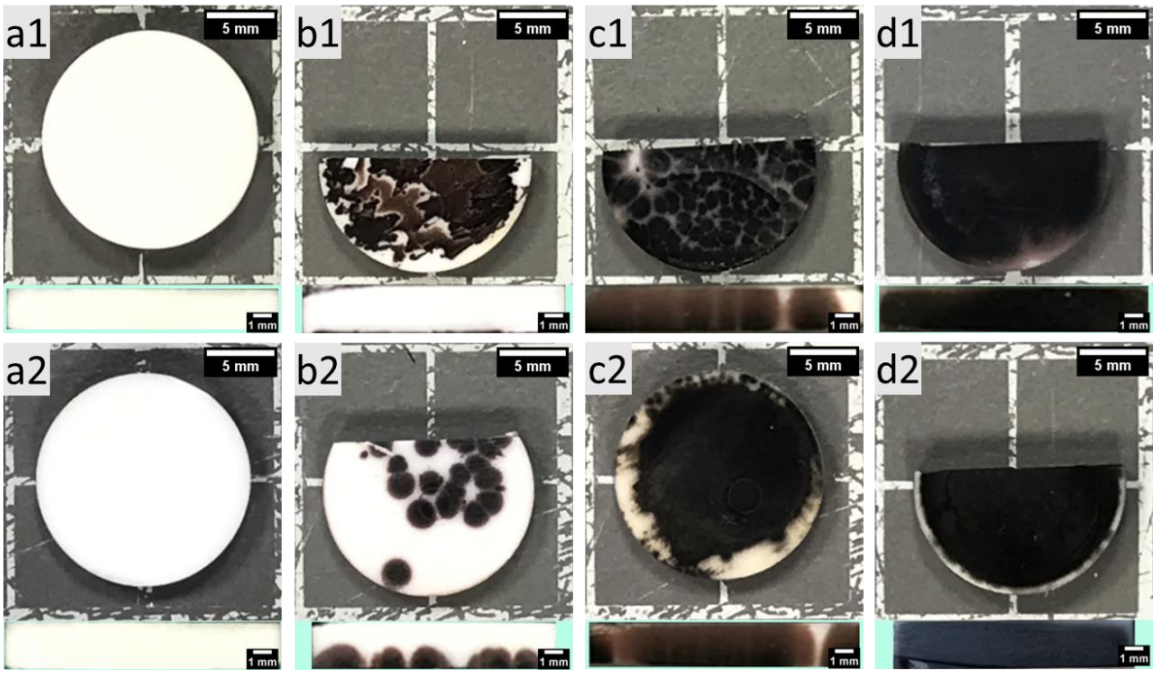

Figure 5-7. Optical images of zirconia samples DC plasma treated under different temperatures of (a) 100 °C, (b) 200 °C, (c) 300 °C, and (d) 500 °C. Treatment durations of (1) 30 minutes and (2) 5 hours are also shown for each temperature. A cross-section view of each treated sample is also present at the bottom of each image.

5.3.2.2 Effect of voltages

As no appreciable glow-discharge was observed within the plasma furnace at voltages below 370 V, the influence of cathodic potential was only examined at voltages greater than 370 V. Simultaneously, it was not possible to maintain a temperature of 200 °C with the application of potentials above 450 V (temperature increased above 200 °C even with just a single). Therefore, investigations on the influence of cathodic potential on the plasma blackening of zirconia were limited to voltages between 370 and 450 V.

As revealed within Figure 5-8, when all other parameters are controlled, the influence of increasing voltage is found to directly correlate with the number of circular black spots formed on the cathode-facing (bottom) surface of the zirconia sample. Given the varying sizes of the spots between and within each sample, only the largest (i.e., fastest growing) spots were used for comparisons between different voltage settings. No significant difference could be measured in the diameters of the largest black spot formed across the different voltage treatments, with an overall average diameter of 1.97 ± 0.06 mm. As the frequency of the formed spots increases with applied voltage, this implies that cathodic voltage plays an important role for initiating the transformation but does not appear to significantly impact the growth mechanism.

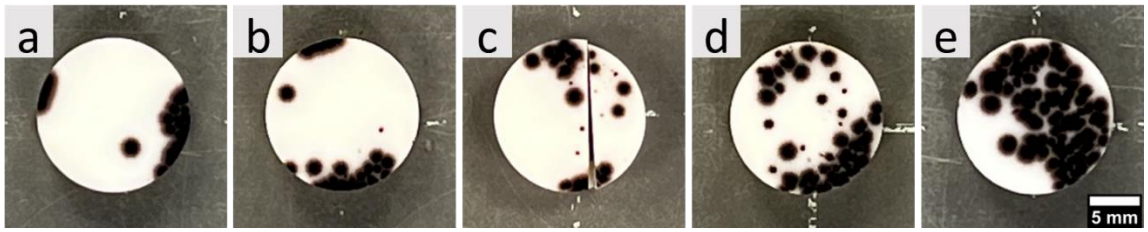

Figure 5-8. Optical images of zirconia samples DC plasma treated under different cathode potentials of (a) 370 V, (b) 390 V, (c) 410 V, (d) 430 V, and (e) 450 V.

5.3.3 The effect of plasma treatment settings

As the materials involved and configuration of the plasma furnace can also impact the outcome of the treatment, the following chapter aims to assess the potential role of cationic doping on the transformation of zirconia, the need for direct contact with the cathode for the initiation and growth of black regions, and the direction of growth of the black regions.

5.3.3.1 Cathode material

Cationic doping (e.g., with Fe) has previously been reported to be able to reduce zirconia, thereby transforming the material from white to black [132, 291-293]. Given that the steel cathode worktable used in this study contains elements which have potential to dope zirconia, it is important to investigate plasma treatments where cationic doping is not allowed (or significantly restricted). Since Zr702 is primarily composed of Zr (98.8 wt%), the potential role of cationic doping can be effectively avoided when carrying out plasma treatments using a Zr702 cathode worktable. As illustrated in Figure 5-9, both Zr702 and the AISI 316 stainless-steel cathode materials were able to produce black zirconia, which indicates that the principal mechanism for the plasma blackening of zirconia is independent of elemental doping.

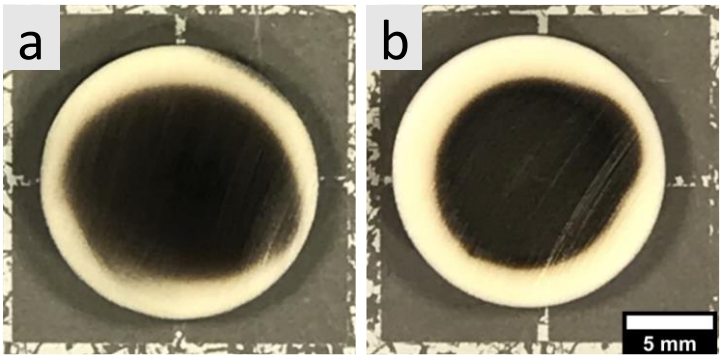

Figure 5-9. Optical images after DC plasma treatment at 500 °C for 5 hours using a (a) Zr702 and (b) AISI 316 stainless steel worktable.

5.3.3.2 Contact conditions

As the plasma blackening was observed to start at 200 °C (for both 30 minute and 5 hour treatments) but did not show complete through-depth treatment of the zirconia, it was chosen as the ideal temperature for examining the importance of contact conditions on the initiation of the blackening. As expected, both the normal and blind hole contact conditions showed that the black spots on the cathode-facing surface

(Figure 5-10) and the blackened regions of the cross-section (Figure 5-11) expanded with longer treatment durations.

Examination of the location and growth of the black spots on the cathode-facing surface of the treated samples demonstrated the importance of direct (or close) contact of the cathode with the sample. Where contact was not possible (i.e., in the blind hole regions), no black spots were found to form (Figure 5-10b1-b5). Instead, these areas were only found to begin transforming with longer durations (associated with the accumulation effect, as observed in section 3.2.1). On the other hand, under normal contact conditions (Figure 5-10a1-a5), both the edges and the centres of the cathode-facing surface were found to form the initial black spots.

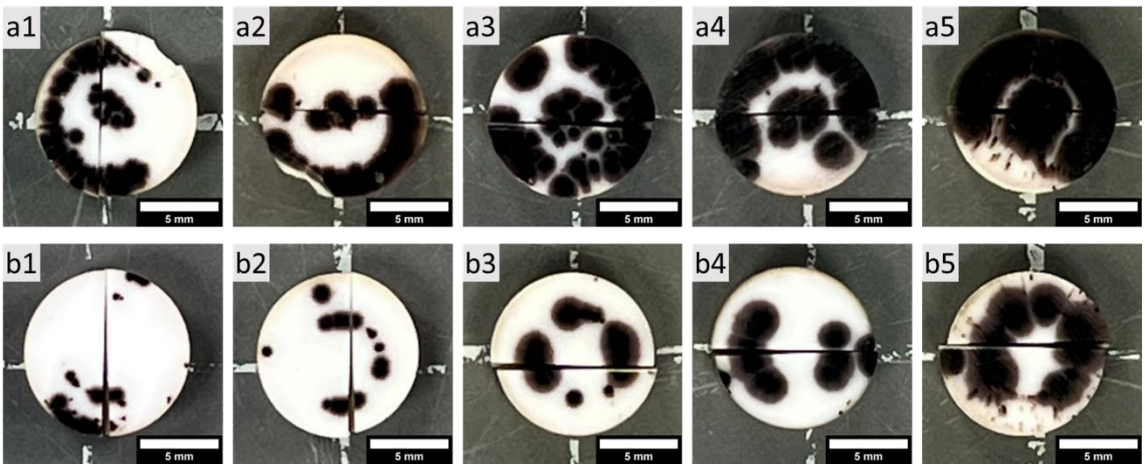

Figure 5-10. Plasma treated samples under (a) normal) and (b) blind hole contact conditions at 200 °C for: 1h (1), 2h (2), 3h (3), 4h (4), and 5h (5).

Interestingly, the transverse cuts of both treated samples clearly reveal incremental growth of the black regions towards the anode-facing surface (Figure 5-11). These initial black dots are found to expand at approximately equal rates in both the horizontal and vertical directionsly in the 2D cross-section views. Given the eventual expected through-depth treatment of the zirconia (Figure 5-6), this implies that the rate

of growth of the black spots is equal in all 3 dimensions (i.e., x, y and z), and therefore should be forms a hemispherical shape.

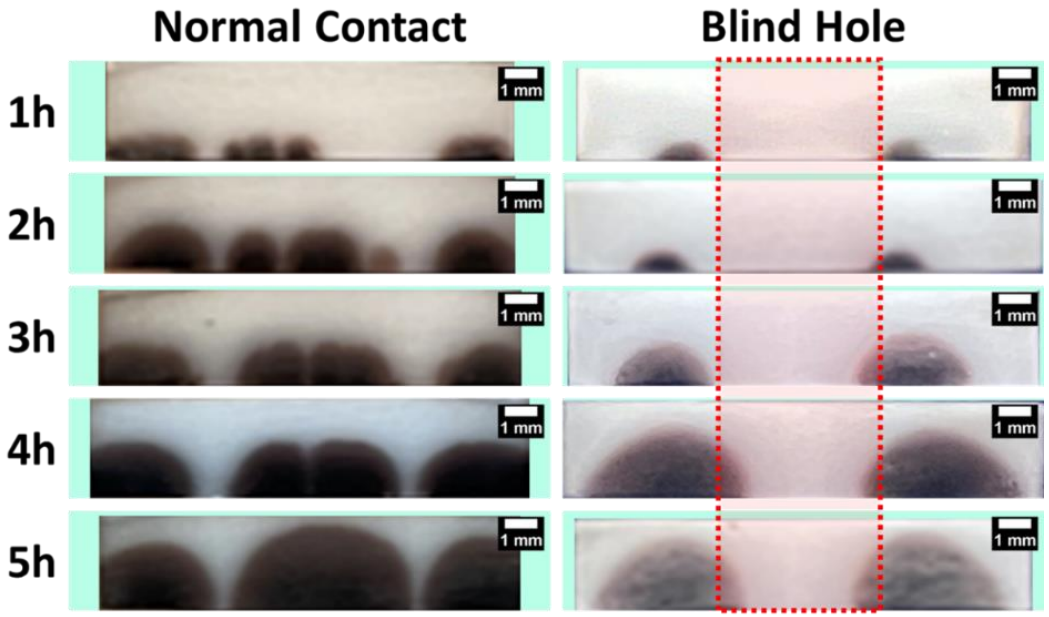

Figure 5-11. Cross-section views of plasma treated samples under normal (left) and blind hole (right) contact conditions at 200 °C for increasing durations (going down).

5.3.3.3 Plasma blackening growth direction

Studies utilising electrochemical reduction methods to form black oxygen-deficient zirconia have previously shown that the black regions grow from the cathode towards the anode [121, 122, 133, 294]. The similarities between electrochemical reduction techniques and our plasma approach (i.e., both involve the use of separated electrodes) suggest that a similar growth mechanism is to be expected. However, given that plasma treatments also involve ion bombardment of the exposed surfaces (i.e., surfaces not in contact with the cathode) and that the treatments are performed at low pressures, it is still necessary to confirm the direction of growth.

To evaluate the initiation and direction of growth of the black regions, treatments were carried out where the contact point between the cathode and the zirconia samples was reversed (Figure 5-5). One sample was maintained in an upright configuration (Sample A; bottom surface in contact with the cathode) while the contact point was flipped for the other sample (Sample B; top surface in contact with the cathode). To allow for the identification of the growth direction, the treatments were performed at a relatively low temperature of 200 °C to avoid the complete transformation of the material.

Figure 5-12 reveals that the initiation and growth of the black regions always develop from the surfaces in contact with the cathode (i.e., cathode-facing surface). Therefore, this suggests that plasma-induced blackening of zirconia follows the same cathode-to-anode growth direction as the electrochemical reduction methods. Moreover, these findings also support the contact condition requirements for the initiation and growth of the black regions (as previously introduced in section 4.3.2).

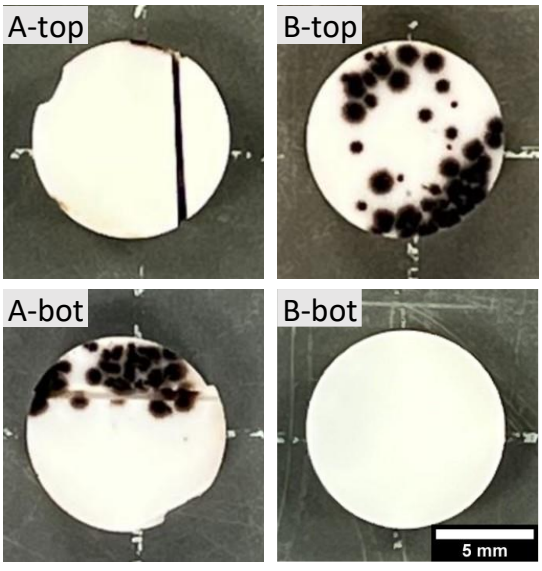

Figure 5-12. Optical images of the top and bottom surfaces of zirconia samples plasma treated at 200 °C for 30 min with the cathode in contact beneath the sample (A) and above the sample (B).

5.3.4 Accumulation and degree of blackening

As previously reported by the authors of this study [295], plasma treatments have the ability to significantly improve the broad spectrum light absorption capability of zirconia. Therefore, to map the light absorption capability across a plasma treated zirconia sample, tetragonal phase peak contributions in Raman spectra were systematically collected at different positions across sample. Colour maps were then used to visualise the light absorption capability (or degree of blackening) across the material.

The darkest regions in Figure 5-13b appear to correspond with the initial spots at the cathode-facing surface of the sample, which is consistent with the results from Section 3.3.2 and Section 3.3.3. The light absorption capability of each black region decreases when moving away from this starting central spot (in all directions). Although isolated black regions were previously observed to grow at the same rate in all directions over time (Figure 11), when they approach other black regions they appear to not completely follow this trend. This is clearly found within the highlighted right region of Figure 5-13, which shows that the growth of two nearby discrete black region is hindered at the sides facing each other, therefore suggesting some form of growth inhibition. Interestingly, this is not observed to significantly impact the maximum depth of the black regions, with all black regions appearing to have similar maximum depths.

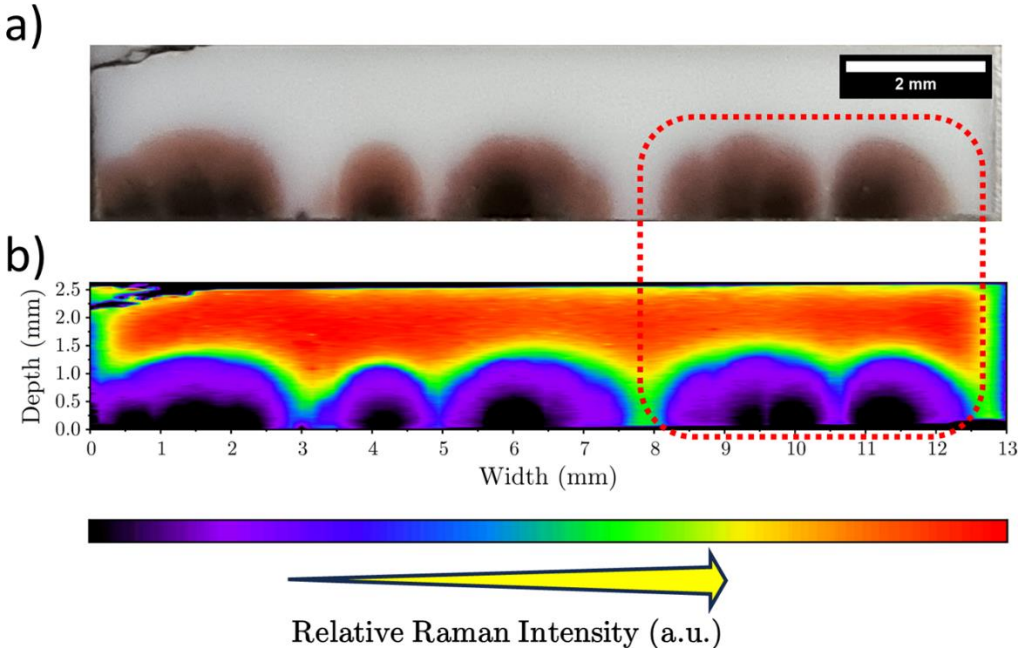

Figure 5-13. Cross-sectional (a) optical image and (b) Raman intensity map of a zirconia sample plasma treated at 200 °C for 5 hours.

5.4 Discussion

To devise the potential transformation mechanism involved during the plasma blackening of zirconia, an evaluation of the influence that different treatment configurations and parameters have on the initiation and growth of black zirconia has been conducted. Given the vast number of parameters, the following discussion has been grouped to overview (1) the role that pre-existing oxygen vacancies have at the start of the plasma treatment, (2) the importance of cathodic contact and electrical discharge on the blackening of zirconia, (3) potential mechanisms for the conductance of oxygen anions within the lattice and the generation of new oxygen vacancies, and (4) the formation of a moving cathode front within the zirconia (and the potential implications). Finally, (5) the plasma reduction of zirconia is compared with traditional electrochemical reduction methods.

5.4.1 The role of pre-existing oxygen vacancies

Yttria-stabilised zirconia (YSZ) is known to contain oxygen vacancies ($V_O^{\cdot\cdot}$) within the material as illustrated in Figure 5-14a, which must form in response to the charge disparity between Zr^{4+} and Y^{3+} (as depicted by equation 5-1) [120, 296-298]. This development of oxygen vacancies (with no trapped electrons) acts to preserve charge neutrality across the entire material. However, despite the net neutral charge from a macroscopic scale, the presence of oxygen vacancies with less than two trapped electrons (i.e., $V_O^{\cdot\cdot}$ and $V_O^{\cdot}$) do still create localised charge disparity across the anionic sites (as these vacancies are positively charged in relation to anionic sites occupied by O^{2-} ions) [120, 299, 300].

Therefore, in the presence of a cathodic and/or anodic potential (as found during plasma treatments), this local charge disparity can be expected to lead to the

segregation of charges according to their relative potential (i.e., $V_O^{\cdot\cdot}$ moving towards the cathodic side and O^{2-} sites moving towards the anodic side). If the cathodic and anodic potentials are homogeneously spread across opposite faces of the material (as would be the case under ideal contact conditions), a uniform gradient of oxygen vacancies would be expected to be developed at each depth between the two electrodes (Figure 5-14b). As the movement of oxygen vacancies can only be possible through the displacement of lattice oxygen atoms, an equivalent amount of lattice oxygen is considered to move in the opposite direction (i.e., from the cathode towards the anode) as illustrated in Figure 5-14c. As shown by equation 5-2, this represents a net movement (from anode-facing sites) of oxygen vacancies towards the cathode-facing surfaces $[V_O^{\cdot\cdot}(\text{af}) \rightarrow V_O^{\cdot\cdot}(\text{cf})]$ with a net movement of lattice oxygen (from cathode-facing sites) towards the anode-facing surface $[O_O^X\ (\text{cf}) \rightarrow O_O^X\ (\text{af})]$.

$$Y_2O_3 \rightarrow 2Y_{Zr}' + 3O_O^X + V_O^{\cdot\cdot} \quad (5\text{-}1)$$

$$V_O^{\cdot\cdot}(\text{af}) + O_O^X\ (\text{cf}) \rightarrow V_O^{\cdot\cdot}(\text{cf}) + O_O^X(\text{af}) \quad (5\text{-}2)$$

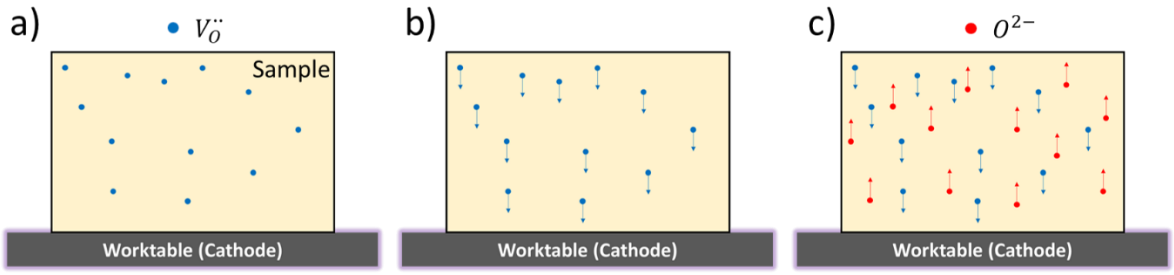

Figure 5-14. Schematic diagram showing a transverse view of a zirconia sample on a cathode worktable with (a) the pre-existing oxygen vacancies, (b) the initial movement of pre-existing oxygen vacancies and (c) the opposite migration of lattice oxygen.

5.4.2 The need for cathode contact and electrical discharge

Instead of a homogeneous reduction of the zirconia following plasma treatment, localised circular black spots are observed on the surface of the samples (Figure 5-7 and Figure 5-8). Given that ideal flat contact between two plane surfaces (i.e., sample and worktable) is known to be extremely challenging, this suggests that ideal contact conditions are not present during these treatments. Therefore, it is more probable that the true physical contacting points between the surfaces are localised to the most protruding asperities of the two surfaces (Figure 5-15a & b). This suggests that the diffusion of the oxygen vacancies towards the cathode is not uniform and is instead biased towards the sites with the strongest cathodic potential (i.e., most intimate contacting points). Confirmation of this directional migration was revealed by developing a treatment with only a single contact point with the cathodic worktable (Figure 5-15c & d). Plasma blackening was observed to only develop from the single contact point (and grew uniformly in all directions away from the contact point).

The contact dependence of the process is further supported by the findings of the treatments utilising worktables with blind holes (Figure 5-10). No circular black spots could be found at sites where contact between the cathode and zirconia sample was intentionally prevented.

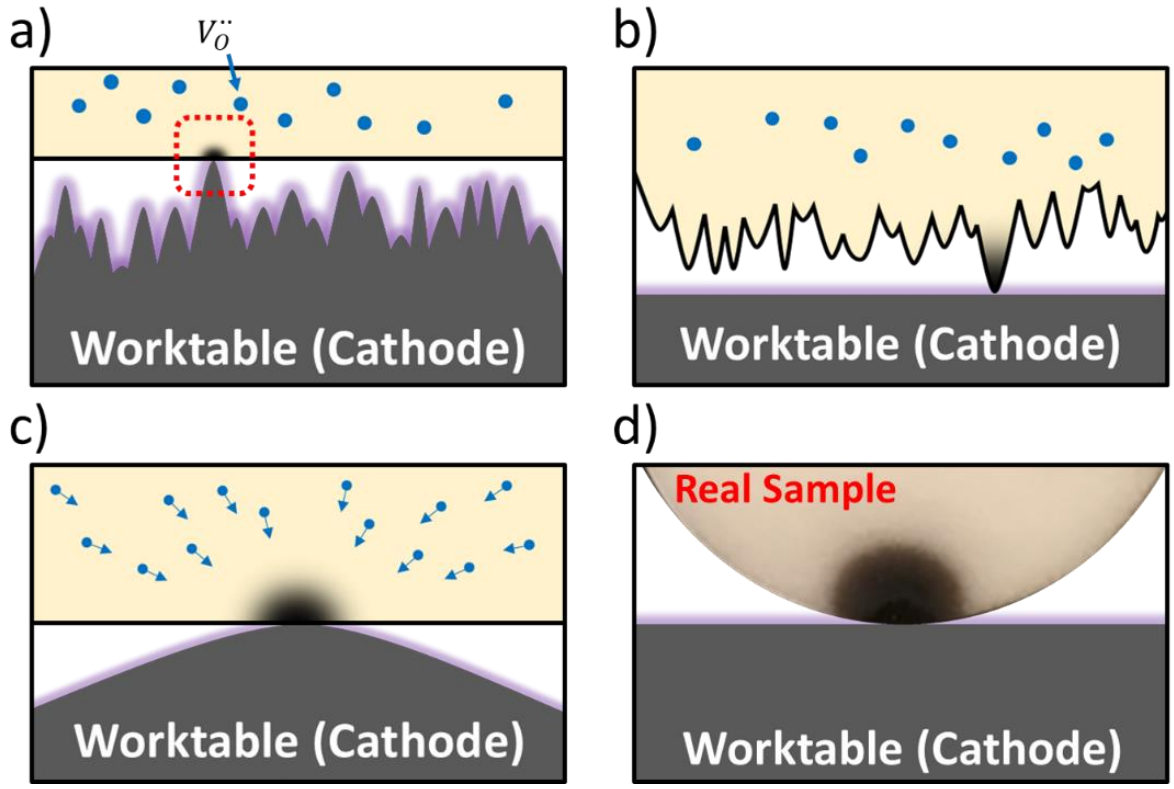

Figure 5-15. Diagram showing a transverse view of a zirconia specimen with pre-existing oxygen vacancies ($V_O^{\cdot\cdot}$) under different contact conditions due to a rough worktable surface (a) or rough sample surface (b). A magnified view of a single asperity with the collective directional movement of oxygen vacancies towards the contact point (c). A camera image of a cylindrical zirconia sample treated using a single contact point under DCP plasma treatment conditions at 200 °C for 5 hours (d).

The influence of voltage is well described by Paschen's law, where the breakdown voltage of a gas (or gas mixture) is a function of the pressure and distance between the electrodes [301, 302]. Given that the zirconia is typically non-conductive, it can be regarded as being at a floating potential that is relatively anodic to the worktable (to oppose the nearby electric fields). At close distances (or appropriate power/pressure settings), it is possible for the electric current to discharge from the cathode towards the zirconia. In practice, the discharge of current will closely relate to the gap between the asperities of the zirconia and the cathodic worktable, with greater breakdown

voltage requirements for larger gaps. At sufficiently low potentials, this would give rise to only the most intimate contacting asperities being actively involved in the discharge process. Therefore, this localises the positions where significant current transfer can take place and consequently influences the electric field distribution around the sample and the non-uniform net movement of oxygen vacancies (and cation reduction) across the cathode-facing surface.

The combined findings of the blind hole (Section 5.3.3.2) and cathodic potential (Section 5.3.2.2) experiments demonstrate the critical influence of contact conditions and electrical potential on the initiation mechanism and localised bulk-reduction of zirconia. The importance of the ‘active’ black spots at the cathode-facing surface is also clearly demonstrated by the lack of transformation of the zirconia under ASP treatment conditions (Figure 5-6), where no direct contact with the cathode is made despite interactions with other reactive species within the plasma.

Figure 5-16 provides an overview of the relationship between the local cathode-to-sample spacing and applied potential, as well as their influence on the net movement of oxygen vacancies. Larger cathodic potentials are shown to allow for the breakdown of bigger gaps between the asperities of the cathode worktable and zirconia surface. This allows for the ‘activation’ of non-contacting asperities (indirect contact) and allows for the development of more ‘active’ sites (from Figure 5-16b). The influences of nearby ‘active’ sites on each other are also illustrate in Figure 5-16c, and will be discussed in further detail in Section 5.4.4

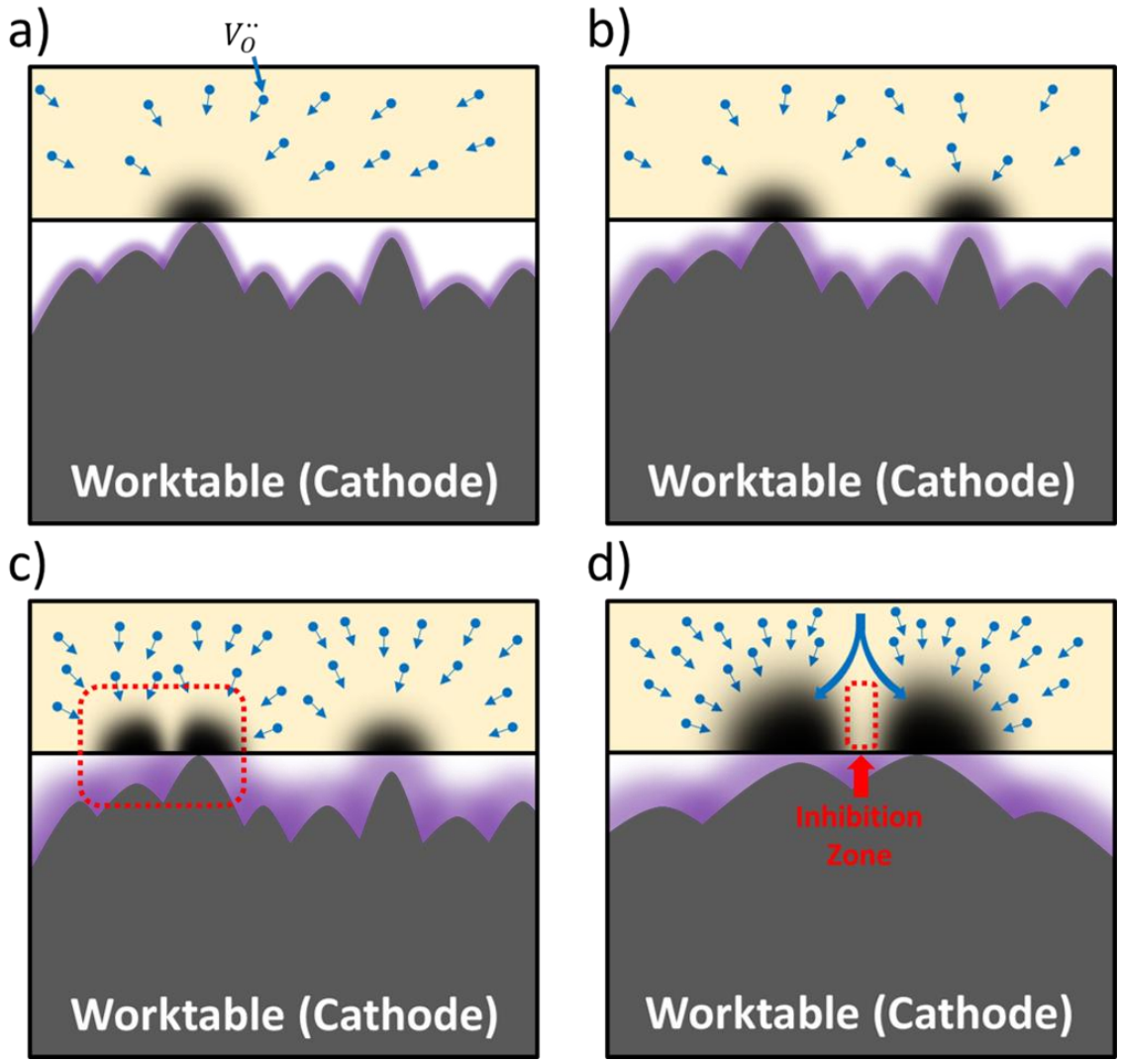

Figure 5-16. Overview of the localised 'activation' of the cathode-facing surface, directed net movement of oxygen vacancies ($V_O^{\cdot\cdot}$) and the influence of nearby black regions during the initial stages of plasma treatment of zirconia. Images a) → c) show the effect of increasing cathodic potential and demonstrate the electrical breakdown of larger gaps and therefore the 'activation' of more sites on the zirconia surface. When 'active' sites are well separated (a & b), the black regions are found to grow with a hemispherical shape. However, when 'active' sites are close together (c) black regions with asymmetrical shape develop. Image d) shows a magnified view of two nearby 'active' regions. The diversion of the net movement of oxygen vacancies between the two 'active' regions is revealed, and demonstrates how the inhibition zone between them forms.

5.4.3 Generation and conduction of new oxygen vacancies

Although oxygen vacancies exist within pristine yttria-stabilised zirconia, the total numbers are finite and cannot account for the progressive collection of vacancies at the cathode-facing ‘active’ regions. However, as progressive transformation of zirconia is observed with longer and/or more powerful plasma treatment conditions, it must be implied that new oxygen vacancies are generated within the treatments. The hemispherical outward growth of the black regions is also supported by the formation of new oxygen vacancies (from the anode-facing surfaces), which can enable continuous homogeneous net movement of oxygen vacancies from all directions. Therefore, this suggests that the environment around the anode-facing surfaces may also play a crucial role in the extensive treatment of zirconia.

The bombardment of electrically conductive workpieces with ionised gases forms the foundation of many direct current (DC) plasma treatments. However, as untreated zirconia is not a good electrical conductor, no such direct bombardment would be expected to occur. Additionally, as the zirconia is not in direct contact with the anode, as is the case in electrochemical reduction methods, the driving forces for the removal of oxygen are difficult to explain. Therefore, alternative means of forming oxygen vacancies must exist. One potential way is the interaction of the exposed anode-facing surfaces with post-plasma species within the chamber. Given that species within the plasma are highly energetic (i.e., at high temperatures), even when the collective plasma can be considered ‘cold’ or ‘weak’, it is possible for these species to overcome the Zr-O dissociation energy and thus allow for the formation of oxygen vacancies (equation 5-3).

Once the oxygen vacancies are formed, their relatively positive charge leads to their accumulation at the 'active' sites of the cathode-facing (cf) surface (as described in Section 5.4.1). The combination of the net movement of oxygen vacancies away from the anode-facing surfaces and their replacement with lattice oxygen (equation 5-2 and Figure 5-17 allows for the continuous generation of new oxygen vacancies throughout the plasma treatment. The cathodic potential of the worktable can then attract the (relatively) positively charged oxygen vacancies towards the 'active' sites, as well as supply the electrons necessary for the reduction of zirconium ions (Zr^{4+} to Zr^{3+}). However, the order of these processes is still unclear and requires further investigation. Moreover, the role that the electrons formed during the generation of oxygen vacancies (equation 5-3) play is also unclear. It is possible for the electrons to be released away from the sample (and move towards the chamber anode) or for them to facilitate the reduction of zirconium ions at the anode-facing surfaces (as shown by equation 5-4) [295, 303-305].

Overall, this proposed mechanism of oxygen vacancies generation is supported by the observed effects of temperature, cathodic voltage and treatment duration have on transformation of zirconia.

$$O_O^X \text{ (af)} \xrightarrow{\text{Plasma Interaction}} V_O^{\cdot\cdot}\text{(af)} + \frac{1}{2}O_{2(g)} + 2e^- \quad \text{(5-3)}$$

$$Zr^{4+} + e^- \rightarrow Zr^{3+} \quad \text{(5-4)}$$

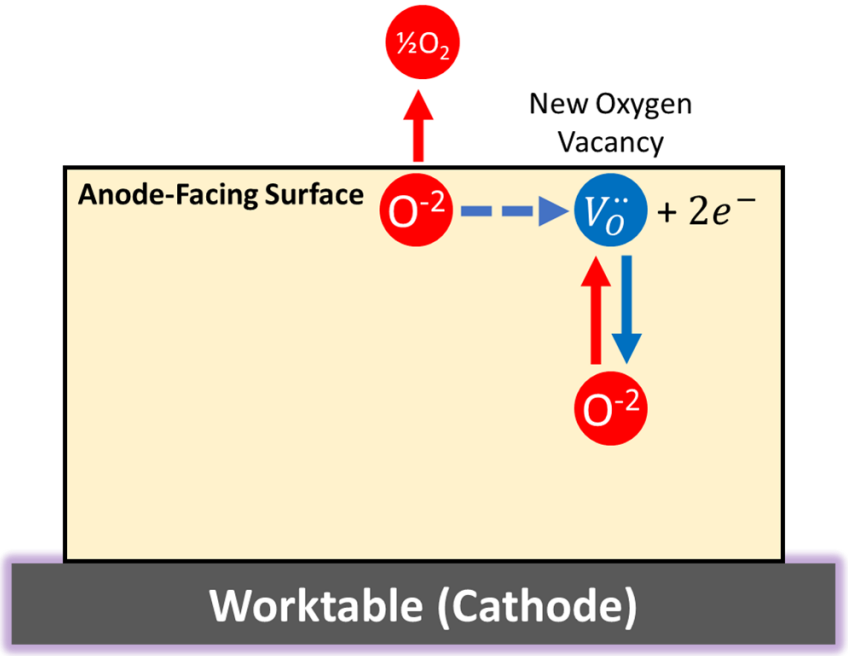

Figure 5-17. Overview of the continuous removal of lattice oxygen (O^{2-}) at the anode-facing surfaces during plasma treatment of zirconia. This is made possible by the replacement of newly formed oxygen vacancies (V_O^X) with lattice oxygen coming from cathode-facing sites.

5.4.4 Influence of treatment parameters on formation and net movement of oxygen vacancies

Treatment temperature is known to directly influence the energy requirements for the dissociation of Zr-O bonds (by way of increased bond thermal energy). [209, 306, 307] Therefore, higher temperatures can facilitate the rightward shift of equation 5-3, which, at the earlier stages of treatment, can be perceived as a shorter “initiation" phase (where limited or no colour change is observed). As the temperature rises, greater numbers of oxygen vacancies are generated, which increase the concentration of charge carriers, and thus increase the electrical conductivity of zirconia. The increased thermal (vibrational) energy within the zirconia crystal structure at elevated treatment temperatures also provides favourable thermodynamic and kinetic conditions necessary for diffusion (conduction) of oxygen vacancies (rightward shift of equation

5-2). This can accelerate the accumulation of oxygen vacancies at the cathode-facing surface, which can be interpreted as the "migration" phase. Hence, temperature strongly correlates with the rate of transformation under plasma treatment, as evidenced by the increasing bulk transformations shown in Figure 5-7.

Additionally, as greater power input (i.e., stronger plasma) is also required to achieve higher temperatures, the influence of plasma power must also be considered. As previously described in Section 5.4.2, the cathode potential can directly influence the number of ‘active’ sites that form on the cathode-facing surface. Therefore, it is already expected that increasing the operating voltage will directly influence the distribution and rate of bulk-reduction. Additionally, more energetic (and frequent) post-plasma species formed with stronger plasma will also aid in the generation of more oxygen vacancies. Finally, larger potential differences between the cathode, sample (floating potential) and anode walls of the chamber will also have an accelerating effect on the diffusion of oxygen vacancies towards the cathode. Overall, the effect of greater potential differences is to promote faster and more effective bulk-transformation of zirconia samples (as evidenced in Figure 5-8).

In contrast to temperature and operating voltage, treatment duration only appears to influence the extent of migration and accumulation of oxygen vacancies at the cathode-facing surface. Treatment duration is found to have no appreciable influence on initiating the transformation of the zirconia, as evidenced by the lack of change observed when insufficient temperature (or power) conditions are employed (Figure 5-7 & Figure 5-8). Similarly, cationic doping is also not observed to be (at least not significantly) involved in the formation and movement of oxygen vacancies during plasma treatment of zirconia (Figure 5-9).

5.4.5 Movement and growth of cathode front

At the start of the plasma treatment of zirconia, the current transfer (both direct and indirect) takes place at the physical interface between the cathode and the cathode-facing surface of the zirconia sample (as shown in Figure 5-16). However, analogous to electrochemical reduction techniques, this cathode front is found to move with the growth of the black oxygen-deficient zirconia ($ZrO_{2-\alpha}$) that initiates from the 'active' points at the cathode-facing surface.

This moving cathode front develops from the progressive migration of oxygen vacancies (and Zr^{3+} cations) from all directions towards these 'active' sites, which form a concentration gradient of oxygen vacancies. This leads to growing black regions that are progressively more oxygen-deficient over time (where α continuous becomes larger). The centre of the region exhibits the best light absorption and darkest colour (i.e., where α is largest), and the areas away from this centre gradually become lighter (i.e., where α becomes smaller). This gradient of oxygen-deficiency is strongly supported by the observations (Figure 5-13) of varying colour intensity (visually) and light absorption capability (under Raman mapping) of growing black regions.

As it is well established, the electrical conductivity of substoichiometric zirconia is significantly greater than stoichiometric zirconia [10, 13, 308]. As shown by equation 5, the overall formation of substoichiometric zirconia ($ZrO_{2-\alpha}$) follows from the removal of (molar equivalent amount of) lattice oxygen anions.

$$ZrO_2 \rightarrow ZrO_{2-\alpha} + \frac{\alpha}{2} O_{2(\mathrm{g;\,mol})} \quad (5\text{-}5)$$

This formation of oxygen-deficient zirconia also reduces zirconium cations ($Zr^{4+} \rightarrow Zr^{3+}$) and therefore gives rise to the occupation of new defect or mid-gap energy states (occupation of Zr 4d level) between the top of the valence band (highest occupied

energy level) and the bottom of the conduction band (lowest unoccupied energy level). Consequently, the electronic bandgap of oxygen-deficient zirconia is significantly reduced as compared with the pristine structure.

This lowers the energy requirement for the valence-to-conduction band transition of electrons, which significantly enhances the light absorption capability (bandgap within the visible light range) and improves the electrical conductivity of zirconia [8, 13, 14, 117].

Additionally, as this accumulation initiates and grows outward from the ‘active’ sites of the cathode-facing surface, this allows for the continuous occupation of the conduction band energy levels within these regions. The effect of this electron occupation is the propagation of the electrical current from the cathode interface to the reduced regions of the zirconia (black regions).

Effectively, this acts to extend the cathode front into the zirconia material, and as new oxygen vacancies are continuously generated and conducted towards the reduced regions, the transformed regions grow outward and become more conductive. Essentially, this forms a moving cathode front that is analogous to the moving reaction front in electrochemical reduction techniques [133].

The hemispherically growing black regions form a dynamic cathode front which increases the effective surface area of zirconia in contact with the cathode. Consequently, this mechanism regulates the lateral surface growth of the black regions at a rate consistent with that of the internal boundaries (as found within Figure 5-11).

The observations of the growth trends of the black reduced regions provides strong supporting evidence for the moving cathode theory. During the early stage of growth,

the black regions are typically small enough and spread out enough to not influence each other, giving rise to hemispherical growth within the material (Figure 5-16a). The hemispherical growth proceeds while the different black regions are separated (Figure 5-16b). However, as the black regions approach one another, the supply of oxygen vacancies for each growing black region becomes divided. This significantly limits the growth rate of the regions between the adjacent moving fronts and results in the formation of columnar morphology between the regions (as shown by Figure 5-16d). When there are many adjacent black regions, columnar shaped growth patterns are seen throughout the bulk (as shown in Figure 5-7c1).

When the moving reaction front reaches the anode-facing surface of the sample, a direct circuit can form between the cathode, sample, and anode (going through the conductive gas atmosphere). This accelerates the transformation rate at the through-depth treated regions by enabling direct ionic bombardment of the exposed spots (as shown in Figure 5-18). The formation of the plasma at the surface brings both greater quantities and more energetic impact events, thereby increasing the rate of removal of lattice oxygen and supply of fresh oxygen vacancies at the surface (equation 5-3). The development of this bombardment has already been shown by the authors in a previous study (Fig.1 of [12])

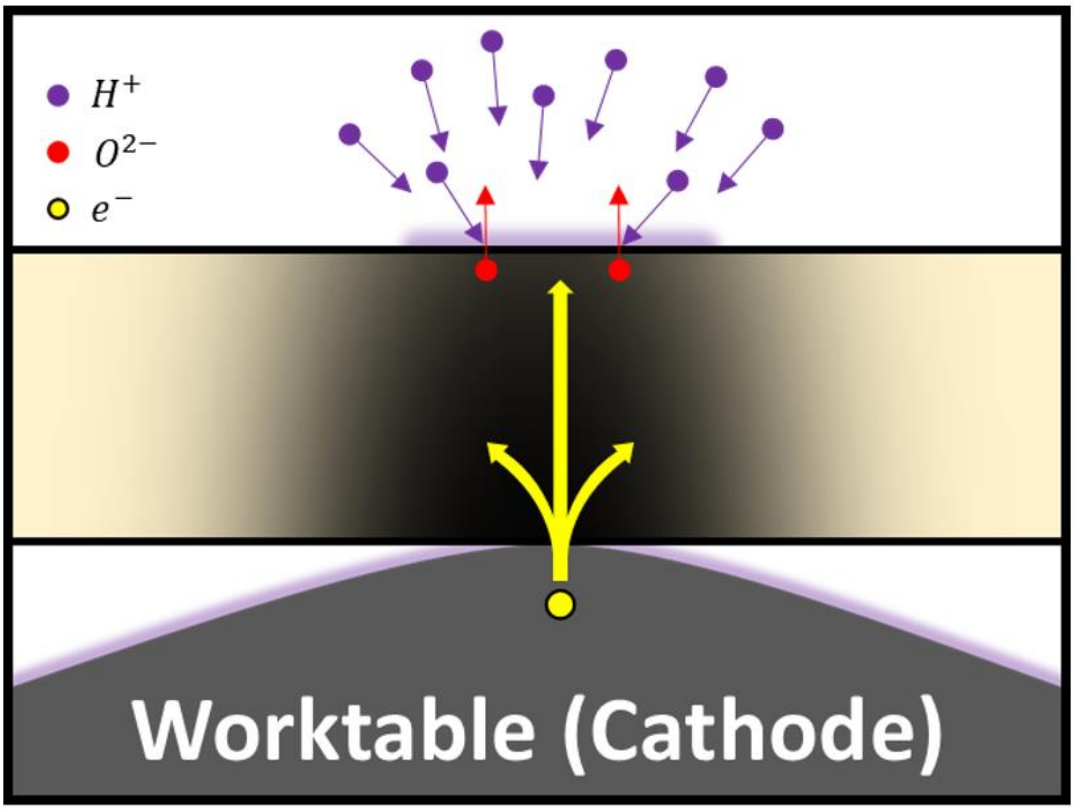

Figure 5-18. Schematic representation of the formation of a glow-discharge at the anode-facing surface of zirconia following the through-depth growth of the black regions. The subsequent direct bombardment with ionic species (H^+ in this case) accelerates the removal of lattice oxygen and the formation of oxygen vacancies during the plasma treatment.

5.4.6 Difference of plasma reduction and electrochemical reduction

From the first reports of electrical blackening of zirconia in 1970 [300], investigations on the blackening phenomena have attracted substantial interest [276, 309-320]. As investigations into the electrochemical, optical, and thermal modifications of black zirconia have advanced, numerous studies have successfully demonstrated the brightening and darkening transformation of zirconia during flash sintering. Given the similarities between flash sintering and plasma blackening (as previously described in [295]), it is valuable to compare the mechanisms and principals involved across both technologies [121, 122, 133].

The primary distinction between plasma treatment and traditional electro-reduction methods lies in the setup and operational principles. Under plasma treatment, the sample does not come into direct contact with the anode of the circuit. Instead, ionised gases play a crucial role in the process by providing a conductive medium for the transfer of current between the anode and cathode (i.e., completing the circuit) [12, 186, 321-323]. This significantly accelerates the subsequent reduction process through two ways: (1) greater effective surface area in (indirect) contact with the anode for the formation of oxygen vacancies (leading to spherical growth) and (2) strong direct plasma bombardment once the transformed regions expand to the outer surface (as shown by the accelerated bombardment with H^+ ions in Figure 5-18).

As the bottom of the sample is in contact with the cathode, it is subjected to the strongest cathodic potential, while all other surfaces of the zirconia sample can be regarded as being relatively anodic in comparison. This arrangement allows oxygen to escape from various angles, as evidenced by the observed hemispherical shape and growth of the black regions in Figure 5-10 and Figure 5-13.

Unlike plasma treatments, electrochemical reduction typically gives rise to parallel field lines between the electrodes [324]. This typically then generates a unidirectional potential gradient and produces a unidirectional flow of current between the anode and cathode with the sample [133]. Therefore, this constrains the direction in which oxygen can escape, and new vacancies can be supplied for the continuous reduction, which leads to the formation of distinct finger-like growth of black regions [133].

Based on the principles of electrochemistry, the entire zirconia samples can be understood as a collection of resistors connected in parallel in the direction of the current. Consequently, the central regions (core) of the cathode-touching zirconia

surfaces in electrochemical reduction approaches are more likely to overcome the breakdown voltage (as discussed in Section 5.4.2), leading to preferential reduction around those regions. However, no such phenomena is observed for plasma treated zirconia samples, with the depth of the black regions being found to be consistent between the edges and centres of the samples (Figure 5-7b2 and Figure 5-10). Therefore, low-pressure plasma treatment presents as a flexible and spatially unrestricted technique for the reduction of zirconia.

5.5 Conclusions

Bulk oxygen-deficient zirconia was successfully produced within this study using a variety of low-pressure plasma treatment configurations and parameters. Evaluation of the impact of different treatment parameters on the reduction (blackening) of zirconia has enabled the proposal of a potential mechanism for the initiation and growth of the transformed regions. Four key development stages of the transformation process are identified, namely: bulk oxygen vacancy conductance, surface activation, oxygen vacancy generation and a moving cathode front. The findings of this study are summarised as follows:

- **Bulk oxygen vacancy conductance:** The reduction (blackening) of zirconia arises due to the opposing net migrations of lattice oxygen (O^{2-}) and oxygen vacancies ($V_O^{\cdot\cdot}$) towards the anode-facing and cathode-facing surfaces, respectively.
- **Surface activation**: Transformation of zirconia is found to initiate at isolated 'active' sites that correspond to locations where there is direct contact (physically touching) or indirect contact (through the electrical breakdown of the gap) with the cathodic worktable.
- Newly formed black regions grow from the cathode-facing sites towards the anode-facing surfaces. When the 'active' sites are spread out, they grow in all directions and form hemispherical black regions.
- The change in colour of the treated material relates to the formation of oxygen-deficient zirconia ($ZrO_{2-\alpha}$). The strongest concentration of $V_O^{\cdot\cdot}$ (where α is largest) are found at the centre of the black regions (at the initiation site). When moving away from the centre, there is a gradual transition back to the white colour of the pristine material (corresponding to smaller α values).

- When the initial ‘active’ sites are located close together, migration of lattice oxygen and $V_O^{\cdot\cdot}$ becomes divided between the growing interfaces of both regions, leading to the formation of inhibition zones and asymmetric growth. This is found to initially produce striated columnar regions of black and white zirconia in through-depth treated samples, which disappear with longer and/or more powerful treatments.
- **Oxygen vacancy generation**: New $V_O^{\cdot\cdot}$ are generated by the release of lattice oxygen at the anode-facing surfaces. The opposing migration of $V_O^{\cdot\cdot}$ and lattice oxygen enable continuous generation of $V_O^{\cdot\cdot}$ throughout the treatment process.
- **Moving cathode front**: The cathode reaction front, which starts at the worktable surface, expands to the growing boundaries of the black regions throughout the treatment. This increases the effective surface area of the cathode in contact with the zirconia, and forms a moving cathode front, thereby accelerating the treatment process. Oxygen vacancies, which have a positive charge relative to lattice oxygen, migrate towards this moving cathode front.
- Once the moving cathode front reach the anode-facing surface, direct ionic bombardment of the surface ensues. This significantly enhances the rate of lattice oxygen removal and oxygen vacancies formation.

In conclusion, low-pressure plasma has been demonstrated to be an attractive and scalable alternative approach for the effective bulk-reduction of zirconia. The process is shown to be adaptable and highly controllable through the optimisation of treatment configurations and parameters. It is hoped that the promising findings of this study can inspire further studies on the plasma reduction of zirconia.

5.6 Supplementary material

In addition to the key information as reported in Paper II, some unpublished information is provided here as supplementary materials for Chapter 5.

5.6.1 X-ray diffraction (XRD) analysis from different temperatures

X-ray diffraction (XRD) analysis was conducted on the 30 min DCP-treated samples for various temperatures (100 to 500 °C). The obtained XRD patterns exhibited high conformity with the PDF standard card #48-0024 for 3-YSZ, as depicted in Figure 5-19.

Although the complete coverage of peak areas of the PDF card was not achieved, no unidentified peaks were observed or measured, suggesting that any missing regions can be attributed to variations in stoichiometry (as is typical in 3-YSZ samples). The X-ray diffraction (XRD) analysis revealed no significant changes in the 2θ angle, which represents the interplanar spacing (d-spacing), or in the broadening of the peaks, indicating no obvious changes in the long-range periodicity of the crystallography. However, a slight rightward shift of approximately 0.1-0.5 ° (as indicated by the orange dashed line in Figure 5-19) was observed in the characteristic peaks around 30, 35, 50 and 60 °. The degree of shift was found to correspond with the degree of sample blackening.

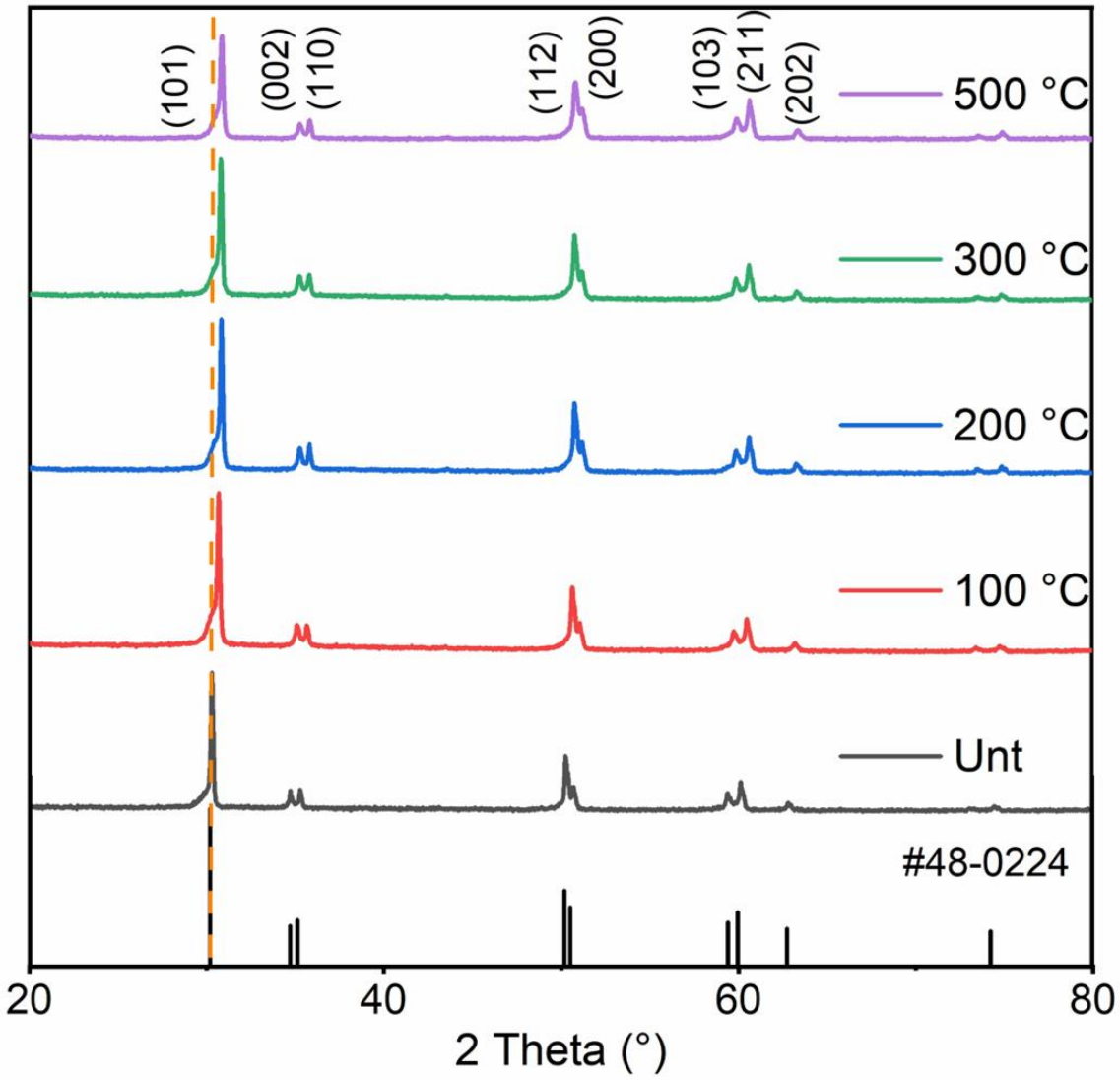

Figure 5-19. XRD patterns of the zirconia samples treated under different temperatures.

Reducing zirconia decreases the average ionic radius of the cation (i.e., zirconium), causing a contraction of the unit cell and a decrease in the unit cell parameter (as mentioned in section 2.3.2.1). Furthermore, the formation of oxygen vacancies can induce changes in the material's electronic structure, affecting the bonding and interatomic forces. These changes further contribute to generating residual stress and the contraction of the unit cell. Notably, the decreasing shift as the angle increases may be attributed to the specific crystallographic orientation of the material. The observed variations in the peak shifts between different crystal planes provide insights

into the lattice distortion during the treatment. Specifically, when examining the (101) crystal plane, the untreated sample exhibits a larger deviation of roughly 0.57° compared to the sample treated at 500 °C. This suggests that the (111) plane experiences a more pronounced lattice distortion during the plasma treatment. On the other hand, the average deviation for the two (202) crystal planes is only 0.50°, indicating a relatively more minor lattice distortion for these planes as shown in Figure 5-20.

These imply that different crystal planes and orientations may experience different lattice strain levels and ionic radii changes, resulting in varying magnitudes of peak shifts. The differences in peak shifts between crystal planes can be attributed to their unique crystallographic orientations and the arrangement of atoms within these planes. Each crystal plane has its own set of lattice parameters and arrangement of atoms, leading to varying degrees of susceptibility to lattice distortion. The response of each plane to the reduction process and the generation of oxygen vacancies can vary based on the interatomic forces and bonding characteristics specific to that plane. The variation in peak shifts also highlights the importance of crystallographic orientation when analysing the effects of plasma treatment on the zirconia material. Different crystal planes may exhibit different degrees of lattice distortion and changes in interatomic distances, providing valuable information about the underlying mechanisms and structural modifications occurring during the reduction process.

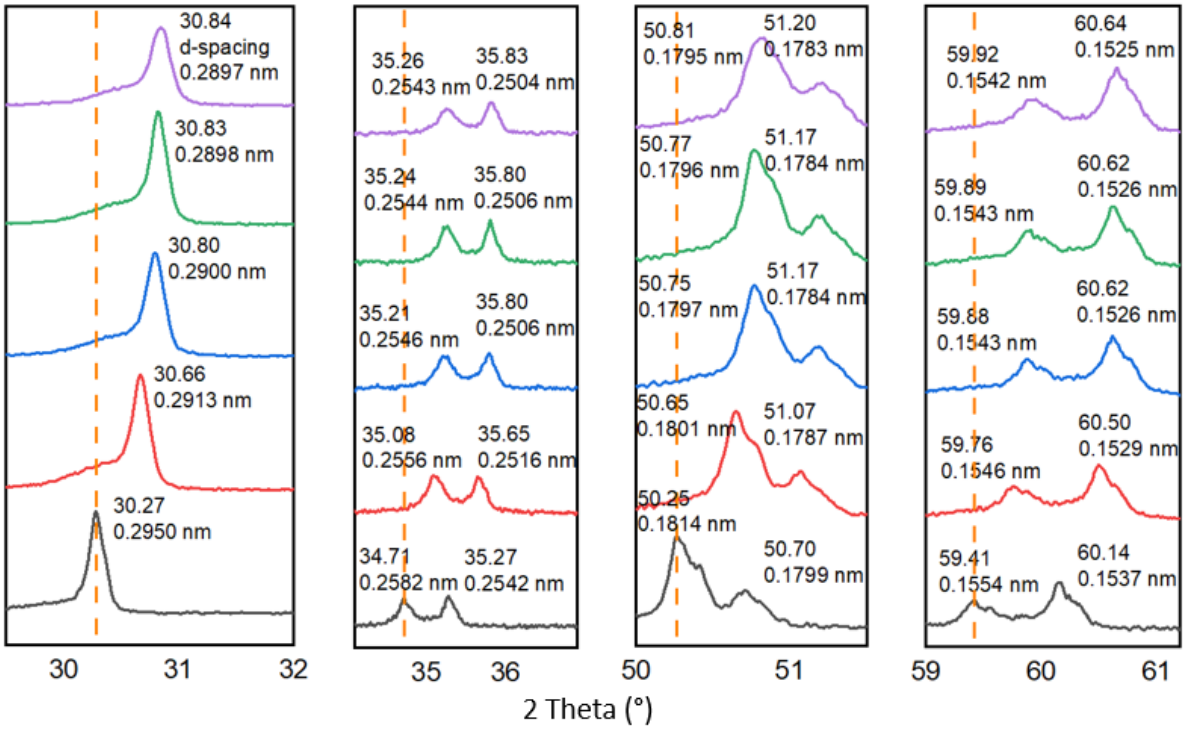

Figure 5-20. The detailed scan revealed characteristic peaks for each zirconia samples treated at various temperatures (The orange dotted line indicates the positions of the different peaks of the untreated zirconia for comparison with the plasma treated sample).

5.6.2 X-ray diffraction (XRD) analysis from sample treated with different gases.

The systematic experimental gas design was used to investigate the effects of the different atmospheres on blackening, including hydrogen and nitrogen, while the remaining conditions were kept constant (500 °C, 3 mbar, DC). In past studies, the temperature and cathodic potential have been shown to play an important role in the transformation kinetics; however, in this section, the size of atoms has also been demonstrated to play an essential role in the transformation rate and the following crystal structure and properties. From the results, both gases treated samples observed blackness, which indicates that the black colour of the samples is not directly related to the difference from the atmosphere. However, the XRD pattern (Figure 5-21) interestingly showed that more monoclinic phases (peak 28.9 °) were observed in the

nitrogen-treated sample but not in the hydrogen-treated sample, which suggests that despite both treatments leading to uniformly blackened samples, differing processes arise between nitrogen and hydrogen treatments. The newly added M-phase can be understood as a phase transformation of the zirconia due to its metastable state (which gives rise to its transformation toughening behaviour). The formation of the monoclinic phase may be induced by the impact of high-speed charged particles on the sample surface during the plasma bombardment process. As the effective mass of nitrogen ions is greater than that of hydrogen ions, it can be inferred that the momentum imparted during the bombardment process from nitrogen ions will introduce more energy, and can more readily facilitate the phase transformation.

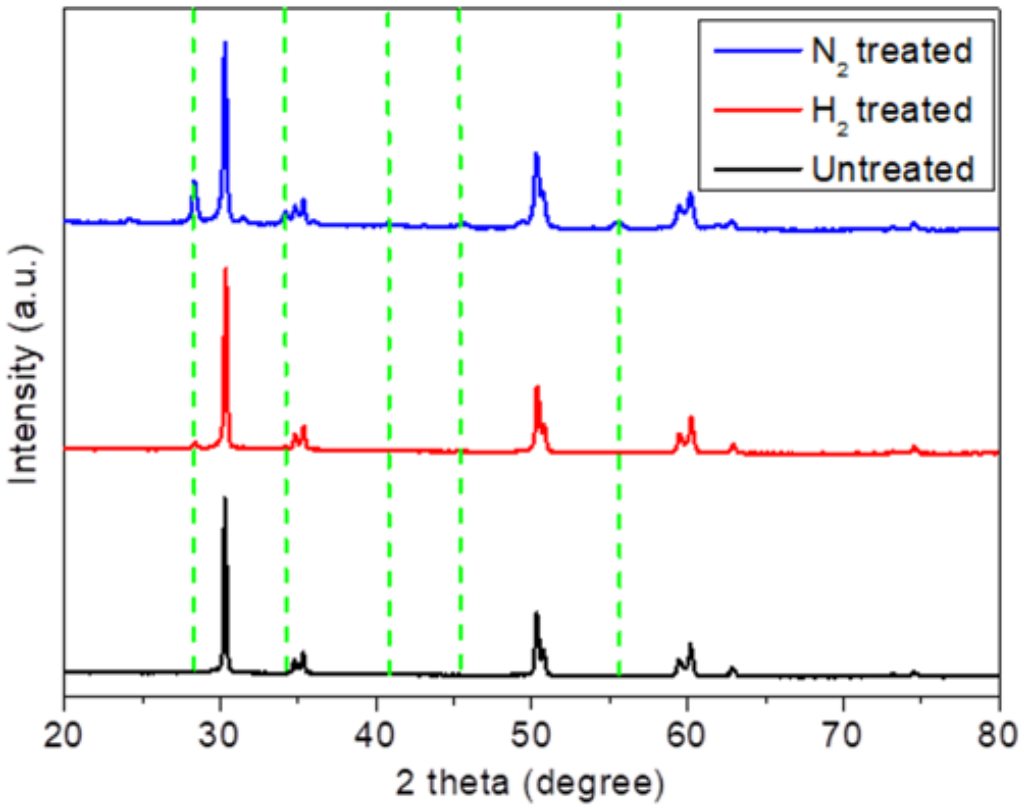

Figure 5-21.The XRD pattern from different gas-treated zirconia.

5.6.3 The other methods to accelerate plasma treatment.

Several techniques have also been explored to accelerate the plasma-blackening process of zirconia, which show potential for future industrial scale up. The techniques introduced in the following section are (1) the pre-sputtering of a conductive surface (gold) prior to plasma treatment (as shown in Figure 5-22) and (2) the introduction of an in-situ sputtering and heating source during the treatment (three stainless steel blocks). Zirconia, being a conventional ceramic material, is considered as a non-conducting material. Consequently, during the initial stages of plasma treatment, the sample acts as an insulating material and is not subjected to ionic bombardment. However, the addition of the gold coating enables the formation of a thin conductive surface, thereby creating a conductive “skin”, which can serve to enable plasma bombardment and to help heat up and process the material more efficiently at the very early stage of the treatment process (as mentioned in Section 5.4.5). Moreover, this method is non-destructive as the gold layer is gradually sputtered away from the sample surface through the plasma bombardment process.

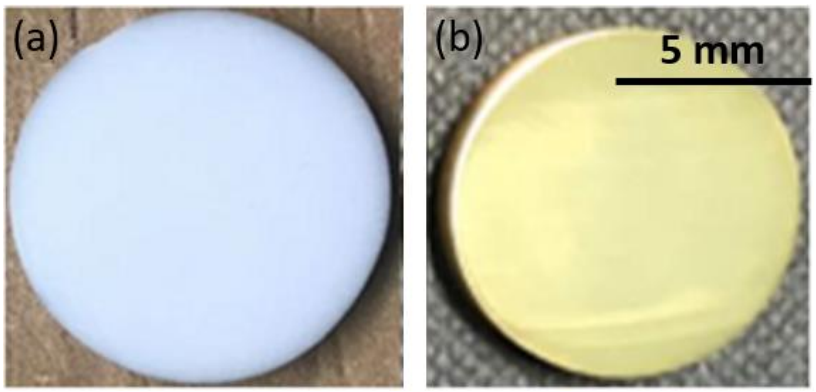

Figure 5-22. (a) pristine and (b) gold coated sample.

As illustrated in Figure 5-23a, three equally sized stainless steel blocks were uniformly arranged around the sample before plasma treatment.

The purpose of this setup serves three main objectives. First, unlike zirconia, stainless steel is an excellent conductor of electricity. Thus, it can interact significantly with ionised ions right at the beginning of plasma treatment, forming an ions cloud region cantered around the stainless steel block (as depicted in Figure 5-23b, where negative glow discharge is observed around the stainless steel block, unlike the zirconia sample). This ions cloud plays a guiding role during plasma treatment, making the region covered by the cloud more susceptible to plasma bombardment. Simultaneously, these three stainless steel blocks can increase local current density, intensifying the treatment of ions in that area and accelerating ion energy absorption and reaction rates.

Second, stainless steel, as an excellent thermal conductor, also undergoes rapid heating due to the plasma bombardment (unlike insulating ceramic materials). Consequently, heat radiation away from the blocks leads to the inner regions of the enclosed space to heat up significantly faster than other areas of the plasma furnace, therefore accelerating the heating up stage of the sample during the plasma treatment.

Third, due to the plasma bombardment process, the three stainless steel blocks release (sputter) some of their surface material onto the zirconia samples and their surroundings. This helps to form a conductive surface layer on the insulating ceramic as well as replenishing the layer throughout the treatment process. This process can accelerate the ions bombardment process and increase the reaction rates and enhance the transformation rate of the plasma treatment process.

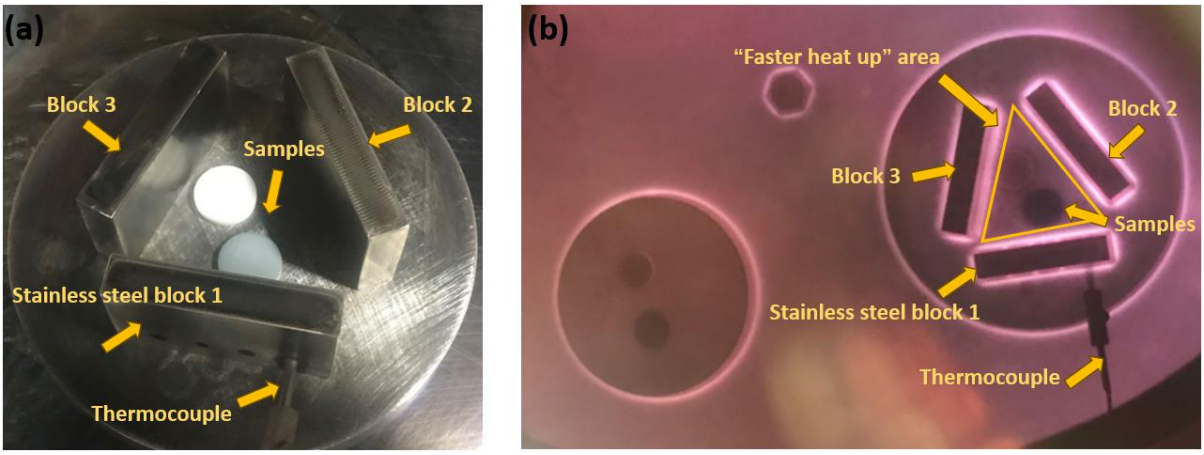

Figure 5-23. Plasma setup figure (a) depicts three stainless steel blocks uniformly positioned around the sample before the treatment, while (b) contrasts the fast heat up area formed by the three stainless steel blocks during the plasma treatment with the sample stage lacking the benefits.

Chapter 6 Plasma-Defect Engineering Repair of Macro-Indentation Cracks in Zirconia

Note: A letter paper based on the plasma cracking healing of zirconia has been submitted to **Scripta Materialia** for publication.

Contributions: (Conceptualization: equal; Data curation: Lead; Formal analysis: Lead; Investigation: Lead; Methodology: Supporting; Validation: Supporting; Writing – original draft: Lead; Writing – review & editing: Lead).

Abstract

Zirconia, recognised for its robust nature owing to its remarkable combination of properties such as high hardness, chemical stability, and biocompatibility, has been extensively utilised across numerous areas including biomedical engineering, catalysis, and electronics. However, in harsh environments characterised by high pressure and high temperatures, cracking often develops due to the formation of T-M phase transformation and localised defects, subsequently leading to the development of significant cracks, resulting in material failure. Although the inherent transformation toughening properties of zirconia, which do to some extent prevent the generation and propagation of cracks, further refinement is still warranted. In this study, we present a novel low-pressure (300 Pa) plasma treatment (N_2 gas at 500 °C for 10 hours) capable of inducing crack-healing of zirconia, allowing for non-destructive restoration of both surface and deep microcracks. Crack-healing phenomena are revealed using a combination of SEM imaging and laser milling performed in-situ to expose both surface and bulk segments of cracks. In combination with XRD spectra, surface Raman maps of cracks produced by 5 and 20 kgf Vickers indentations showcase the subsequent repair following the plasma-induced tetragonal-to-monoclinic phase transition. Low-pressure plasma treatment of zirconia presents a promising strategy for the repair of zirconia materials via a cost-effective, scalable and environmentally friendly approach. Moreover, plasma-treated zirconia is also found to exhibit a unique combined enhancement of surface hardness and fracture toughness.

6.1 Introduction

As a vital ceramic, zirconia is widely used as a structural material in engineering applications due to its high mechanical properties, exceptional thermal stability, and chemical resistance [5, 25, 325]. However, the cracking of zirconia presents certain limitations when exposed to high-stress environments, impacting its practical applicability [326-330]. Exploring the crack-healing of zirconia aims to enhance the mechanical properties, extend the operational lifespan, and increase the material reliability of zirconia. Therefore, realising this goal can have substantial ramifications to expand the utilisation across the aerospace, engineering, and biomedical domains [331, 332].

The phase transformation of in zirconia can be achieved by manipulating temperature and pressure [333, 334]. Wang and Stevens healed the cracks on TZP (ZrO_2 – 3 mol% Y_2O_3) by thermal treatment (1250 °C for 20 min) and they concluded that it is essential for crack healing to conduct the thermal treatment above the ZrO2 (t) $\rightarrow$ ZrO2 (m) transformation temperature [297]; Houjou and co-researchers investigated crack-healing behaviour of ZrO2/SiC composites during thermal treatment in air or N2 gas at 600-1350 °C for 1-100 h and they found that SiC and oxidative environment are necessary for healing cracks in ZrO2/SiC composites [298-299]. More recently, Shunsuke and co-researchers (2023) healed microcracks formed by micro-Vickers indenter in single-crystal cubic zirconia (ZrO_2 – 10 mol% Y_2O_3) by thermal annealing (1250 °C or 1400 °C for 10 min) [333, 335].

The pioneering work by Raj et al. (2011) [301] demonstrated the efficacy of flash events under DC electric fields for sintering. Takahashi et al. healed cracks artificially

formed using a micro-Vickers indentation technique in 8 mol% Y_2O_3-stabilised cubic ZrO_2 (8Y-CSZ) polycrystals under a DC electric field at a relatively low temperature of 800 °C in an electric furnace [336]. However, Pt wire electrodes and Pt paste must be used to connect to the DC source forming a DC electric field to promote the healing process.

The author of this study has discovered for the first time the healing of cracks in zirconia by low pressure plasma treatment, which is scientifically interesting and technologically important. Notably, plasma treatment eliminates the need for direct electrode contact, presenting a clear advantage for potential application. Furthermore, plasma treatment can be conducted at lower temperatures (<550°C) than that for thermal crack healing and DC electric field enhanced cracking healing.

Consequently, this study aimed to investigate the possibility of healing macrocracks and the fundamental mechanisms involved in the crack-healing of zirconia through low-pressure plasma treatment. The optical images of the surfaces and cross-sections of macrocracks formed by Vickers indenter under loads ranging from 5 to 50 kgf) were compared and analysed to assess the extent of crack healing. Combined with the results from XRD spectra and Raman mapping, the phase transitions around the indentations were analysed to comprehend the underlying mechanism for the repair of the cracks. It is expected that the outcomes of this investigation will advance scientific understanding of the mechanism involved in the plasma crack-healing of zirconia and contribute to the future development and optimisation of this novel, cost-effective, and environmentally friendly plasma-defect engineering route.

6.2 Materials and Methods

6.2.1 Sample preparation

Samples of 3 mol-% yttria-stabilised tetragonal zirconia rods (10 mm diameter) were cut into 3mm thick cylindrical coupons (Struers Accutom 50) with a cubic boron nitride cutting wheel. Samples were then ground to #1200 grit size using SiC paper before polishing with diamond suspensions with particle sizes of 6, 3, and 1 μm. Different indentation loads (from 5 and 50 kgf) were produced on the surface of mirror polished samples (Struers Duramin-40).

6.2.2 Plasma treatment

Samples were treated for 10 hours using a Klöckner Ionon 40 kVA plasma furnace under N_2 atmosphere and a working gas pressure of 3 mbar (300 Pa).

After the plasma treatment, gentle surface polishing (using a one-micron polishing sheet for approximately 10 seconds) was conducted to achieve a smoother surface and to remove the deposited layer formed during the plasma process. It is crucial to remove this surface deposition layer because its complex composition may affect subsequent crack characterisations, such as covering cracks and making them unobservable, or introducing impurity phases during surface Raman scanning. The deposition layer on the sample surface post-plasma treatment can be primarily attributed to the following factors: the formation of compounds from residual gas in the plasma interacting with the ceramic surface, the vapor deposition effects of impurity gases (in trace amounts), and the generation of NxMy-type compounds from the interaction of gas and metal ions from the worktable during plasma sputtering (as mentioned in Section 2.4.2).

6.2.3 Optical images

Optical images of the indentation were acquired using a Zeiss optical microscope. The input light was adjusted to a setting of 2, while the grating was maintained in its original mode. To capture comprehensive images accommodating the various indentation sizes, X5 and X10 objectives were used accordingly. The calculation of the indentation dimensions (cracks and indentation area) was performed using ImageJ software.

6.2.4 Raman mapping

Raman scanning was conducted using a Renishaw inVia Raman microscope fitted with a 532 nm excitation laser source and groove density of 1800 l/mm to identify the light absorption capabilities and constituent phases (tetragonal and monoclinic phases). The data were then further analysed using Casa XPS and Origin software packages for deconvoluting the respective spectra and graphing.

6.2.5 Laser milling

A femto-second laser beam in a Hydra-Laser Tribeam microscope was used to prepare the cross-section slice of the sample. SEM images were taken on the cross-section slices after each laser milling.

6.2.6 X-ray diffraction (XRD)

Crystal structures and phase analysis were carried out using XRD (proto AXRD Benchtop) with Cu Kα irradiation (wavelength 0.15406 nm) operated at 40 kV and 30 mA. Pattens were generated from 20-80 ° angles, with step increments of 0.01493 °. Scherrer's equation calculated the average crystallite size: $D=K\lambda/(\beta\cos\theta)$, in which K is Scherrer constant, β is the half-peak height width or integral width of the diffraction peak, θ is Bragg Angle, λ is X-ray wavelength (0. 15406 nm).

6.2.7 Hardness and toughness

Vickers indentations under loads of 300 gf and 10 kgf were used to evaluate the respective hardness and indentation-based fracture toughness of the samples by using Struers Duramin-40. To determine hardness values, the average diagonal lengths of the indents were measured and calculated using equation (1). Fracture toughness measurements were calculated using either equation (2) or equation (3). The ratio of the total crack length (c) across the indent to the half indent diagonal length (a) determined the choice of equation, with equation (2) employed for c/a ≥ 2.5 and equation (3) used for c/a < 2.5 [337].

$$HV = 1.854\frac{F}{(2a)^2} \qquad (6\text{-}1)$$

$$K_{IC} = 0.0752 \cdot \frac{F}{c^{\frac{3}{2}}} \qquad (6\text{-}2)$$

$$K_{IC} = 0.0319 \cdot \frac{F}{0.5 \cdot a \cdot l^{\frac{1}{2}}} \qquad (6\text{-}3)$$

6.3 Results

6.3.1 Sample colour transformation

Figure 6-1 illustrates the process of plasma-induced self-healing in zirconia micro-cracks, accompanied by distinct changes in the sample's colouration. In Figure 6-1 (a), the untreated zirconia sample appears white, resembling normal 3 mol% Yttria-Stabilized Zirconia (3YSZ). The sample's surface exhibits indentations from various loads ranging from 5 kgf to 50 kgf. Figure 6-1 (b) presents the sample treated with N2 at 500°C for 10 hours, resulting in the entire sample turning black, indicative of the transformation to oxygen-deficient zirconia, as previously reported (as shown in Chapter 4). After the removal of the original deposition layer, resulting in Figure 6-1 (c), the black colouration in the centre of the sample remains visible. Figure 6-1 (d) exhibits the sample after the oxidation reaction, during which the oxygen vacancies in the oxygen-deficient zirconia are re-filled, causing the zirconia to revert to its original white colour, consistent with the appearance of the untreated sample. The subsequent re-oxidation treatment is employed to maintain a uniform colour with the untreated sample, preserving its applicability in various potential applications without compromising its appearance.

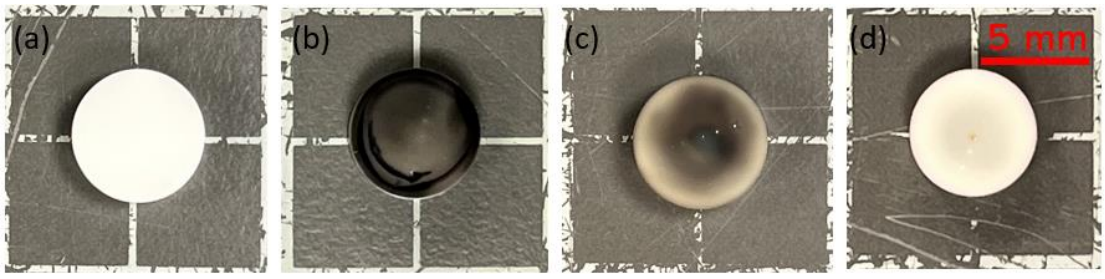

Figure 6-1 Optical images from the zirconia top surface (a) before the plasma treatment, (b) after the treatment (N2-500 °C -10h) with the deposition layer, (c) removed deposition layer by gentle polishing, and (d) after thermal oxidation treatment (air-600 °C -10h).

6.3.2 Surface crack healing

Figure 6-2a1 depicts the untreated sample with 20 kgf Vickers indentation, revealing four microcracks extending along the direction of indentation, each with an average length of 141±3 μm. In Figure 6-2a2, magnified images of these microcracks from the untreated sample provide clearer visibility of their morphology. Notably, the indentation on the untreated samples appears to correspond to the shape of the Vickers indenter, with only a slight curvature at each edge.

Figure 6-2b1 displays the surface picture of the sample after DC plasma treatment. Interestingly, the extended microcracks around the indentation cannot be seen anymore, even at the crack base. The edges of the indent also appear significantly more curved than the untreated indents. Figure 6-2d further highlights the surface morphology of the microcracks and highlights the repaired state. The cracks after plasma treatment appear flat, and the original crack gaps are filled, leading to a promising healing effect. Under optical imaging, no traces of the original crack are visible and the surface appears unblemished, making it difficult to discern the location of the initial crack. Furthermore, an interesting observation is made regarding the size of the indentation. This is reflected in the average diagonal length measurements: the plasma-treated sample exhibits an average diagonal length of 162.48 ± 1.60 μm, which has a 2.04 % decrement compared with the untreated diagonal length of 165.86 ± 0.79 μm, and the overall area of the indentation was reduced by 10.59 %, decreasing from 12,895.47 ± 44.45 to 11,530.44 ± 55.46 μm². The decrease in indentation size may be attributed to the material's response to the plasma treatments: plasma treatment induces a phase transformation surrounding the indentation from a tetragonal phase to a monoclinic phase, leading to expansion. This expansion causes a reduction in indentation dimensions.

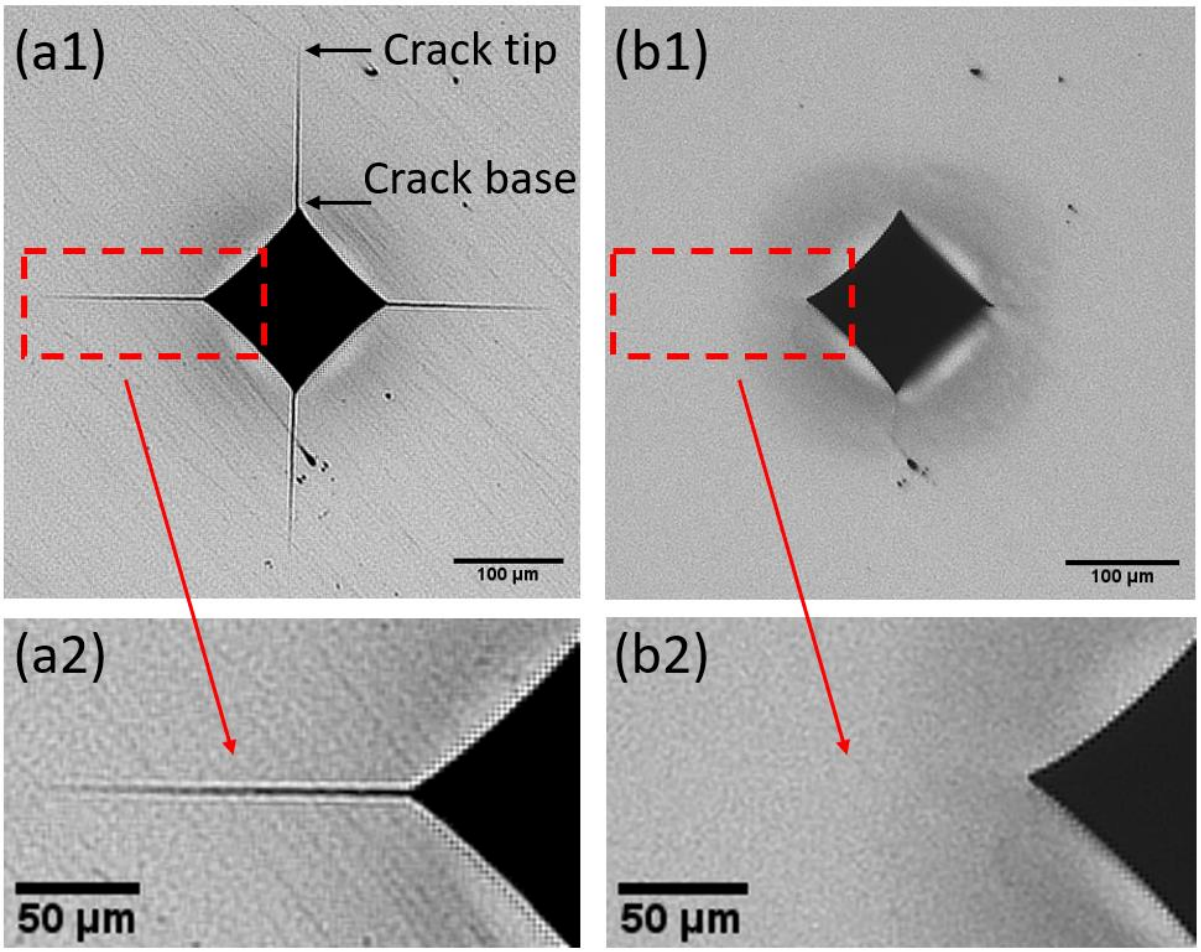

Figure 6-2 Optical images of 20 kgf indentation on the zirconia top surface (a) before the plasma treatment and (b) after plasma treatment, (1) overview figures and (2) detailed figures of the left microcrack of the indentation (as marked by the black arrow: The distal end formed by indentation is referred to as the "crack tip", while the side closer to the indentation is defined as the "crack base").

In order to preliminarily investigate the efficacy of nitrogen plasma treatment in crack repair, data on indentation sizes obtained under different loads were collected (5, 10, 20, 30, and 50 kgf, with the 20 kgf data are shown in Figure 6-2 and the rest are in Figure 6-3). It is evident from the figures that nitrogen plasma treatment at 10 hours, 3 mbar, and 500°C can fully repair cracks formed under loads of 10 kgf and below.

However, starting from 20 kgf, cracks are only partially repaired. In Figure 6-3b3, it is clear that the healing effect is pronounced at the tips of the cracks, while there is no fully repair near the indentation side (at the bottom of the crack). This trend is particularly noticeable in the images of cracks formed under a 50 kgf load. This group experiments reveal an approximate limit to the crack-healing property achieved by plasma treatment under a certain set of parameters. Nevertheless, plasma treatment for ceramic modification is a highly complex process, with the healing process involving the formation of oxygen-deficient zirconia and the phase transformation between monoclinic and tetragonal phases. Therefore, the extent of crack repair is believed to not have a direct linear relationship with factors such as temperature, duration, and gas pressure, but necessitating further in-depth and systematic exploration. It is worth noting that the crack healing for large-scale cracks is more akin to a plasma-induced local enhancement of the m-phase. Since cracks under large loads (above 20 kgf) are not completely healed, reapplying regional stress to the original cracks may result in their reappearance. However, compared to previously published studies (as shown in section 6.1), the degree of repair achieved in this research for 5 kg and 10 kg indentations is still showing its value.

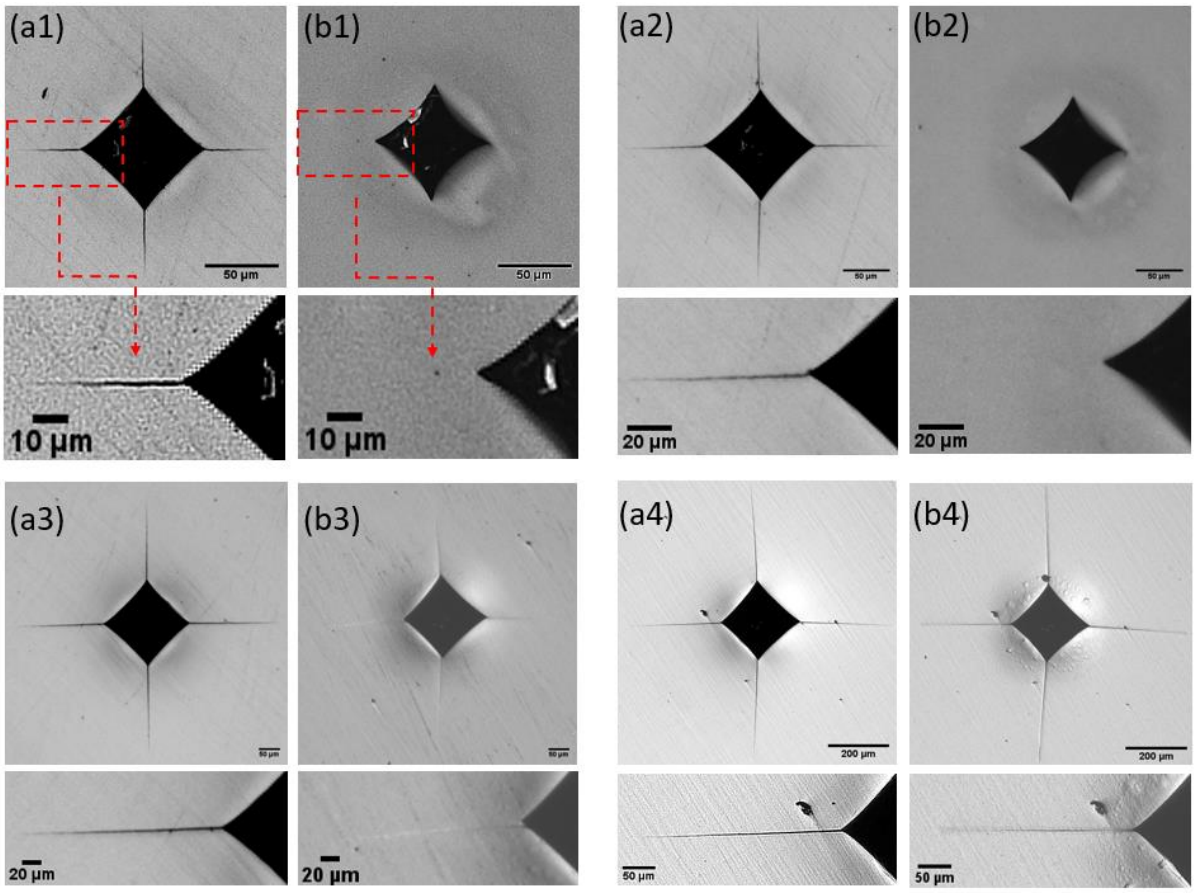

Figure 6-3 Optical images of full-scale indention from 5 kg-50 kgf where group (a) is un-treated sample (b) is N_2-plasma-treated sample and 1 shows from 5 kgf indentations, 2 for 10 kgf, 3 for 30 kgf, 4 for 50 kgf.

In order to gain a detailed understanding of the extent to which plasma treatment repairs cracks in zirconia, the average diagonal length of indentations and the average distance from the midpoint of one side to the midpoint of an adjacent side were measured and tabulated (shown in Table 6-1), the bend rate was obtained by calculating the fraction of the distance reduction at the midpoint of the opposite edge divided by the data from the untreated sample. Across all measurements of indentations formed under different loads, the area of indentations consistently decreased after plasma treatment, providing supportive evidence of expansion caused

by the phase transition from tetragonal to monoclinic phase. Due to the larger volume of indentations compared to cracks, they do not completely heal but still exhibit a trend of reduction. Interestingly, the reduction ratio diminishes as the indentations decrease in size, demonstrating that the induction of zirconia phase transition under fixed plasma treatment conditions remains approximately constant and does not vary with indentation size. Furthermore, it is visually evident from the table that there is not a significant difference in the area of indentations after heat treatment compared to after plasma treatment, thus corroborating the conclusions drawn from the data obtained in Section 6.3.1. The limitation of this experimental set lies in the fact that all data are based on two-dimensional manual measurements of indentation surfaces. Utilising means to obtain three-dimensional graphs of indentation volumes or relying on instrumentation could potentially yield more convincing data.

Table 6-1 Indentation Size Data of Untreated, Plasma Treated, and Thermal Oxidation Treated zirconia

N2					
Indentation (kgf)	Type	Average--Diagonal Distance (μm)	Decrease (%)	Average--Vertical Distance (μm)	Bend Rate
2.5	Unt	59.32	-	38.45	-
	Plasma-treated	54.86	7.52%	32.93	14.36%
	Thermal oxidation	53.61	9.63%	33.39	13.16%
5	Unt	83.365		56.45	
	Plasma-treated	78.635	5.67%	46.49	17.64%
	Thermal oxidation	78.67	5.63%	45.435	19.51%
10	Unt	119.38		78.63	
	Plasma-treated	110.92	7.09%	65.5	16.70%
	Thermal oxidation	110.285	7.62%	63.56	19.17%
20	Unt	165.865		111.765	

	Plasma-treated	162.48	2.04%	106.46	4.75%
	Thermal oxidation	161.92	2.38%	106.97	4.29%
30	Unt	202.535		135.84	
	Plasma-treated	201.48	0.52%	135.425	0.31%
	Thermal oxidation	200.23	1.14%	135.485	0.26%
50	Unt	261.64		173.625	
	Plasma-treated	261.17	0.18%	172.895	0.42%
	Thermal oxidation	259.03	1.00%	173.345	0.16%

6.3.3 Bulk crack healing

Figure 6-4 provides further insights into the crack healing process from the bulk, with a cross-sectional images produced using laser milling of the crack formed by 20 kgf Vickers indents. On the crack's upper side (Figure 6-4b1), the untreated sample had a gap width of 2.47 μm, indicating clear crack propagation in the longitudinal section. Conversely, the treated sample (Figure 6-4b2) exhibited a much narrower crack width of 0.53 μm, approximately one-third of the untreated sample. This significant reduction in crack width indicates effective repair is achieved through plasma treatment. Similarly, as shown in Figure 6-4c1, the middle section of the crack displayed a surface crack width of 1.21 μm, while the repaired width was only 0.39 μm, as observed in Figure 6-4c2. This repair at the middle section aligns with the healing observed at the bottom of the crack. Interestingly, the observation of bulk healing occurring approximately 92 μm from the sample surface indicates that the healing process extends from the surface to the body core of the plasma-treated sample's.

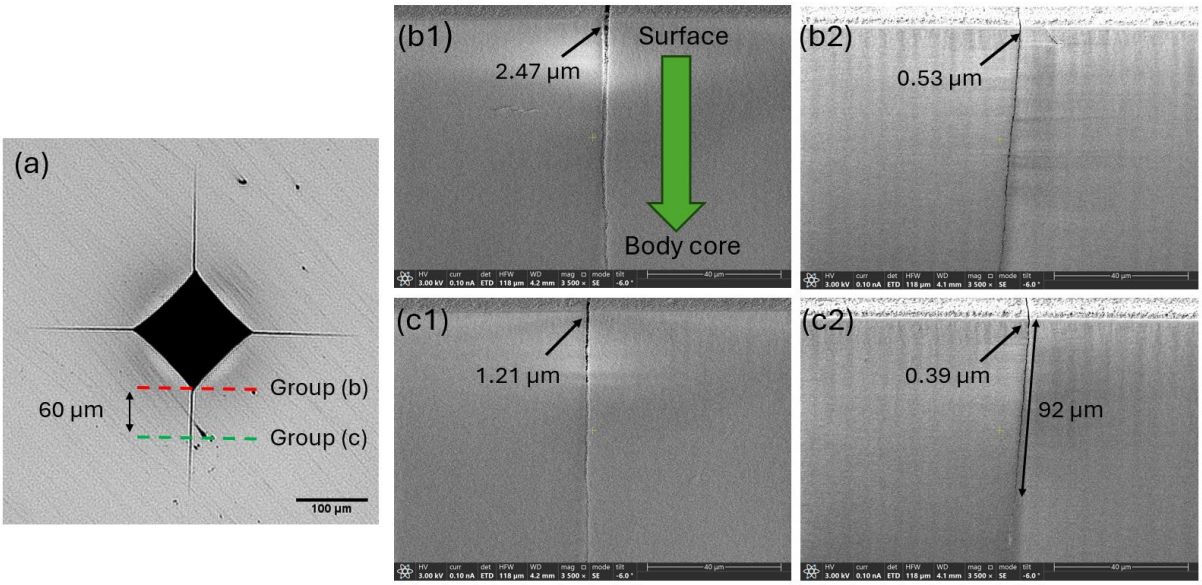

Figure 6-4 Optical images of 20 kg indentation on the zirconia top surface: (a) the locations of the laser milling: one adjacent to the indentation (red line) and the other approximately 60 µm away from the base (green line); the cross-section figures mill from the crack base of the (b1) un-treated sample (the green arrow indicating the crack's propagation from the sample surface to the body core) and (b2) plasma-treated sample (c1) the cross-section figures from 60 µm away from the crack base of the (c1) un-treated sample and (c2) plasma-treated sample.

6.3.4 Phase transformation evidence

Accompany by the significant morphological changes in crack healing, XRD analysis of the plasma-treated sample reveals the presence of a newly added monoclinic character peak at 28.9° in the crystallographic phase structure, as depicted in Figure 6-5a. Both the untreated and plasma-treated zirconia could be indexed using standard patterns corresponding to 3% yttria-stabilised zirconia (PDF #48-0024). A subtle modification in the monoclinic phase content was discernible, as indicated by the red dotted line at 28.9°. With further demonstration provided by the high-resolution scan

from 27.5° to 29.5° (Figure 6-5b), the newly added monoclinic signal of the plasma-treated sample was measured to be 3.41 times greater than that of the untreated sample. Notably, the untreated sample also exhibited the monoclinic phase due to its composition as yttria-stabilised zirconia, an inherent characteristic of the material. However, the plasma-treated samples showed a significant increase in monoclinic phase compared to the untreated samples, attributable to the effects of plasma treatment. The absence of phase transformations (T-M) and the retention of the 3% yttria-stabilised zirconia pattern suggest that plasma treatment might influence the material's microstructure, potentially contributing to the observed phenomena in crack healing and material mechanical performance.

To further investigate the phase information before and after the plasma treatment along the indentation, Raman surface mapping was employed. In Figure 6-5c, the untreated sample exhibits a small monoclinic phase around the 5 kgf indentation. This observation aligns with the phenomenon reported in the literature, where tensile stress induces a phase transition from the tetragonal to monoclinic phase around the indentation, contributing to zirconia's transformation and toughening characteristics. Conversely, as seen in Figure 6-5d, the plasma-treated samples display an increased monoclinic phase formation around the indentation, which is consistent with the XRD findings, further corroborating that the plasma treatment also can induce phase transition (from tetragonal to monoclinic) around the indentation. However, it is worth noting that the phase distribution around the crack is not as distinct as around the indentation, this can be explained by the direction of the new phase generation, that the phase growth occurring from the inside to outside, i.e., originating from the centre of the body core and extending outward (vertically from the deepest part or tip of the crack). As a result, this internal growth of the phase cannot be directly observed on

the surface, which is evident from the curvilinear nature of the side length around the indentation instead of a straight line as shown in Figure 6-1.

Simultaneously, detailed scanning of the microcracks adjacent to the 20 kgf indentation was conducted to assess the consistency of the phase distribution around the crack with the 5 kgf indentation full scanning results. The distribution of the monoclinic phase in the untreated sample aligns with the observations in Figure 6-5e, primarily concentrated along the indentation. This can be attributed to the transformation from the tetragonal phase to the monoclinic phase induced by the vertical compressive stress during the indentation formation. Figure 6-5f exhibits the monoclinic phase distributions after nitrogen plasma treatment. Resembling the 5 kgf scan results, the plasma treatment induced a more substantial presence of the monoclinic phase around the indentation. However, it is worth noting that the phase distribution around the crack is not as distinct as around the indentation; the phases near the crack in the three plots appear consistent on the surface. This can be explained by the direction of the new phase generation, that the nascent phase growth occurs from the inside to outside, i.e., originating from the centre of the body and extending outward (vertically from the deepest part or tip of the crack). As a result, this internal growth of the phase cannot be directly observed on the surface, which is evident from the curvilinear nature of the side length around the indentation instead of a straight line as shown in Figure 6-2.

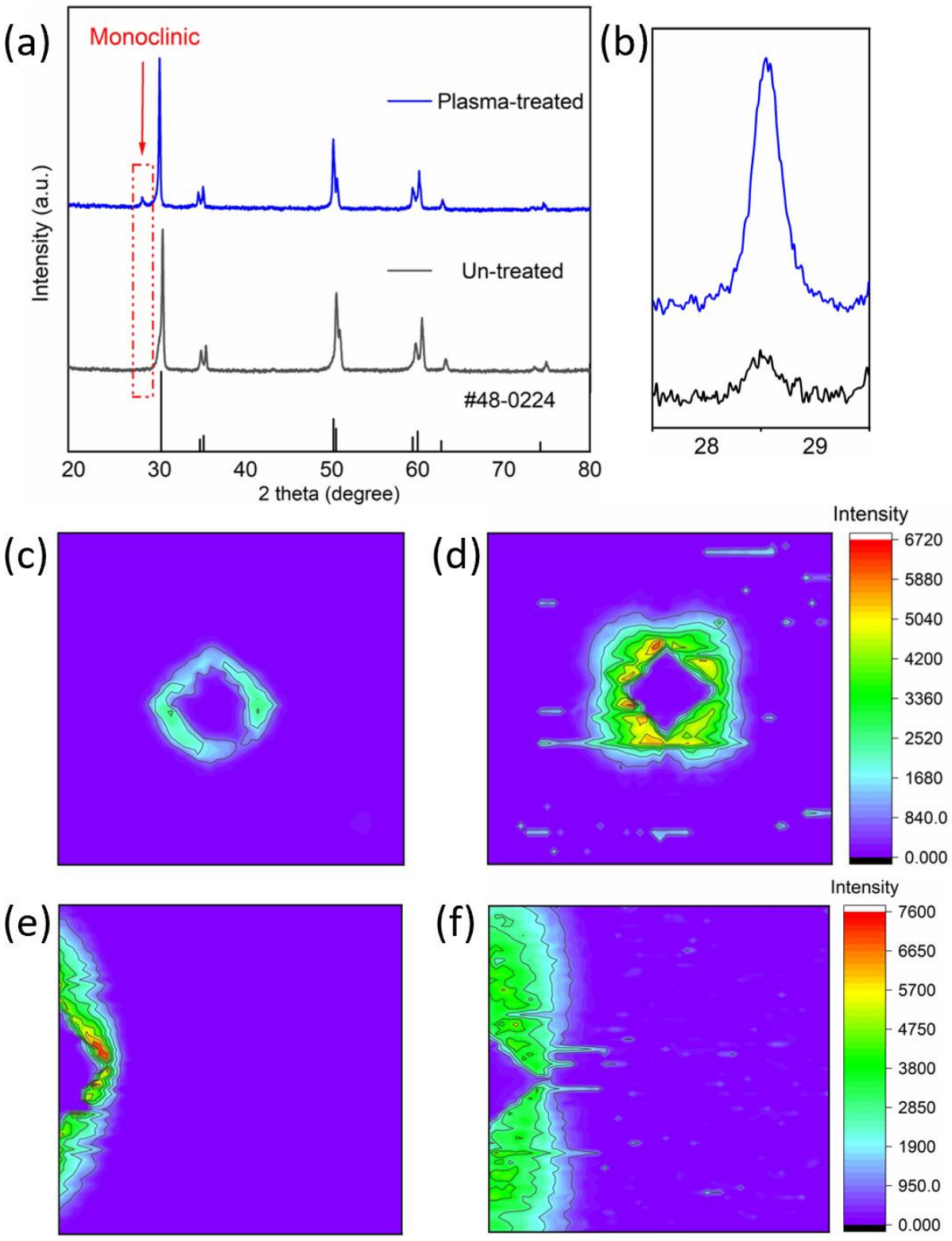

Figure 6-5 XRD patterns of the zirconia from the Un-treated and plasma-treated sample; (b) the detailed scanning from 27.5° - 29.5°, Raman surface mapping of the monoclinic phase distribution near the indentation under a load of 5 kgf of the (c) untreated zirconia and (d)

plasma-treated sample, the right crack's monoclinic phase Raman mapping under a load of 20kgf of (e) untreated zirconia, (f) plasma-treated sample.

6.3.5 Retaining healed cracks following re-oxidation treatment

Although the sample reverted from black to white due to the re-occupation of oxygen vacancies after thermal oxidation treatment, the healed nature of the cracks was not lost. Figure 6-6a illustrates the overall appearance of a 5 kgf indentation, showing that each crack remained intact and repaired, consistent with the situation after plasma treatment as shown in Figure 6-2. Raman scans (Figure 6-6c) also confirmed this observation, with the intensity of the monoclinic phase around the indentation only showing limited difference from that of the plasma treated sample. This implies that the monoclinic phase generated by plasma treatment exhibits sufficient thermal stability below 600 °C and does not become ineffective due to the re-oxidation process. This finding opens up broad possibilities for the plasma-assisted healing of cracked zirconia, as it demonstrates that plasma treatment can induce large-scale crack self-repair without altering the sample's colour, thus providing extensive avenues for further exploration.

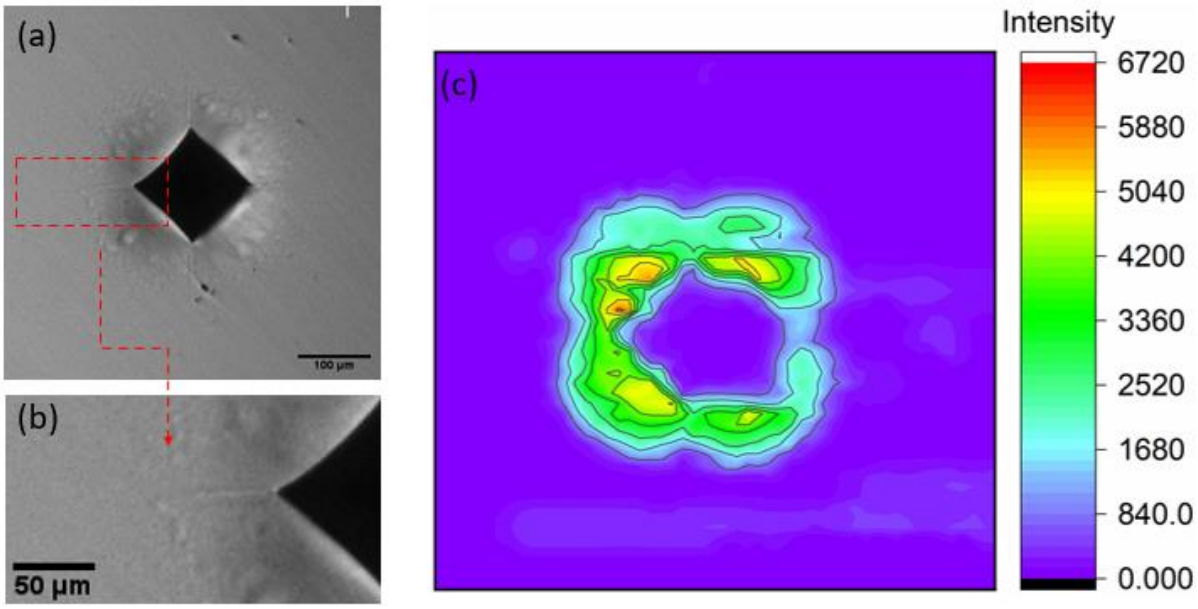

Figure 6-6 Optical images(a) of 5 kgf indention after TO treatment (base on the sample treated by N2-10h-500 °C), (b) the detailed figure for the left crack and (c) Raman mapping of the 5 kgf indention keep the sample intensity bar as the previous one.

Furthermore, plasma treatment using different gases has been demonstrated to effectively repair cracks in zirconia. As depicted in Figure 6-7, the morphology around the 5 kgf load after H_2-10 hours-500 °C treatment was obtained, showing a noticeable repair effect on the cracks. Raman scans of the indentations also confirmed the presence of a newly formed m-phase around the indentations.

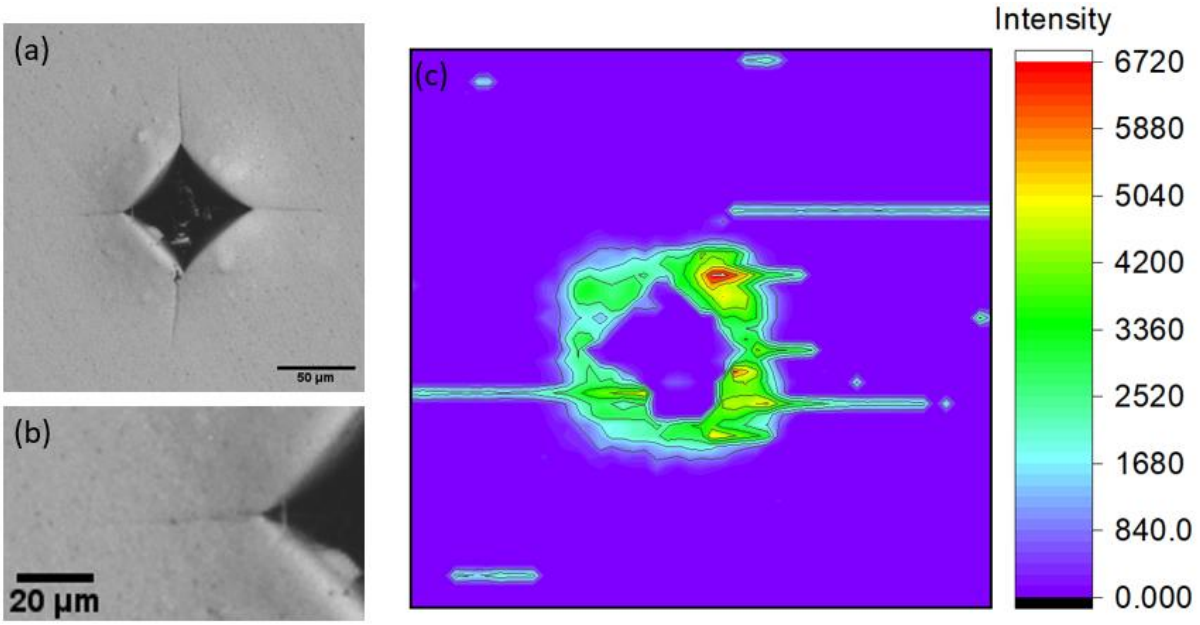

Figure 6-7 Optical images (a) of 5 kgf indention after H2-10h-500 °C plasma treatment, (b) the detailed figure for the left crack and (c) Raman mapping of the 5 kgf indention keep the sample intensity bar as the previous one.

Moreover, accompanying the process of crack-healing, the surface hardness of plasma-treated zirconia was enhanced. Unlike numerous studies reporting on oxygen-deficient zirconia, plasma treatment can directly treat bulk polycrystalline YSZ, whereas most other approaches obtained samples in powdered or thin-layered form, hence unable to characterise mechanical properties. The hardness results were depicted in Figure 6-8: the untreated sample exhibited a hardness of 1246HV0.3/20, whereas after plasma treatment, the hardness increased significantly to 1351, demonstrating a notable improvement. This significant enhancement persisted even when the pressure was increased to 0.5 kgf. Simultaneously, the sample's fracture toughness showed a slight improvement under different loads (5 and 10 kgf). This indicates that, during the process of plasma-induced zirconia crack self-healing, not only were the cracks partially repaired, but also the mechanical performance of the

samples was improved, thereby enhancing the reliability and stability of zirconia in subsequent applications.

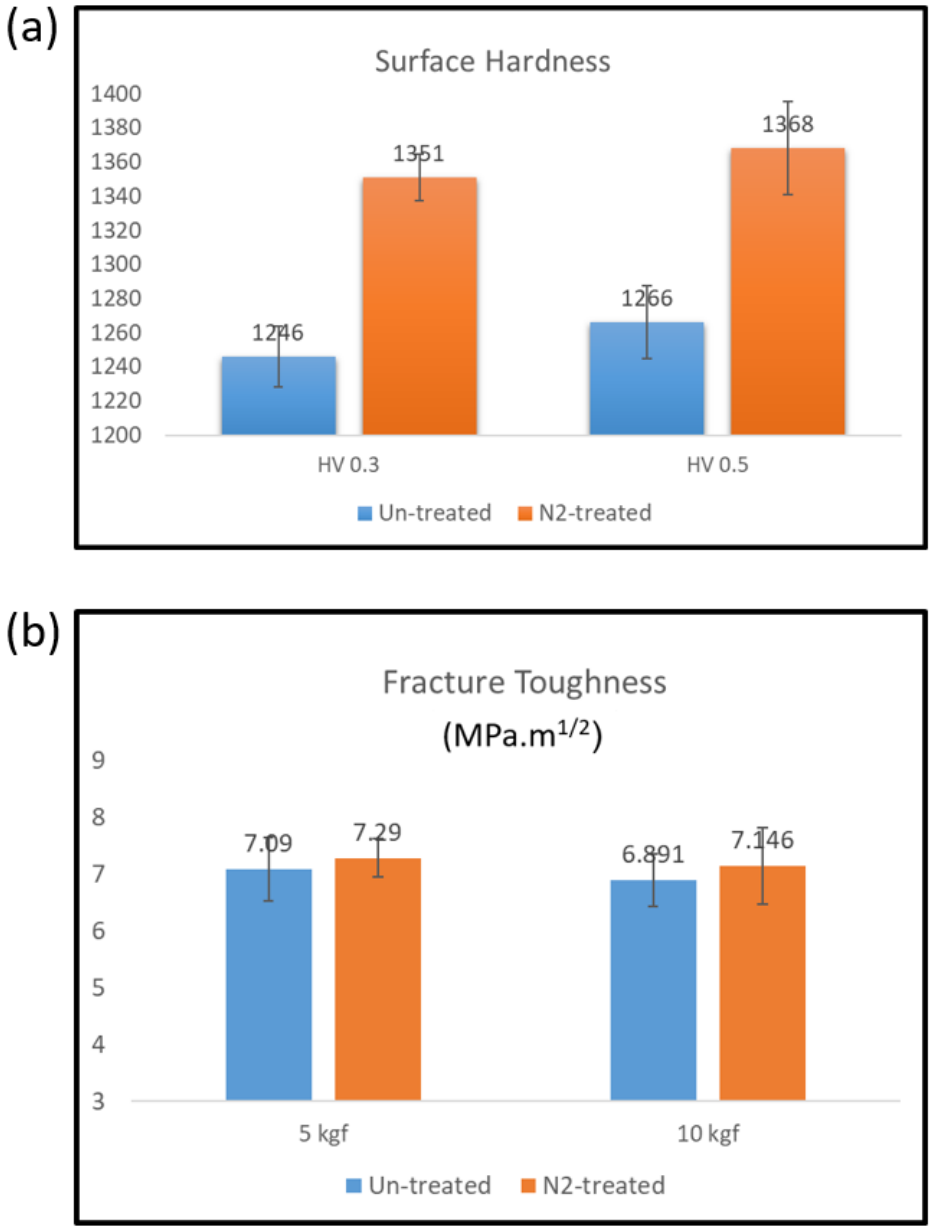

Figure 6-8 Comparison between untreated zirconia and plasma-treated zirconia of (a) surface hardness under different loads (0.3 kgf and 0.5 kgf) and (b) fracture toughness under different loads (5 and 10 kgf).

6.4 Discussion

Low-pressure plasma treatment (N_2-500°C-10h-3mbar) has successfully healed cracks (formed by 10 kgf indentation) in bulk 3YSZ. The repair mechanism involves the bombardment of the sample surface by charged particles (N ions and free electrons) during plasma treatment. This bombardment is accompanied by high-energy values (from the kinetic energy of charged particles), transferring this energy to the sample surface upon collision, thereby inducing stress elevation around cracks in zirconia, leading to the transformation from tetragonal to monoclinic phase. Furthermore, plasma bombardment results in elevated surface temperatures (with target regions far exceeding others within the plasma furnace), providing a temperature basis for zirconia phase transformation.

Additionally, due to the density inconsistency between monoclinic and tetragonal phases, the transition from tetragonal to monoclinic phase is associated with volume expansion, and the crack's region provides space for this expansion. Consequently, newly formed monoclinic phases predominantly occur along the indentation and crack. This phenomenon is evident from Figure 6-2, where the crack repair process accompanies the contraction of the entire indentation. The bending of each edge of the indentation occurs due to the regional expansion caused by the newly generated monoclinic phase, similar to the reason for crack healing. The size of the indentation is much larger than micro-cracks, making the healing trend observable but macroscopically invisible. This fact is well demonstrated in the results of Raman surface scanning of the 5 kgf indentation (Figure 6-5d). However, no sufficient monoclinic signal was observed along the crack (20 kgf) during Raman scanning as shown in Figure 6-5f, possibly because the crack had closed, and newly formed monoclinic phases were believed to generate perpendicular to the crack. Furthermore,

considering the effective depth of Raman scanning to be approximately 3-5nm, much smaller than the longitudinal depth of the crack (approximately 100um), therefore, no M-phase precipitation was observed on or near the surface in the scanning of cracks formed by 20 kgf.

The focus of this project lies in the positive significance of plasma-induced M-phase generation within the indentation regions concerning the repairing of large-scale cracks. It is noteworthy that not all cracks formed under varies load are fully healed (cracks with loads exceeding 20 kgf are just not partially repaired). The term "crack healing" mentioned in the project refers more to describing a trend of reduction in crack dimensions (width, length, and depth) for those cracks that have not been completely healed, rather than stating that the cracks have been repaired at a physical scale.

It can be observed from Figure 6-3 that the repair limit of plasma treatment (N2-500°C-10h) for indentations is approximately below 10 kgf, as cracks formed under 5 kgf and 10 kgf loads are more likely fully repaired at the bottom, making the original cracks invisible under high-resolution microscopy. However, in the images of indentations formed under 20 kgf to 30 kgf, the original length of the cracks and the filled (packed) areas can be faintly seen, which may lead to the reappearance of cracks if regional stress is reintroduced to the original cracks. Similarly, this viewpoint is further illustrated in the cross-sectional images of cracks in Figure 6-4, where the reduction in crack size (width and depth) can be observed from the bottom and middle milling of the cracks, indicating a trend of crack repair. However, as shown in Figure 6-4c2, the longitudinal repair of cracks always starts from the bulk, and surface repair only occurs after the interior region of the sample is fully filled with M-phase. Although plasma-induced M-phase strengthening in crack repair presents some size limitations

compared to traditional methods, it still provides resultful inspiration and groundwork for the ceramic cracks-healing study in the future.

The underlying phenomena leading to the increase in both hardness and fracture toughness of zirconia following plasma treatment is difficult to ascertain, but may be related to several contributing factors. Firstly, the bombardment of cations onto the sample surface within the plasma environment appears to trigger a transformation of zirconia from its tetragonal phase to monoclinic phase without the need for cracks or deformation. This transformation can introduce residual stresses into the material, which would then increase its resistance to further deformation. Consequently, when external loads are applied, these residual stresses can act is two main ways: (1) the residual stresses they introduce may partially counteract any new external stresses, and (2) the pre-transformed monoclinic crystals may act as nucleation sites for further and more extensive formation of the monoclinic phase. This phenomenon would then reduce surface deformation and help to mitigate the likelihood of plastic deformation, thus contributing to an increase in surface hardness. Furthermore, the presence of abundant oxygen vacancies in black zirconia also seems to play a role. These vacancies influence the crystal structure, potentially introducing further distortion into the lattice. It's plausible that residual stresses arise from this distortion as well, contributing to the observed mechanical changes. However, given the speculative nature of these hypotheses, there is a need for future dedicated and in-depth systematic investigations of the phenomena to explore the underlying mechanisms.

Unlike traditional repair methods involving the addition of healing agents, plasma repair belongs to the category of inducing zirconia self-healing. In previous crack-healing studies, crack repair mainly relied on the diffusion of oxygen healing agents into the ceramic matrix at high temperatures to achieve expansion, whereas plasma

acts only as an inducing factor, effectively accelerating the crack closure and repair process, and successfully achieving crack repair without any healing agents. In addition, compared to spark plasma sintering, DC/AC electric current for zirconia crack repair, plasma treatment requires lower temperature conditions, has a larger repair scale (ten times that reported in literature on current repair of zirconia micro-cracks), and has a wider adjustable range, undoubtedly representing a breakthrough in technological advancement.

This study provides a new approach for inducing zirconia crack self-repair, laying the foundation for research on plasma-modified zirconia and offering new ideas for research in the field of ceramic crack repair.

6.5 Conclusion

In this study, we investigated the feasibility of plasma surface defect-engineering for the crack-healing phenomena in zirconia. The results indicate:

- Plasma treatment (500 °C at 300 Pa for 10 h in 100% N_2) can partially heal the cracks formed on zirconia under a 20 kgf load. This repair originates not only from the surface but also extends to the interior of the material.
- Clear evidence from XRD and Raman surface scans shows the presence of significantly increased monoclinic phases in the healed samples, primarily distributed around cracks and indentations.
- Plasma treatment is found to induce a partial transformation of tetragonal phases to monoclinic phases in zirconia. Due to the density difference, this phase transformation leads to local volume expansion, which allows for the closing and healing of cracks.
- During the plasma treatment, an apparent enhancement in both surface and near-surface hardness and fracture toughness is observed.

Chapter 7 General Discussion

As discussed, the key focus and major achievement of this research lie in the successful blackening (reduction) of commercially available bulk 3YSZ zirconia (3YSZ) with oxygen deficiency by innovative low pressure plasma defect engineering. According to the themes, the research activities and outcomes of this research are reported separately in Chapters 4, 5 and 6 for the sake of clarity and for the ease of understanding. This chapter is directed at synthesising these three themes to provide a wider picture of this research work for a better understanding of the thesis.

7.1 Plasma defect engineering induced oxygen-deficient zirconia (ZrO_{2-a})

As discussed in Chapter 2.3.2, oxygen-deficient zirconia (ZrO_{2-a}) has great application potential in areas such as photocatalysis for water splitting and pollution degradation, light absorption for solar energy harvesting, and photothermal/sonodynamic cancer therapy [7, 10, 14]. Despite the attractive properties, the challenges to efficiently produce oxygen vacancies in zirconia are related to the high Zr-O bond dissociation energy and high bulk vacancy formation energies [13].

As summarised in Section 2.3.2.3, notwithstanding the fact that significant efforts have been devoted to developing routes for synthesising ZrO_{2-a} to reduce its bandgap and improve its photo-responsibility, these approaches exhibit various limitations. The precursors are predominantly particles or powders and demanding processing conditions are required such as high pressures and temperatures or the use of strong reducing agents (e.g., acids). The sintering of these particular ZrO_{2-a} materials into bulk will lead to re-oxidation and thus loss of the attractive properties of ZrO_{2-a}. High-temperature electrochemical reduction is promising for reducing ZrO_2 sheets; however,

existing electrochemical reduction routes pose challenges for the homogeneous treatment of components with complex geometries (non-uniform potential difference).

A breakthrough has been made in this research to efficiently produce bulk ZrO_{2-a} by plasma defect engineering employing environmentally friendly and energy efficient low-pressure DC plasma (Chapter 4/Paper I). Comprehensive characterisation has been conducted: EPR analysis (Figure 4-4) revealed the presence of Zr^{3+} cations and the formation of diamagnetic F^{2+} ($V_O^{\cdot\cdot}$) centres in plasma treated zirconia; XPS analysis (Figure 4-5 & Figure 4-6) demonstrated significantly increased concentrations of oxygen vacancies and reduced zirconium ions (Zr^{3+}) in plasma treated zirconia. The increase of oxygen vacancies is also supported by TGA and DSC measurements (Figure 4-7). The pioneer research has demonstrated for the first time that it is feasible to convert bulk white YSZ zirconia into black oxygen deficient ZrO_{2-a} by plasma defect engineering due to the reduction and significant increase of oxygen vacancies.

7.2 Conditions and Mechanism for the Formation of Bulk ZrO_{2-a}

The research reported in Chapter 4 (Paper I) has revealed that as for the blackening of zirconia powders, the significant increase in oxygen vacancies is the primary cause for the blackening of bulk 3YZ zirconia. However, it is noteworthy that the reduction processes of bulk zirconia and the mechanism involved should differ from that for powdered zirconia, whether placed in a reducing atmosphere or reacted with a reducing agent, the total contact surface area between zirconia powders with many surface active sites (as mentioned in Section 5.4.3) and the reducing agent is very large so that powdered zirconia materials are prone to undergo reduction reactions thus exhibiting high reaction efficiency. However, the above mechanism is not applicable to bulk zirconia. In the reaction process of bulk samples, it is necessary to

consider the conditions required for the initial generation of an oxygen vacancy, whether, under these conditions, the oxygen vacancy has an effective propagation rate, and how oxygen vacancies are transmitted in bulk zirconia materials, which formed the theme of Chapter 5/Paper II.

To this end, systematic investigations of different plasma technologies (DC, active-screen plasma) (Figure 5-1), treatment configurations (contact conditions, cathode material, and cathode potential) (Figure 5-4, Figure 5-3, Figure 5-2 and Figure 5-5), and treatment parameters (voltage, temperature, duration) have been conducted to elucidate the conditions for plasma blackening, uncover the crucial variables that influence the rate of the reduction process, and establish a unique mechanism for the bulk transformation of zirconia.

For instance, as shown in Figure 5-7, when treated at 100 °C the sample did not meet the initial conditions to generate the active sites for forming oxygen vacancies, and even with an increased reaction time of 5 hours, no black colouration was observed. At 200 °C, noticeable blackening occurred at the bottom of the sample, indicating that this temperature condition met the requirements for oxygen vacancy generation, but the generation and transmission rate of oxygen vacancies in the bulk were limited. This resulted in only partial blackening (only going halfway through the 3mm thick sample after 5 hours of treatment). When the temperature was increased to 300 °C, although the black colouration in the sample was not entirely uniform, it essentially covered the entire sample. The difference in longitudinal cross-sectional images between 30 minutes and 5 hours was limited (not as much as the 200 °C treatments), suggesting that 300 °C satisfies both the initial formation of oxygen vacancies and provides adequate internal kinetic energy for their bulk transmission (migration). In comparison to electrical current methods (e.g., electrochemical reduction) that often

involve high temperatures and/or high pressure conditions, as discussed in Section 2.3.2.3, plasma treatment presents profound advantages over electrical current methods for the formation of bulk ZrO_{2-a}.

Although the bulk ZrO_{2-a} was successfully produced through plasma defect engineering, the transformation mechanism still required further study. Firstly, the most crucial comparison was made between the applicability of AS and DC plasma technologies for plasma defect engineering of zirconia (Figure 5-6). Samples under AS conditions did not undergo blackening, and this could be understood by the lack of direct plasma bombardment of the samples and insufficient cathode bias. It was demonstrated that the blackening could not be achieved solely through heating by thermal radiation. Subsequently, cross-sectional images of samples treated at different temperatures and times demonstrated that the initiation of the black colour transformation started from the bottom of the samples in contact with the worktable (cathode), and progressed vertically upwards. This observation was quite key, as the diffusion direction of transformation was not aligned with the typical nitrogen diffusion direction observed during plasma nitriding treatments (an important application of plasma, details can be found in Figure 5-12). By reversing the cathode connection, it was possible to confirm that the diffusion direction of colour change was independent of the plasma bombardment direction or gravity, and instead only relied on the location of contact with the cathode. In other words, the generation of black colour always originates from the surface in direct contact with the cathode, spreading towards the other surfaces, regardless of other experimental conditions. Further evidence was provided through a comparison of cross-sectional images of samples treated with bases containing blind holes and conventional bases (Figure 5-10). Combining these findings with previously published articles on the current-induced blackening of oxygen

vacancies, a mechanism for the plasma generation of oxygen vacancies defects in zirconia was formed (Section 5.4). The outcomes from the above designed experiments have laid a solid basis for establishing the theoretical models and hence advancing scientific understanding of the mechanisms involved (Figure 5-14 to Figure 5-18). The reduction (blackening) of bulk 3YZ zirconia by low pressure plasma defect engineering is achieved through the opposing net migrations of lattice oxygen (O^{2-}) and oxygen vacancies ($V_O^{\cdot\cdot}$) towards the anode-facing and cathode-facing surfaces, respectively.

7.3 Property Improvement and Crack Healing

As demonstrated in Chapter 4 (Paper I), the plasma defect engineered black oxygen deficient zirconia exhibited a significant increase in light absorption across the entire sunlight spectrum (200-3000 nm) compared with the untreated white zirconia (Figure 4-8), which is not commonly observed with oxygen-deficient zirconia formed using other approaches. It should be pointed out that the untreated white zirconia only exhibited notable optical absorption capability in the short-wave ultraviolet (UV) visible radiation but natural sunlight is comprised of only 5% UV (300-400 nm) and 43% visible (400-700 nm), with the remaining 52% consisting of the different categories of infrared (700-2500 nm) radiation. Therefore, the sustained absorption across the entire solar spectrum could pave way towards future efficient solar energy harvesting with high yield using the low pressure DC plasma generated oxygen-deficient zirconia developed from this research.

In addition to the enhanced functional properties, as reported in Chapter 6 (Figure 6-6), the hardness increased from 1246HV0.3 for the untreated white zirconia to 1351HV0.3 for the plasma defect engineered black zirconia (Figure 6-6) representing

an increase of 8.4% following the plasma treatment; the indentation fracture toughness is at least maintained or even marginally increased judging the average value. Although the mechanism involved in enhanced mechanical properties is not clear, combined improvement in both hardness and toughness is unique because in most cases increased hardness is at the cost of reduced toughness for most materials. Therefore, it is expected that the abrasive wear and impact wear properties of zirconia could be improved by the plasma defect engineering technology developed from this research because of the combined improvement of hardness and toughness.

As evidenced in Figs 6.2-6.4, low pressure plasma treatment can partially heal the cracks artificially introduced on zirconia by Vickers indentation with a load as high as 20 kgf. This crack healing or repair starts from the surface and then extends to the interior of the material mainly due to plasma treatment induced partial transformation of tetragonal phases to monoclinic phases and the resulting local volume expansion in zirconia. Furthermore, the reduction-reoxidation process developed from this research is entirely reversible and has significant future advantages for crack repair. This implies that complexly shaped 3YSZ parts when cracked can undergo damage-free restoration without the need for grinding into powder and subsequent high-temperature sintering. In contrast to conventional crack healing methods, which rely on thermal expansion or thermal oxidation with healing agents, plasma treatment could offer higher application potential and broader applicability as it does not rely on healing agents. Additionally, plasma treatment with different carrier gases (such as hydrogen) can also yield similar repair effects, thereby offering additional options for further research and application.

7.4 Forward Thinking

The plasma defect engineering technology developed from the present research for converting white zirconia into black oxygen deficient with significantly improved functional and mechanical properties. This research has provided a comprehensive understanding and significant insights into the application of plasma treatment in the surface restoration and modification of zirconia materials, thereby establishing a solid foundation for future research into other metal oxide such as TiO_2.

Meanwhile, the low-pressure plasma treatment also has some limitations, which are worth further investigation by future researchers to achieve technological advancements. For instance, there is inevitably a very thin deposition layer on the surface of ceramic samples after the plasma treatment, which needs to be removed before various characterisations/applications of the samples can be performed. Removal steps include gentle polishing (as mentioned in Section 6.2.1 and Section 6.3.1) or the ultrasonic cleaning. Additionally, while the low-pressure environment is favourable for plasma generation (as mentioned in the section 2.4.2), but it cannot perform continuous processing (replacing samples and re-establishing a low-pressure environment through evacuation is necessary). If future technologies can widely, efficiently, and steadily form plasma at room temperature and atmospheric pressure, it would be a significant breakthrough for ceramic plasma treatment. Furthermore, due to the presence of airflow throughout the plasma treatment, processing powdered samples with low-pressure plasma furnaces becomes almost impossible (because powdered samples are lightweight and are easily carried away by airflow after being bombarded by plasma). Therefore, how to enable low-pressure plasma furnaces to process powdered samples extensively is also worthy of extensive future research.

Chapter 8 Summary & Future work

In the present research, a range of low pressure DC plasma treatments were designed and comprehensive characterisation of the plasma defect engineered oxygen-deficient zirconia, including the structure, optical absorption ability, and mechanical behaviour, has been conducted. The mechanism of zirconia reduction under low-pressure plasma treatment has been thoroughly investigated. Concurrently, the phenomenon and mechanism of low-pressure plasma crack-healing in zirconia are also elucidated. This chapter will provide a summary of the key findings and major contributions of the entire project, as well as propose avenues for future work.

Key Findings and Contributions

A list of the key scientific and potential technological contributions of this research, separated into the three respective studies, is provided below.

Paper I – Oxygen-deficient zirconia, a potential material for light absorption obtained from plasma defect engineering.

- The complete colour transformation of the bulk zirconia (from pure white to metallic black) was found after subjecting the sample to hydrogen plasma treatment at 500 °C for 5 hours, with no new phase formation.
- The confirmation was made through various characterisations (XPS, EPR, TGA) that the black zirconia obtained after plasma treatment is oxygen-deficient zirconia, indicating a significant increase in oxygen vacancy content compared to pristine samples.
- Plasma-treated zirconia exhibits significantly higher light absorption across the entire sunlight spectrum (200-3000 nm) than pristine zirconia.

- Plasma treatment leads to a significant reduction in both the direct and indirect bandgap values of zirconia. The direct bandgap decreases from 4.84 eV to 2.61 eV, while the indirect bandgap decreases from 3.19 eV to 1.45 eV.

Paper II – Conditions and mechanisms of low-pressure plasma blackening.

- DC plasma treatments can efficiently generate bulk oxygen-deficient zirconia (ZrO_{2-a}) with a thickness of 1-3 mm at temperatures ranging from 200 °C to 500 °C for durations spanning 30 minutes to 5 hours.
- The contact conditions with the cathode determine the location and reduction rate of plasma blackening. The onset of blackening in oxygen-deficient zirconia consistently initiates at conditions directly in contact with the cathode and propagates gradually to areas without direct contact.
- Black areas always grow from cathode-facing surfaces towards the anode-facing surfaces, and the migration of oxygen vacancies leads to the hemispherical growth of black regions, which differs from traditional current reduction methods.
- The progression of low-pressure plasma blackening can be significantly enhanced through various methods, such as applying a higher operating voltage, gold coating the sample surface before treatment, creating a hollow cathode condition by enclosing the sample with three stainless steel blocks, and strategically placing additional stainless steel blocks around the sample to improve heating efficiency.

Paper III – Plasma defect engineering-induced crack-healing.

- Plasma treatment (500 °C at 300 Pa for 10 h in 100% N_2) can partially heal the cracks formed on zirconia under a 20 kgf load. This repair originates not only from the surface but also from the interior of the samples.
- Clear evidence from XRD and Raman surface scans shows the presence of significantly increased monoclinic phases in the healed samples, primarily distributed around cracks and indentations.
- Plasma treatment induces a partial phase transformation from tetragonal to monoclinic in zirconia. Due to the density difference, this phase transformation leads to local volume expansion, which is the main reason for crack healing.
- During the crack healing process, an apparent enhancement in both surface and near-surface hardness and fracture toughness is observed, implying that plasma defect engineering can simultaneously strengthen the mechanical properties of the samples during crack healing.

Proposed Future Work

The present project has shown that the oxygen-deficient zirconia (ZrO_{2-a}) can be successfully produced through low-pressure plasma treatments. The significant capability and efficiency of plasma treatments for modifying the electronic band structure and optical properties of fully dense zirconia offer promising prospects for scalable, cost-efficient, rapid, and environmentally friendly production of n-type semiconducting zirconia. Therefore, the following future work is proposed.

Expansion of plasma defect-engineering to other ceramic materials

Zirconia is just one critical material among many outstanding ceramic materials of interest, and therefore, extending the findings of this research towards other crucial ceramic materials is valuable. The low-pressure plasma defect engineering of zirconia

can serve as an model for future modification of other important ceramic materials with similar structures to zirconia, such as titania (TiO_2) and silica (SiO_2), with the aim to modify their structure and enhance their properties and performance.

Using titania as an example, it has a much narrower bandgap compared to zirconia. Currently, there are studies focusing on the synthesis of black titania (oxygen-deficient titania) for photocatalytic generation of hydrogen, the structure of which is similar to oxygen-deficient zirconia, where the introduction of oxygen vacancies creates new energy levels and reduces the bandgap.

The integration of plasma defect engineering with titania holds great potential. However, a significant challenge lies in the fact that commercially available titania is mostly in the form of powder, which adds complexity to the plasma treatment approach. There are two main thoughts to address this issue. Firstly, the powder form of titania can be sintered into bulk samples in a minimally destructive manner whenever possible (i.e., without altering its basic properties or introducing new defects), followed by plasma treatment.

Secondly, the plasma treatment process can be optimised to effectively treat powder samples. For instance, employing a blind-hole stainless steel block with a metal lid placed over the powder sample while simultaneously reducing the airflow within the furnace; the blind-hole stainless steel block can be bonded to the ceramic substrate as a whole part to hold the powder form titania during the treatment.

Investigate the mechanism underlying the combined enhancement of surface hardness and fracture toughness of oxygen-deficient zirconia

This project has demonstrated that oxygen-deficient zirconia exhibits higher surface hardness and indentation-based fracture toughness compared to untreated zirconia.

However, the exact cause of this phenomenon remains unclear based on the current research findings, highlighting the need for further systematic investigation. As previously mentioned, plasma defect-engineering holds significant implications for the modification of various ceramic materials. Unlike traditional carburising or nitriding treatments of metallic materials, the enhancement of mechanical properties of zirconia are not related to the diffusion of interstitial elements or to the precipitation of hard structures (e.g., nitrides and carbides). Therefore, to reveal the mechanism of action, it is necessary comprehensive investigations to be carried out on the origin of the increased toughness and hardness of zirconia.

Future research on plasma defect engineering to improve the surface hardness and fracture toughness of zirconia can be broadly categorised into three directions. Firstly, systematic experiments are needed to fully characterise the mechanical properties of zirconia samples after plasma treatment under different conditions (temperature, gas composition, pressure, duration, and contact conditions). Secondly, considering the differences between by the anode-facing and cathode-facing surfaces of plasma-treated zirconia (as mentioned in Section 5.4), it is also important to explore the mechanical property differences of both surface during the initial formation and later development of the reduced structured, as well as, the performance within the bulk of the material. Thirdly, to employ microscopy characterisation techniques such as high-resolution transmission electron microscopy (HR-TEM) and Focus Ion Beam (FIB) slicing and view to observe the phase transition distribution (from tetragonal to monoclinic) following plasma treatment. This can reveal the state of the pre-transformed monoclinic phase and form the basis for later practical and theoretical investigations (e.g., finite element analysis of the mechanical behaviour of zirconia

with both monoclinic and tetragonal phase) on the mechanism behind the increased toughness and hardness of plasma treated zirconia.

Characterisations of photocatalytic property and photocatalysis-related applications of bulk oxygen-deficient zirconia

This project has demonstrated the feasibility of preparing bulk 3YSZ with oxygen vacancies using low-pressure plasma and has suggested that bulk zirconia exhibits both direct and indirect band gap reductions compared to pristine samples, as discussed in section 4.3.3. This implies that the bulk zirconia synthesised by this method has potential for enhanced photocatalytic activity. However, there is still a lack of extensive exploration into the photocatalytic performance and specific applications of bulk oxygen-deficient zirconia, which warrants targeted future research.

Future studies should consider that bulk zirconia, when used as a photocatalysis, has a smaller surface area in contact with water (or the environment) compared to powdered samples, which could significantly impact the active sites for chemical reactions. Key considerations for testing and application include methods such as assembling more bulk zirconia samples into black zirconia plates (similar to solar panels) or allowing the zirconia to rotate slowly around an axis in water (or the environment) to ensure sufficient effective surface area for light exposure.

References

[1] Saridag, S., Tak, O. and Alniacik, G. (2013) Basic properties and types of zirconia: An overview. **World Journal of Stomatology**; 2(3): 40-47.

[2] Subbarao, E. (1981) Zirconia-an overview. **Advances in ceramics**; 1: 1-24.

[3] Piconi, C. and Maccauro, G. (1999) Zirconia as a ceramic biomaterial. **Biomaterials**; 20(1): 1-25.

[4] Garvie, R.C. and Nicholson, P.S. (1972) Structure and thermomechanical properties of partially stabilized zirconia in the CaO-ZrO2 system. **Journal of the American Ceramic Society**; 55(3): 152-157.

[5] Kelly, J.R. and Denry, I. (2008) Stabilized zirconia as a structural ceramic: an overview. **Dental materials**; 24(3): 289-298.

[6] Foschini, C., Filho, O.T., Juiz, S., Souza, A., Oliveira, J., Longo, E., Leite, E., Paskocimas, C. and Varela, J.A. (2004) On the stabilizing behavior of zirconia: A Combined experimental and theoretical study. **Journal of materials science**; 39: 1935-1941.

[7] Sun, L., Jiao, X., Liu, W., Wang, Y., Cao, Y., Bao, S.-J., Xu, Z., Kang, Y. and Xue, P. (2019) Novel Oxygen-Deficient Zirconia (ZrO2–x) for Fluorescence/Photoacoustic Imaging-Guided Photothermal/Photodynamic Therapy for Cancer. **ACS applied materials & interfaces**; 11(44): 41127-41139.

[8] Imparato, C., Fantauzzi, M., Passiu, C., Rea, I., Ricca, C., Aschauer, U., Sannino, F., D'Errico, G., De Stefano, L. and Rossi, A. (2019) Unraveling the charge state of oxygen vacancies in ZrO2–x on the basis of synergistic computational and experimental evidence. **The Journal of Physical Chemistry C**; 123(18): 11581-11590.

[9] Jiao, X., Sun, L., Zhang, W., Ren, J., Zhang, L., Cao, Y., Xu, Z., Kang, Y. and Xue, P. (2021) Engineering oxygen-deficient ZrO2-x nanoplatform as therapy-activated "immunogenic cell death (ICD)" inducer to synergize photothermal-augmented sonodynamic tumor elimination in NIR-II biological window. **Biomaterials**; 272: 120787.

[10] Kim, Y.J., Kim, G.-Y., Kim, H.-S., Kim, S., Kim, B., Choi, Y.J., Kim, J., Kim, J. and Ryu, W.-H. (2022) Highly conductive ZrO2–x spheres as bifunctional framework stabilizers and gas evolution relievers in nickel-rich layered cathodes for lithium-ion batteries. **Composites Part B: Engineering**; 238: 109911.

[11] Solakidou, M. (2022) Control of monomeric Vo's versus Vo clusters in ZrO2− x for solar-light H2 production from H2 O at high-yield (millimoles gr− h−). **Scientific Reports**; 12: 15132.

[12] Dashtbozorg, B., Shi, F., Tagliaferro, A., Abela, S., Falticeanu, L. and Dong, H. (2024) Plasma defect-engineering of bulk oxygen-deficient zirconia. **Acta Materialia**; 262: 119457.

[13] Sinhamahapatra, A., Jeon, J.-P., Kang, J., Han, B. and Yu, J.-S. (2016) Oxygen-deficient zirconia (ZrO2− x): a new material for solar light absorption. **Scientific reports**; 6(1): 27218.

[14] Wang, Q., Edalati, K., Koganemaru, Y., Nakamura, S., Watanabe, M., Ishihara, T. and Horita, Z. (2020) Photocatalytic hydrogen generation on low-bandgap black zirconia (ZrO 2) produced by high-pressure torsion. **Journal of Materials Chemistry A**; 8(7): 3643-3650.

[15] Qi, F., Yang, Z., Zhang, J., Wang, Y., Qiu, Q. and Li, H. (2020) Interfacial reaction-induced defect engineering: Enhanced visible and near-infrared absorption of wide band gap metal oxides with abundant oxygen vacancies. **ACS Applied Materials & Interfaces**; 12(49): 55417-55425.
[16] Hassan, N. and Jalil, A. (2022) A review on self-modification of zirconium dioxide nanocatalysts with enhanced visible-light-driven photodegradation of organic pollutants. **Journal of Hazardous Materials**; 423: 126996.
[17] Zu, D., Wang, H., Yang, T., Wei, H., Sun, S. and Wu, H. (2020) Black ZrO2 synthesized by molten lithium reduction strategy for photocatalytic hydrogen generation. **Journal of the American Ceramic Society**; 103(8): 4035-4042.
[18] Shi, F., Dashtbozorg, B., Li, X. and Dong, H. (2024) Processing conditions and mechanisms for the plasma defect-engineering of bulk oxygen-deficient zirconia. **Journal of Materials Research and Technology**.
[19] Ram Mohan Rao, K., Trinadh, K. and Nouveau, C. (2019) Glow discharge plasma nitriding of low alloy steel. **Mater Today Proc**; 19: 864-866.
[20] Wang, J., Xiong, J., Peng, Q., Fan, H., Wang, Y., Li, G. and Shen, B. (2009) Effects of DC plasma nitriding parameters on microstructure and properties of 304L stainless steel. **Mater Charact**; 60(3): 197-203.
[21] Li, G.-j., Peng, Q., Li, C., Wang, Y., Gao, J., Chen, S.-y., Wang, J. and Shen, B.-l. (2008) Effect of DC plasma nitriding temperature on microstructure and dry-sliding wear properties of 316L stainless steel. **Surf Coat Technol**; 202(12): 2749-2754.
[22] Dashtbozorg, B., Tao, X. and Dong, H. (2022) Active-screen plasma surface multi-functionalisation of biopolymers and carbon-based materials–An overview. **Surf Coat Technol**; 442: 128188.
[23] Yang, N.-n., Shen, P., Yang, B., Guo, R.-f. and Jiang, Q.-c. (2016) Significant improvement in the wettability of ZrO_2 by molten Al under the application of a direct current. **Mater Des**; 111: 158-163.
[24] Masó, N. and West, A.R. (2015) Electronic Conductivity in Yttria-Stabilized Zirconia under a Small *dc* Bias. **Chem Mater**; 27(5): 1552-1558.
[25] Manicone, P.F., Iommetti, P.R. and Raffaelli, L. (2007) An overview of zirconia ceramics: basic properties and clinical applications. **Journal of dentistry**; 35(11): 819-826.
[26] Madfa, A.A., Al-Sanabani, F.A., Al-Qudami, N.H., Al-Sanabani, J.S. and Amran, A.G. (2014) Use of zirconia in dentistry: An overview. **The Open Biomaterials Journal**; 5(1).
[27] Pradeep, C., Gupta, S. and Sisodia, S. (2020) ZIRCONIA IN DENTISTRY; AN OVERVIEW. **Guident**; 13(10).
[28] Rao, M., Raju, M., Sajjan, M. and Raju, A. (2015) An Overview on Zirconia. **TPDI**; 6(2): 32-36.
[29] AN, R., Gupta, R. and Weber, D. (2018) Zirconia Biomaterials.
[30] Li, Y., Wang, S., Wang, M., Zhang, X., Lu, B., Wang, Y., Dong, D., He, F., Liu, W. and Wu, S. (2021) Three-dimensional printing of blue-colored zirconia accessories using digital light processing-based stereolithography. **Journal of Asian Ceramic Societies**; 9(2): 727-732.
[31] Carlier, G. and Lorand, J.-P. (2008) Zr-rich accessory minerals (titanite, perrierite, zirconolite, baddeleyite) record strong oxidation associated with magma mixing in the south Peruvian potassic province. **Lithos**; 104(1-4): 54-70.

[32] Seifert, W. and Kramer, W. (2003) Accessory titanite: an important carrier of zirconium in lamprophyres. **Lithos**; 71(1): 81-98.
[33] Goff, J., Hayes, W., Hull, S., Hutchings, M. and Clausen, K.N. (1999) Defect structure of yttria-stabilized zirconia and its influence on the ionic conductivity at elevated temperatures. **Physical Review B**; 59(22): 14202.
[34] Rondão, A., Muccillo, E., Muccillo, R. and Marques, F. (2017) On the electrochemical properties of Mg-PSZ: an overview. **Journal of Applied Electrochemistry**; 47: 1091-1113.
[35] Pilathadka, S., Vahalová, D. and Vosáhlo, T. (2007) The Zirconia: a new dental ceramic material. An overview. **Prague Med Rep**; 108(1): 5-12.
[36] Denry, I. and Kelly, J.R. (2008) State of the art of zirconia for dental applications. **Dental materials**; 24(3): 299-307.
[37] Asharaf, S., Karthigeyan, A.S., Deivanai, M. and Mani, R. (2014) Zirconia: properties and application" a review. **Pakistan Oral & Dental Journal**; 34(1).
[38] Zhang, Y. and Lawn, B.R. (2018) Novel zirconia materials in dentistry. **Journal of dental research**; 97(2): 140-147.
[39] Butler, E. (1985) Transformation-toughened zirconia ceramics. **Materials Science and Technology**; 1(6): 417-432.
[40] Claussen, N. and Heuer, A. (1991) Transformation toughening. In: **Concise Encyclopedia of Advanced Ceramic Materials**. Elsevier. p 494-497.
[41] Chevalier, J., Gremillard, L., Virkar, A.V. and Clarke, D.R. (2009) The tetragonal-monoclinic transformation in zirconia: lessons learned and future trends. **Journal of the american ceramic society**; 92(9): 1901-1920.
[42] Rose, L. (1987) The mechanics of transformation toughening. **Proceedings of the Royal Society of London A Mathematical and Physical Sciences**; 412(1842): 169-197.
[43] Basu, B. (2005) Toughening of yttria-stabilised tetragonal zirconia ceramics. **International Materials Reviews**; 50(4): 239-256.
[44] Green, D.J. (2018) **Transformation toughening of ceramics**. CRC press.
[45] Hannink, R. and Swain, M. (1994) Progress in transformation toughening of ceramics. **Annual Review of Materials Science**; 24(1): 359-408.
[46] Chen, X., Liu, L. and Huang, F. (2015) Black titanium dioxide (TiO 2) nanomaterials. **Chemical Society Reviews**; 44(7): 1861-1885.
[47] Chen, X., Liu, L., Yu, P.Y. and Mao, S.S. (2011) Increasing solar absorption for photocatalysis with black hydrogenated titanium dioxide nanocrystals. **Science**; 331(6018): 746-750.
[48] Naldoni, A., Allieta, M., Santangelo, S., Marelli, M., Fabbri, F., Cappelli, S., Bianchi, C.L., Psaro, R. and Dal Santo, V. (2012) Effect of nature and location of defects on bandgap narrowing in black TiO2 nanoparticles. **Journal of the American Chemical Society**; 134(18): 7600-7603.
[49] Syzgantseva, O.A., Calatayud, M. and Minot, C. (2012) Revealing the surface reactivity of zirconia by periodic DFT calculations. **The Journal of Physical Chemistry C**; 116(11): 6636-6644.
[50] Morterra, C., Giamello, E., Orio, L. and Volante, M. (1990) Formation and reactivity of zirconium (3+) centers at the surface of vacuum-activated monoclinic zirconia. **Journal of Physical Chemistry**; 94(7): 3111-3116.
[51] Soares, M.R.N. (2016) **Development of zirconia based phosphors for application in lighting and as luminescent bioprobes**: Universidade de Aveiro (Portugal).

[52] Eichler, J., Eisele, U. and Rödel, J. (2004) Mechanical properties of monoclinic zirconia. **Journal of the American Ceramic Society**; 87(7): 1401-1403.
[53] Carter, D.B.W.C.B. (2009) **Transmission Electron Microscopy A Textbook for Materials Science**. springer publication.
[54] Shukla, S. and Seal, S. (2005) Mechanisms of room temperature metastable tetragonal phase stabilisation in zirconia. **International materials reviews**; 50(1): 45.
[55] Peter, Y. and Cardona, M. (2010) **Fundamentals of semiconductors: physics and materials properties**. Springer Science & Business Media.
[56] Shackelford, J.F. and Doremus, R.H. (2008) Ceramic and glass materials. **JF Shackelford, RH Doremus**: 28-329.
[57] Ohtaka, O., Yamanaka, T. and Yagi, T. (1994) New high-pressure and-temperature phase of ZrO 2 above 1000° C at 20 GPa. **Physical Review B**; 49(14): 9295.
[58] Grebenyuk, A., Karaulov, A., Dauknis, V., Prantskyavichyus, G. and Yurenas, V. (1968) Effect of phase composition on the thermal shock resistance of zirconia. **Refractories**; 9(1-2): 44-51.
[59] Weber, B.C. (1958) **Zirconia: Its Crystallographic Polymmorphy and High Temperature Potentials**. Wright Air Development Center, Air Research and Development Command, United ….
[60] Newman, J. (1968) Solid State Electrolysis of Yttria Stablized Zirconia.
[61] Porter, D.L. and Heuer, A. (1977) Mechanisms of toughening partially stabilized zirconia (PSZ). **J Am Ceram Soc;(United States)**; 60.
[62] Messing, G.L., Hirano, S.I. and Gauckler, L. (2006) Ceramic processing science. **Journal of the American Ceramic Society**; 89(6): 1769-1770.
[63] Garvie, R.C., Hannink, R. and Pascoe, R. (1990) Ceramic steel? In: **Sintering Key Papers**. Springer. p 253-257.
[64] Casellas, D., Feder, A., Llanes, L. and Anglada, M. (2001) Fracture toughness and mechanical strength of Y-TZP/PSZ ceramics. **Scripta materialia**; 45(2): 213-220.
[65] Hughan, R.R. and Hannink, R.H. (1986) Precipitation During Controlled Cooling of Magnesia‐Partially‐Stabilized Zirconia. **Journal of the American Ceramic Society**; 69(7): 556-563.
[66] Gupta, T., Bechtold, J., Kuznicki, R., Cadoff, L. and Rossing, B. (1977) Stabilization of tetragonal phase in polycrystalline zirconia. **Journal of Materials Science**; 12: 2421-2426.
[67] Vasanthavel, S. and Kannan, S. (2018) Structural investigations on the tetragonal to cubic phase transformations in zirconia induced by progressive yttrium additions. **Journal of Physics and Chemistry of Solids**; 112: 100-105.
[68] Chevalier, J., Deville, S., Münch, E., Jullian, R. and Lair, F. (2004) Critical effect of cubic phase on aging in 3 mol% yttria-stabilized zirconia ceramics for hip replacement prosthesis. **Biomaterials**; 25(24): 5539-5545.
[69] Chevalier, J. (2006) What future for zirconia as a biomaterial? **Biomaterials**; 27(4): 535-543.
[70] Matsui, K., Horikoshi, H., Ohmichi, N., Ohgai, M., Yoshida, H. and Ikuhara, Y. (2003) Cubic‐formation and grain‐growth mechanisms in tetragonal zirconia polycrystal. **Journal of the American Ceramic Society**; 86(8): 1401-1408.
[71] Ruiz, L. and Readey, M.J. (1996) Effect of heat treatment on grain size, phase assemblage, and mechanical properties of 3 mol% Y‐TZP. **Journal of the American ceramic society**; 79(9): 2331-2340.

[72] Haberko, K. and Pampuch, R. (1983) Influence of yttria content on phase composition and mechanical properties of Y-PSZ. **Ceramics International**; 9(1): 8-12.
[73] Cernuschi, F., Bianchi, P., Leoni, M. and Scardi, P. (1999) Thermal diffusivity/microstructure relationship in Y-PSZ thermal barrier coatings. **Journal of Thermal Spray Technology**; 8: 102-109.
[74] Ghatee, M., Shariat, M. and Irvine, J. (2009) Investigation of electrical and mechanical properties of 3YSZ/8YSZ composite electrolytes. **Solid State Ionics**; 180(1): 57-62.
[75] Cao, Y., Li, C., Ma, Y., Luo, H., Yang, Y. and Guo, H. (2019) Mechanical properties and thermal conductivities of 3YSZ-toughened fully stabilized HfO2 ceramics. **Ceramics International**; 45(10): 12851-12859.
[76] Ingo, G., Paparazzo, E., Bagnarelli, O. and Zacchetti, N. (1990) XPS studies on cerium, zirconium and yttrium valence states in plasma-sprayed coatings. **Surface and Interface Analysis**; 16(1-12): 515-519.
[77] Zhang, Q., Liu, W., He, F., Chen, Y. and Wu, H. (2000) Characteristics of cerium oxide in ternary ZrO2-MgO-CeO2 system. **Journal of materials science letters**; 19: 1093-1094.
[78] Wang, T.Y., Xu, Y.G., Huang, Z.H., Fang, M.H., Liu, Y.G., Wu, X.W., Yin, L., Liu, B.L. and Hu, X.Z. (2014) Influence of CeO2 Additive on the Phase Transformations of Zirconia from Zircon Ore by Carbothermal Reduction Process. **Key Engineering Materials**; 602: 238-241.
[79] Zhao, M., Ren, X. and Pan, W. (2015) Low thermal conductivity of SnO2-doped Y2O3-stabilized ZrO2: effect of the lattice tetragonal distortion. **Journal of the American Ceramic Society**; 98(1): 229-235.
[80] Ding, H., Virkar, A.V. and Liu, F. (2012) Defect configuration and phase stability of cubic versus tetragonal yttria-stabilized zirconia. **Solid State Ionics**; 215: 16-23.
[81] Trice, R., Su, Y.J., Mawdsley, J., Faber, K., De Arellano-Lopez, A., Wang, H. and Porter, W. (2002) Effect of heat treatment on phase stability, microstructure, and thermal conductivity of plasma-sprayed YSZ. **Journal of materials science**; 37: 2359-2365.
[82] Hwang, K.-J., Shin, M., Lee, M.-H., Lee, H., Oh, M.Y. and Shin, T.H. (2019) Investigation on the phase stability of yttria-stabilized zirconia electrolytes for high-temperature electrochemical application. **Ceramics International**; 45(7): 9462-9467.
[83] Chen, D., Luo, F., Zhou, W. and Zhu, D. (2018) Influence of Nb5+, Ti4+, Y3+ and Zn2+ doped Na3Zr2Si2PO12 solid electrolyte on its conductivity. **Journal of Alloys and Compounds**; 757: 348-355.
[84] Ray, J.C., Panda, A.B., Saha, C.R. and Pramanik, P. (2003) Synthesis of Niobium (V)-Stabilized Tetragonal Zirconia Nanocrystalline Powders. **Journal of the American Ceramic Society**; 86(3): 514-516.
[85] Caspers, C., Gloskovskii, A., Drube, W., Schneider, C.M. and Müller, M. (2014) “Conductive” yttria-stabilized zirconia as an epitaxial template for oxide heterostructures. **Journal of Applied Physics**; 115(17).
[86] Žmak, I., Ćorić, D., Mandić, V. and Ćurković, L. (2019) Hardness and indentation fracture toughness of slip cast alumina and alumina-zirconia ceramics. **Materials**; 13(1): 122.

[87] Kelly, P.M. and Rose, L.F. (2002) The martensitic transformation in ceramics—its role in transformation toughening. **Progress in Materials Science**; 47(5): 463-557.
[88] Hannink, R.H., Kelly, P.M. and Muddle, B.C. (2000) Transformation toughening in zirconia-containing ceramics. **Journal of the American Ceramic Society**; 83(3): 461-487.
[89] Ćorić, D., Renjo, M.M. and Ćurković, L. (2017) Vickers indentation fracture toughness of Y-TZP dental ceramics. **International Journal of Refractory Metals and Hard Materials**; 64: 14-19.
[90] Fedorov, P.P. and Yarotskaya, E.G. (2021) Zirconium dioxide. Review. **Конденсированные среды и межфазные границы**; 23(2 (eng)): 170-188.
[91] Römer, H., Luther, K.D. and Assmus, W. (1994) Coloured zirconia. **Crystal Research and Technology**; 29(6): 787-794.
[92] Liu, G., Xie, Z., Wang, W., Wu, Y. and Yang, X. (2011) Fabrication of coloured zirconia ceramics by infiltrating water debound injection moulded green body. **Advances in Applied Ceramics**; 110(1): 58-62.
[93] Dietrich, A., Heimann, R. and Willmann, G. (1996) The colour of medical-grade zirconia (Y-TZP). **Journal of Materials Science: Materials in Medicine**; 7: 559-565.
[94] Agarkov, D., Borik, M., Bredikhin, S., Burmistrov, I., Eliseeva, G., Kolotygin, V., Kulebyakin, A., Kuritsyna, I., Lomonova, E. and Milovich, F. (2019) Structure and transport properties of zirconia crystals co-doped by scandia, ceria and yttria. **Journal of Materiomics**; 5(2): 273-279.
[95] Alaniz, J., Perez-Gutierrez, F., Aguilar, G. and Garay, J. (2009) Optical properties of transparent nanocrystalline yttria stabilized zirconia. **Optical Materials**; 32(1): 62-68.
[96] Zhang, H., Kim, B.-N., Morita, K., Yoshida, H., Lim, J.-H. and Hiraga, K. (2010) Optimization of high-pressure sintering of transparent zirconia with nano-sized grains. **Journal of alloys and compounds**; 508(1): 196-199.
[97] Ogden, J.M. (2021) Green Zircon in Early South-East Asian Jewellery. **The Journal of Gemmology**; 37(8): 775-776.
[98] Forno, I., Priarone, P.C., Settineri, L. and Grande, M.A. (2014) Surface characterization and machinability of zirconium alloys in view of jewelry application. **Advanced Materials Research**; 941: 18-25.
[99] Domagala, R. and McPherson, D. (1954) System zirconium-oxygen. **JOM**; 6: 238-246.
[100] Aronson, S. (1961) Oxidation and equilibrium in nonstoichiometric zirconium dioxide powder. **Journal of The Electrochemical Society**; 108(4): 312.
[101] Fujishima, A. and Honda, K. (1972) Electrochemical photolysis of water at a semiconductor electrode. **nature**; 238(5358): 37-38.
[102] Maeda, K. and Domen, K. (2010) Photocatalytic water splitting: recent progress and future challenges. **The Journal of Physical Chemistry Letters**; 1(18): 2655-2661.
[103] Osterloh, F.E. (2013) Inorganic nanostructures for photoelectrochemical and photocatalytic water splitting. **Chemical Society Reviews**; 42(6): 2294-2320.
[104] Mettenbörger, A., Singh, T., Singh, A.P., Järvi, T.T., Moseler, M., Valldor, M. and Mathur, S. (2014) Plasma-chemical reduction of iron oxide photoanodes for efficient solar hydrogen production. **international journal of hydrogen energy**; 39(10): 4828-4835.

[105] Tan, H., Zhao, Z., Zhu, W.-b., Coker, E.N., Li, B., Zheng, M., Yu, W., Fan, H. and Sun, Z. (2014) Oxygen vacancy enhanced photocatalytic activity of pervoskite SrTiO3. **ACS applied materials & interfaces**; 6(21): 19184-19190.
[106] Tompkins, F.C. (1960) Superficial chemistry and solid imperfections. **Nature**; 186(4718): 3-6.
[107] Liu, G., Wang, T., Ouyang, S., Liu, L., Jiang, H., Yu, Q., Kako, T. and Ye, J. (2015) Band-structure-controlled BiO (ClBr)(1− x)/2 I x solid solutions for visible-light photocatalysis. **Journal of Materials Chemistry A**; 3(15): 8123-8132.
[108] Lou, Y., Ma, J., Cao, X., Wang, L., Dai, Q., Zhao, Z., Cai, Y., Zhan, W., Guo, Y. and Hu, P. (2014) Promoting effects of In2O3 on Co3O4 for CO oxidation: tuning O2 activation and CO adsorption strength simultaneously. **Acs Catalysis**; 4(11): 4143-4152.
[109] Maeda, Y., Iizuka, Y. and Kohyama, M. (2013) Generation of oxygen vacancies at a Au/TiO2 perimeter interface during CO oxidation detected by in situ electrical conductance measurement. **Journal of the American Chemical Society**; 135(2): 906-909.
[110] Pan, C. and Zhu, Y. (2010) New type of BiPO4 oxy-acid salt photocatalyst with high photocatalytic activity on degradation of dye. **Environmental science & technology**; 44(14): 5570-5574.
[111] Cui, H., Zhu, G., Xie, Y., Zhao, W., Yang, C., Lin, T., Gu, H. and Huang, F. (2015) Black nanostructured Nb 2 O 5 with improved solar absorption and enhanced photoelectrochemical water splitting. **Journal of Materials Chemistry A**; 3(22): 11830-11837.
[112] Guo, H.-L., Zhu, Q., Wu, X.-L., Jiang, Y.-F., Xie, X. and Xu, A.-W. (2015) Oxygen deficient ZnO 1− x nanosheets with high visible light photocatalytic activity. **Nanoscale**; 7(16): 7216-7223.
[113] Xia, T., Wallenmeyer, P., Anderson, A., Murowchick, J., Liu, L. and Chen, X. (2014) Hydrogenated black ZnO nanoparticles with enhanced photocatalytic performance. **RSC advances**; 4(78): 41654-41658.
[114] Ye, K., Li, K., Lu, Y., Guo, Z., Ni, N., Liu, H., Huang, Y., Ji, H. and Wang, P. (2019) An overview of advanced methods for the characterization of oxygen vacancies in materials. **TrAC Trends in Analytical Chemistry**; 116: 102-108.
[115] Huang, Y., Li, K., Li, S., Lin, Y., Liu, H. and Tong, Y. (2018) Ultrathin Bi2MoO6 nanosheets for photocatalysis: performance enhancement by atomic interfacial engineering. **ChemistrySelect**; 3(26): 7423-7428.
[116] Punnoose, A. and Seehra, M. (2002) ESR Observation of W5+ and Zr3+ States in Pt/WO x/ZrO2 Catalysts. **Catalysis letters**; 78: 157-160.
[117] Din, L.M.U. and Kumar, V. (2023) Oxygen-deficient low band gap black zirconia nanoparticle synthesis and tailoring its band gap/photoluminescence via silver doping. **Physica B: Condensed Matter**; 652: 414626.
[118] Tolba, S.A. and Allam, N.K. (2019) Computational design of novel hydrogen-doped, oxygen-deficient monoclinic zirconia with excellent optical absorption and electronic properties. **Scientific reports**; 9(1): 10159.
[119] Xia, X. (2010) **Computational modelling study of yttria-stabilized zirconia**: UCL (University College London).
[120] Dong, Y., Huang, Y., Ding, D., Wu, W., Yao, X. and Li, J. (2021) Chemical and structural origin of hole states in yttria-stabilized zirconia. **Acta Materialia**; 203: 116487.

[121] Biesuz, M., Pinter, L., Saunders, T., Reece, M., Binner, J., Sglavo, V.M. and Grasso, S. (2018) Investigation of electrochemical, optical and thermal effects during flash sintering of 8YSZ. **Materials**; 11(7): 1214.
[122] Alvarez, A., Dong, Y. and Chen, I.W. (2020) DC electrical degradation of YSZ: voltage-controlled electrical metallization of a fast ion conducting insulator. **Journal of the American Ceramic Society**; 103(5): 3178-3193.
[123] Dancer, C.E. (2016) Flash sintering of ceramic materials. **Materials Research Express**; 3(10): 102001.
[124] Ren, K., Liu, J. and Wang, Y. (2020) Flash sintering of yttria-stabilized zirconia: Fundamental understanding and applications. **Scripta Materialia**; 187: 371-378.
[125] Cologna, M., Prette, A.L. and Raj, R. (2011) Flash-sintering of cubic yttria-stabilized zirconia at 750° C for possible use in SOFC manufacturing. **Journal of the American Ceramic Society**; 94(2): 316-319.
[126] Jha, S.K., Terauds, K., Lebrun, J.-M. and Raj, R. (2016) Beyond flash sintering in 3 mol% yttria stabilized zirconia. **Journal of the Ceramic Society of Japan**; 124(4): 283-288.
[127] Downs, J.A. (2013) Mechanisms of flash sintering in cubic zirconia.
[128] Biesuz, M. and Sglavo, V.M. (2019) Microstructural temperature gradient-driven diffusion: possible densification mechanism for flash sintering of zirconia? **Ceramics International**; 45(1): 1227-1236.
[129] Qin, W., Majidi, H., Yun, J. and van Benthem, K. (2016) Electrode effects on microstructure formation during flash sintering of yttrium-stabilized zirconia. **Journal of the American Ceramic Society**; 99(7): 2253-2259.
[130] Kirchheim, R. (2019) Incubation time for flash sintering as caused by internal reactions, exemplified for yttria stabilized zirconia. **Acta Materialia**; 175: 361-375.
[131] Zhang, H., Kim, B.-N., Morita, K., Hiraga, H.Y.K. and Sakka, Y. (2011) Effect of sintering temperature on optical properties and microstructure of translucent zirconia prepared by high-pressure spark plasma sintering. **Science and technology of advanced materials**.
[132] Guo, F. and Xiao, P. (2012) Effect of Fe2O3 doping on sintering of yttria-stabilized zirconia. **Journal of the European Ceramic Society**; 32(16): 4157-4164.
[133] Janek, J. and Korte, C. (1999) Electrochemical blackening of yttria-stabilized zirconia–morphological instability of the moving reaction front. **Solid State Ionics**; 116(3-4): 181-195.
[134] Jana, S. and Biswas, P.K. (1997) Characterization of oxygen deficiency and trivalent zirconium in sol-gel derived zirconia films. **Materials Letters**; 30(1): 53-58.
[135] Chen, F.F. (2012) **Introduction to plasma physics**. Springer Science & Business Media.
[136] Conrads, H. and Schmidt, M. (2000) Plasma generation and plasma sources. **Plasma sources science and technology**; 9(4): 441.
[137] Graves, D.B. (1994) Plasma processing. **IEEE transactions on Plasma Science**; 22(1): 31-42.
[138] Boenig, H. (2019) **Plasma science and technology**. Cornell University Press.
[139] Fridman, A. (2008) **Plasma chemistry**. Cambridge university press.

[140] Bellan, P.M. (2008) **Fundamentals of plasma physics**. Cambridge university press.
[141] Liddell, H.G., Scott, R. and Jones, S.H.S. A Greek-English lexicon. Clarendon. Oxford; 1940.
[142] Chu, P.K. and Lu, X. (2013) **Low temperature plasma technology: methods and applications**. CRC press.
[143] Piel, A. (2010) An introduction to laboratory, space, and fusion plasmas. **Plasma Physics**.
[144] Chiuderi, C. and Velli, M. (2015) **Basics of plasma astrophysics**. Springer.
[145] Mishin, E.V. (2019) Artificial aurora experiments and application to natural aurora. **Frontiers in Astronomy and Space Sciences**; 6: 14.
[146] Paschmann, G., Haaland, S., Treumann, R. and Treumann, R.A. (2003) **Auroral plasma physics**. Springer Science & Business Media.
[147] Xu, W., Fang, J. and Lu, Y. (2002) Study on ceramic cutting by plasma arc. **Journal of materials processing technology**; 129(1-3): 152-156.
[148] Tonks, L. and Langmuir, I. (1929) A general theory of the plasma of an arc. **Physical review**; 34(6): 876.
[149] Gerdeman, D.A. and Hecht, N.L. (2012) Arc plasma technology in materials science.
[150] Lieberman, M.A. and Lichtenberg, A.J. (1994) Principles of plasma discharges and materials processing. **MRS Bulletin**; 30(12): 899-901.
[151] Galli, G., Hamrita, H., Jammes, C., Kirkpatrick, M.J., Odic, E., Dessante, P. and Molinié, P. (2019) Paschen's law in extreme pressure and temperature conditions. **IEEE Transactions on Plasma Science**; 47(3): 1641-1647.
[152] Husain, E. and Nema, R. (1982) Analysis of Paschen curves for air, N2 and SF6 using the Townsend breakdown equation. **IEEE transactions on electrical insulation**; (4): 350-353.
[153] Ollegott, K., Wirth, P., Oberste-Beulmann, C., Awakowicz, P. and Muhler, M. (2020) Fundamental properties and applications of dielectric barrier discharges in plasma-catalytic processes at atmospheric pressure. **Chemie Ingenieur Technik**; 92(10): 1542-1558.
[154] Calvert, J. Electrical Discharges-How the spark, glow and arc work. 2005.
[155] Claude, G. System of illuminating by luminescent tubes. Google Patents; 1915.
[156] Durand, F., Szeliski, R., Mohan, A., Choudhury, P., Tumblin, J., McGuire, M., Matusik, W., Pfister, H., Chen, B. and Hughes, J.F. (2007) Theme Articles.
[157] Franz, G. (2009) **Low pressure plasmas and microstructuring technology**. Springer Science & Business Media.
[158] Czerwiec, T., Michel, H. and Bergmann, E. (1998) Low-pressure, high-density plasma nitriding: mechanisms, technology and results. **Surface and Coatings Technology**; 108: 182-190.
[159] Lei, M. and Zhang, Z. (1995) Plasma source ion nitriding: A new low temperature, low-pressure nitriding approach. **Journal of Vacuum Science & Technology A: Vacuum, Surfaces, and Films**; 13(6): 2986-2990.
[160] Korhonen, A. and Sirvio, E. (1982) A new low pressure plasma nitriding method. **Thin Solid Films**; 96(1): 103-108.
[161] Ehiasarian, A. and Hovsepian, P.E. (2024) Novel high-efficiency plasma nitriding process utilizing a high power impulse magnetron sputtering discharge. **Journal of Vacuum Science & Technology A**; 42(2).
[162] Czerwinski, F. (2012) Thermochemical treatment of metals. **Heat Treatment–Conventional and Novel Applications**; 5: 73-112.

[163] Chiad, B.T., Al-Zubaydi, T., Khalaf, M. and Khudiar, A. (2009) Construction and characterization of a low pressure plasma reactor using DC glow discharge. **Journal of Optoelectronics and Biomedical Materials**; 1(3): 255-262.
[164] Liang, W., Juncai, S. and Xiaolei, X. (2001) Low pressure plasma arc source ion nitriding compared with glow-discharge plasma nitriding of stainless steel. **Surface and Coatings Technology**; 145(1-3): 31-37.
[165] Mehta, V. and Rohit, M. (2005) **Principles of Electronics (Multicolour Edition)**. S. Chand Publishing.
[166] Fridman, A. and Kennedy, L.A. (2004) **Plasma physics and engineering**. CRC press.
[167] Reece Roth, J. (2001) Industrial plasma engineering.
[168] Konjevic, N., Videnovic, I. and Kuraica, M. (1997) Emission spectroscopy of the cathode fall region of an analytical glow discharge. **Le Journal de Physique IV**; 7(C4): C4-247-C244-258.
[169] Tahiyat, M.M., Stephens, J.C., Kolobov, V.I. and Farouk, T.I. (2021) Striations in moderate pressure dc driven nitrogen glow discharge. **Journal of Physics D: Applied Physics**; 55(8): 085201.
[170] Benilov, M. (2008) Understanding and modelling plasma–electrode interaction in high-pressure arc discharges: a review. **Journal of Physics D: Applied Physics**; 41(14): 144001.
[171] Vintizenko, L., Grigoriev, S., Koval, N., Tolkachev, V., Lopatin, I. and Schanin, P. (2001) Hollow-cathode low-pressure arc discharges and their application in plasma generators and charged-particle sources. **Russian physics journal**; 44(9): 927-936.
[172] Mavrodineanu, R. (1984) Hollow cathode discharges: Analytical applications. **JOURNAL OF RESEARCH of the National Bureau of Standards**; 89(2): 143.
[173] Moran, S.L. (1979) High repetition rate LC oscillator. **IEEE Transactions on Electron Devices**; 26(10): 1524-1527.
[174] Korolev, Y.D. and Koval, N. (2018) Low-pressure discharges with hollow cathode and hollow anode and their applications. **Journal of Physics D: Applied Physics**; 51(32): 323001.
[175] Liu, H., Che, H., Li, G. and Lei, M. (2021) Low-pressure hollow cathode plasma source carburizing technique at low temperature. **Surface and Coatings Technology**; 422: 127511.
[176] Liu, H., Che, H., Gao, J., Li, G. and Lei, M. (2022) Low-pressure hollow cathode plasma source carburizing of AISI 304L austenitic stainless steel at low temperature. **Surface and Coatings Technology**; 442: 128548.
[177] Dashtbozorg, B. (2021) **Development of durable antibacterial stainless steel surfaces through plasma nitriding and ultrashort pulsed laser texturing** [PhD]. Birmingham, UK: University of Birmingham.
[178] Barankova, H. and Bárdoš, L. (2001) Hollow cathode plasma sources for large area surface treatment. **Surface and Coatings Technology**; 146: 486-490.
[179] Fietzke, F. and Zimmermann, B. (2010) Plasma characterization and technological application of a hollow cathode plasma source with an axial magnetic field. **Surface and Coatings Technology**; 205(5): 1491-1496.
[180] Barankova, H. and Bárdoš, L. (2003) Hollow cathode atmospheric pressure plasma sources for surface treatment. **Surface and Coatings Technology**; 174: 63-67.

[181] Nishimoto, A., Nagatsuka, K., Narita, R., Nii, H. and Akamatsu, K. (2010) Effect of the distance between screen and sample on active screen plasma nitriding properties. **Surface and Coatings Technology**; 205: S365-S368.
[182] Lin, K., Li, X., Sun, Y., Luo, X. and Dong, H. (2014) Active screen plasma nitriding of 316 stainless steel for the application of bipolar plates in proton exchange membrane fuel cells. **Int J Hydrog Energy**; 39(36): 21470-21479.
[183] Li, C., Bell, T. and Dong, H. (2002) A study of active screen plasma nitriding. **Surface Engineering**; 18(3): 174-181.
[184] Gallo, S.C. and Dong, H. (2009) On the fundamental mechanisms of active screen plasma nitriding. **Vacuum**; 84(2): 321-325.
[185] Biró, A.S. (2014) Active Screen Plasma Nitriding State of the Art. **Production Processes and Systems**; 7(1): 103-114.
[186] Zhao, C., Li, C., Dong, H. and Bell, T. (2006) Study on the active screen plasma nitriding and its nitriding mechanism. **Surface and Coatings Technology**; 201(6): 2320-2325.
[187] Li, C. and Bell, T. (2004) Corrosion properties of active screen plasma nitrided 316 austenitic stainless steel. **Corrosion Science**; 46(6): 1527-1547.
[188] Huang, Y.-T., Kavanagh, S.R., Scanlon, D.O., Walsh, A. and Hoye, R.L.Z. (2021) Perovskite-inspired materials for photovoltaics and beyond—from design to devices. **Nanotechnology**; 32(13): 132004.
[189] Fakharuddin, A., Jose, R., Brown, T.M., Fabregat-Santiago, F. and Bisquert, J. (2014) A perspective on the production of dye-sensitized solar modules. **Energy Environ Sci**; 7(12): 3952-3981.
[190] Bartkowiak, A., Korolevych, O., Chiarello, G.L., Makowska-Janusik, M. and Zalas, M. (2021) How can the introduction of Zr^{4+} ions into TiO_2 nanomaterial impact the DSSC photoconversion efficiency? A comprehensive theoretical and experimental consideration. **Mater**; 14(11): 2955.
[191] Chen, X., Shen, S., Guo, L. and Mao, S.S. (2010) Semiconductor-based photocatalytic hydrogen generation. **Chem Rev**; 110(11): 6503-6570.
[192] Reddy, C.V., Reddy, K.R., Harish, V.V.N., Shim, J., Shankar, M.V., Shetti, N.P. and Aminabhavi, T.M. (2020) Metal-organic frameworks (MOFs)-based efficient heterogeneous photocatalysts: Synthesis, properties and its applications in photocatalytic hydrogen generation, CO_2 reduction and photodegradation of organic dyes. **Int J Hydrog Energy**; 45(13): 7656-7679.
[193] Emeline, A., Kataeva, G.V., Litke, A.S., Rudakova, A.V., Ryabchuk, V.K. and Serpone, N. (1998) Spectroscopic and photoluminescence studies of a wide band gap insulating material: Powdered and colloidal ZrO_2 sols. **Langmuir**; 14(18): 5011-5022.
[194] Paiverneker, V.R., Petelin, A.N., Crowne, F.J. and Nagle, D.C. (1989) Color-center-induced band-gap shift in yttria-stabilized zirconia. **Phys Rev B**; 40(12): 8555-8557.
[195] Leung, D.Y.C., Fu, X., Wang, C., Ni, M., Leung, M.K.H., Wang, X. and Fu, X. (2010) Hydrogen production over titania-based photocatalysts. **ChemSusChem**; 3(6): 681-694.
[196] Biesuz, M., Pinter, L., Saunders, T., Reece, M., Binner, J., Sglavo, V. and Grasso, S. (2018) Investigation of Electrochemical, Optical and Thermal Effects during Flash Sintering of 8YSZ. **Mater**; 11(7): 1214.
[197] Manoharan, D., Loganathan, A., Kurapati, V. and Nesamony, V.J. (2015) Unique sharp photoluminescence of size-controlled sonochemically synthesized zirconia nanoparticles. **Ultrason Sonochem**; 23: 174-184.

[198] Gionco, C., Paganini, M.C., Giamello, E., Burgess, R., Di Valentin, C. and Pacchioni, G. (2013) Paramagnetic Defects in Polycrystalline Zirconia: An EPR and DFT Study. **Chem Mater**; 25(11): 2243-2253.
[199] Sinhamahapatra, A., Jeon, J.-P., Kang, J., Han, B. and Yu, J.-S. (2016) Oxygen-deficient zirconia (ZrO_{2-x}): A new material for solar light absorption. **Sci Rep**; 6(1): 27218.
[200] Zu, D., Wang, H., Yang, T., Wei, H., Sun, S. and Wu, H. (2020) Black ZrO_2 synthesized by molten lithium reduction strategy for photocatalytic hydrogen generation. **J Am Ceram Soc**; 103(8): 4035-4042.
[201] Huang, Y., Yu, Y., Yu, Y. and Zhang, B. (2020) Oxygen vacancy engineering in photocatalysis. **Solar RRL**; 4(8): 2000037.
[202] Sun, L., Jiao, X., Liu, W., Wang, Y., Cao, Y., Bao, S.-J., Xu, Z., Kang, Y. and Xue, P. (2019) Novel oxygen-deficient zirconia (ZrO_{2-x}) for fluorescence/photoacoustic imaging-guided photothermal/photodynamic therapy for cancer. **ACS Appl Mater Interfaces**; 11(44): 41127-41139.
[203] Chen, C., Ruan, C., Zhan, Y., Lin, X., Zheng, Q. and Wei, K. (2014) The significant role of oxygen vacancy in Cu/ZrO_2 catalyst for enhancing water–gas-shift performance. **Int J Hydrog Energy**; 39(1): 317-324.
[204] Cristache, C.M., Burlibasa, M., Cristache, G., Drafta, S., Popovici, I.A., Iliescu, A.A., Zisi, S. and Burlibasa, L. (2011) Zirconia and its biomedical applications. **Metal Int**; 16(7): 18-23.
[205] Rani, V., Sharma, A., Kumar, A., Singh, P., Thakur, S., Singh, A., Le, Q.V., Nguyen, V.H. and Raizada, P. (2022) ZrO_2-Based Photocatalysts for Wastewater Treatment: From Novel Modification Strategies to Mechanistic Insights. **Catal**; 12(11): 1418.
[206] Syzgantseva, O.A., Calatayud, M. and Minot, C. (2012) Revealing the surface reactivity of zirconia by periodic DFT calculations. **J Phys Chem C**; 116(11): 6636-6644.
[207] Kouva, S., Honkala, K., Lefferts, L. and Kanervo, J. (2015) Review: monoclinic zirconia, its surface sites and their interaction with carbon monoxide. **Catal Sci Technol**; 5(7): 3473-3490.
[208] Albanese, E., Ruiz Puigdollers, A. and Pacchioni, G. (2018) Theory of ferromagnetism in reduced ZrO_{2-x} nanoparticles. **ACS Omega**; 3(5): 5301-5307.
[209] Chupka, W., Berkowitz, J. and Inghram, M.G. (1957) Thermodynamics of the Zr-ZrO2 system: The dissociation energies of ZrO and ZrO2. **The Journal of Chemical Physics**; 26(5): 1207-1210.
[210] Luo, Y.-R. and Kerr, J.A. (2012) Bond dissociation energies. **CRC handbook of chemistry and physics**; 89: 89.
[211] Wang, Q., Edalati, K., Koganemaru, Y., Nakamura, S., Watanabe, M., Ishihara, T. and Horita, Z. (2020) Photocatalytic hydrogen generation on low-bandgap black zirconia (ZrO_2) produced by high-pressure torsion. **J Mater Chem A**; 8(7): 3643-3650.
[212] Anselmi-Tamburini, U., Woolman, J.N. and Munir, Z.A. (2007) Transparent nanometric cubic and tetragonal zirconia obtained by high-pressure pulsed electric current sintering. **Adv Funct Mater**; 17(16): 3267-3273.
[213] Alvarez, A., Dong, Y. and Chen, I.W. (2020) DC electrical degradation of YSZ: Voltage-controlled electrical metallization of a fast ion conducting insulator. **J Am Ceram Soc**; 103(5): 3178-3193.

[214] Nikiforov, S., Menshenina, A. and Konev, S. (2019) The influence of intrinsic and impurity defects on the luminescent properties of zirconia. **J Lumin**; 212: 219-226.
[215] Moya, J.S., Moreno, R., Requena, J. and Soria, J. (1988) Black color in partially stabilized zirconia. **J Am Ceram Soc**; 71(11): C479-C480.
[216] Qi, F., Yang, Z., Zhang, J., Wang, Y., Qiu, Q. and Li, H. (2020) Interfacial Reaction-Induced Defect Engineering: Enhanced Visible and Near-Infrared Absorption of Wide Band Gap Metal Oxides with Abundant Oxygen Vacancies. **ACS Appl Mater Interfaces**; 12(49): 55417-55425.
[217] Lv, H., Bao, J., Ruan, F., Zhou, F., Wang, Q., Zhang, W., Guo, W., Zhang, Y., Song, X. and An, S. (2020) Preparation and properties of black Ti-doped zirconia ceramics. **J Mater Res Technol**; 9(3): 6201-6208.
[218] Morant, C., Sanz, J.M. and Galán, L. (1992) Ar-ion bombardment effects on ZrO_2. **Phys Rev B**; 45(3): 1391-1398.
[219] Janek, J. and Korte, C. (1999) Electrochemical blackening of yttria-stabilized zirconia a morphological instability of the moving reaction front. **Solid State Ion**; 116(3-4): 181-195.
[220] Farley, J.M., Thorp, J.S., Ross, J.S. and Saunders, G.A. (1972) Effect of current-blackening on the elastic constants of yttria-stabilised zirconia. **J Mater Sci**; 7(4): 475-476.
[221] Wright, D.A., Thorp, J.S., Aypar, A. and Buckley, H.P. (1973) Optical absorption in current-blackened yttria-stabilized zirconia. **J Mater Sci**; 8(6): 876-882.
[222] Thorp, J.S. and Buckley, H.P. (1973) The dielectric constants of current-blackened single crystral yttria-stabilized zirconia. **J Mater Sci**; 8(10): 1401-1408.
[223] Thorp, J.S., Aypar, A. and Ross, J.S. (1972) Electron spin resonance in single crystal yttria stabilized zirconia. **J Mater Sci**; 7(7): 729-734.
[224] Luerßen, B., Janek, J., Günther, S., Kiskinova, M. and Imbihl, R. (2002) Microspectroscopy at a moving reduction front in zirconia solid electrolyte. **Phys Chem Chem Phys**; 4(12): 2673-2679.
[225] Moghadam, F.K., Yamashita, T. and Stevenson, D.A. (1983) Characterization of the current-blackening phenomena in scandia stabilized zirconia using transmission electron microscopy. **J Mater Sci**; 18(8): 2255-2259.
[226] Ye, K., Li, K., Lu, Y., Guo, Z., Ni, N., Liu, H., Huang, Y., Ji, H. and Wang, P. (2019) An overview of advanced methods for the characterization of oxygen vacancies in materials. **Trends Anal Chem**; 116: 102-108.
[227] Yuan, Y., Yu, H., Podpirka, A., Ostdiek, P., Srinivasan, R. and Ramanathan, S. (2022) Negative Differential Resistance in Oxygen-ion Conductor Yttria-stabilized Zirconia for Extreme Environment Electronics. **ACS Appl Mater Interfaces**; 14(35): 40116-40125.
[228] Vazquez-Arce, J., Tiznado, H. and Kirchheim, R. (2022) Onset of electronic conductivity in nanometer thick films of yttria stabilized zirconia (YSZ) at high electric fields. **Acta Mater**; 229: 117826.
[229] Dong, Y. and Chen, I.W. (2018) Electrical and hydrogen reduction enhances kinetics in doped zirconia and ceria: <scp>II</scp> . Mapping electrode polarization and vacancy condensation in <scp>YSZ</scp>. **Journal of the American Ceramic Society**; 101(3): 1058-1073.
[230] Landi, S., Segundo, I.R., Freitas, E., Vasilevskiy, M., Carneiro, J. and Tavares, C.J. (2022) Use and misuse of the Kubelka-Munk function to obtain the band

gap energy from diffuse reflectance measurements. **Solid State Commun**; 341: 114573.
[231] Viezbicke, B.D., Patel, S., Davis, B.E. and Birnie, D.P. (2015) Evaluation of the Tauc method for optical absorption edge determination: ZnO thin films as a model system. **Phys Status Solidi B**; 252(8): 1700-1710.
[232] Makuła, P., Pacia, M. and Macyk, W. (2018) How To Correctly Determine the Band Gap Energy of Modified Semiconductor Photocatalysts Based on UV–Vis Spectra. **J Phys Chem Lett**; 9(23): 6814-6817.
[233] Shinar, J., Tannhauser, D. and Silver, B. (1985) ESR study of color centers in yttria stabilized zirconia. **Solid State Commun**; 56(2): 221-223.
[234] Teeparthi, S.R., Awin, E.W. and Kumar, R. (2018) Dominating role of crystal structure over defect chemistry in black and white zirconia on visible light photocatalytic activity. **Sci Rep**; 8(1).
[235] Naumenko, A., Berezovska, N., Biliy, M. and Shevchenko, O. (2008) Vibrational analysis and Raman spectra of tetragonal zirconia. **Phys Chem Solid State**; 9(1): 121-125.
[236] Hemberger, Y., Wichtner, N., Berthold, C. and Nickel, K.G. (2016) Quantification of yttria in stabilized zirconia by Raman spectroscopy. **Int J Appl Ceram**; 13(1): 116-124.
[237] Vasanthavel, S. and Kannan, S. (2018) Structural investigations on the tetragonal to cubic phase transformations in zirconia induced by progressive yttrium additions. **J Phys Chem Solids**; 112: 100-105.
[238] Chevalier, J., Gremillard, L., Virkar, A.V. and Clarke, D.R. (2009) The tetragonal‐monoclinic transformation in zirconia: lessons learned and future trends. **J Am Ceram Soc**; 92(9): 1901-1920.
[239] Zhang, J., Gao, Y., Jia, X., Wang, J., Chen, Z. and Xu, Y. (2018) Oxygen vacancy-rich mesoporous ZrO2 with remarkably enhanced visible-light photocatalytic performance. **Sol Energy Mater Sol Cells**; 182: 113-120.
[240] Ben-Michael, R., Tannhauser, D.S. and Genossar, J. (1991) ESR centers in reduced stabilized zirconia. **Phys Rev B**; 43(10): 7395-7404.
[241] Laguta, V., Buryi, M., Arhipov, P., Sidletskiy, O., Laguta, O., Brik, M.G. and Nikl, M. (2020) Oxygen-vacancy donor-electron center in Y3Al5O12 garnet crystals: Electron paramagnetic resonance and dielectric spectroscopy study. **Phys Rev B**; 101(2).
[242] Qi, F., Yang, Z., Wang, Y., Qiu, Q. and Li, H. (2021) Defects in black zirconia responsible for solar energy harvesting. **J Mater Chem C**; 9(46): 16732-16740.
[243] Nikiforov, S.V., Kortov, V.S., Kiryakov, A.N., Konev, S.F. and Men'Shenina, A.A. (2017) Increasing the Luminescence Yield of Zirconia. **Tech Phys Lett**; 43(12): 1074-1076.
[244] Bobricheva, I., Stavitsky, I., Yermolaev, V., Kotsarenko, N., Shmachkova, V. and Kochubey, D. (1998) ESR study of paramagnetic sites in sulfated zirconia. **Catal Lett**; 56: 23-27.
[245] Frolova, E.V. and Ivanovskaya, M.I. (2006) The origin of defects formation in nanosized zirconia. **Mater Sci Eng C**; 26(5-7): 1106-1110.
[246] Zhu, S., Zu, X., Wang, L. and Ewing, R. (2002) Cesium Ion Implantation in Single Crystal Yttria-Stabilized Zirconia (YSZ) and Polycrystalline $MgAl_2O_4$-YSZ. **Mater Res Soc Online Proc Library**; 713.
[247] Jakes, P. and Erdem, E. (2011) Finite size effects in ZnO nanoparticles: An electron paramagnetic resonance (EPR) analysis. **Phys Status Solidi Rapid Res Lett**; 5(2): 56-58.

[248] Lou, Q., Zeng, J., Man, Z., Zheng, L., Park, C., Kassiba, A., Liu, Y., Chen, X. and Li, G. (2019) The effect of grain boundary on the visible light absorption of $BaTi_{1-x}[Ni_{1/2}Nb_{1/2}]_xO_{3-\delta}$. **J Am Ceram Soc**; 102(12): 7405-7413.

[249] Imparato, C., Fantauzzi, M., Passiu, C., Rea, I., Ricca, C., Aschauer, U., Sannino, F., D'Errico, G., De Stefano, L., Rossi, A. and Aronne, A. (2019) Unraveling the Charge State of Oxygen Vacancies in ZrO_{2-x} on the Basis of Synergistic Computational and Experimental Evidence. **J Phys Chem C**; 123(18): 11581-11590.

[250] Lackner, P., Hulva, J., Köck, E.-M., Mayr-Schmölzer, W., Choi, J.I.J., Penner, S., Diebold, U., Mittendorfer, F., Redinger, J., Klötzer, B., Parkinson, G.S. and Schmid, M. (2018) Water adsorption at zirconia: from the ZrO_2(111)/Pt_3Zr(0001) model system to powder samples. **J Mater Chem A**; 6(36): 17587-17601.

[251] Bosio, N., Schaefer, A. and Grönbeck, H. (2022) Can oxygen vacancies in ceria surfaces be measured by O1s photoemission spectroscopy? **J Condens Matter Phys**; 34(17): 174004.

[252] Lee, N.-W., Yoon, K.R., Lee, J.-Y., Park, Y., Pyo, S.-J., Kim, G.-Y., Ha, D.-H. and Ryu, W.-H. (2019) Highly Conductive Off-Stoichiometric Zirconium Oxide Nanofibers with Controllable Crystalline Structures and Bandgaps and Improved Electrochemical Activities. **ACS Appl Energy Mater**; 2(5): 3513-3522.

[253] Deligiannakis, Y., Mantzanis, A., Zindrou, A., Smykala, S. and Solakidou, M. (2022) Control of monomeric Vo's versus Vo clusters in ZrO_{2-x} for solar-light H_2 production from H_2O at high-yield (millimoles.gr^{-1}.h^{-1}). **Sci Rep**; 12(1).

[254] Picquart, M., López, T., Gómez, R., Torres, E., Moreno, A. and Garcia, J. (2004) Dehydration and crystallization process in sol-gel zirconia. **J Therm Anal Calorim**; 76(3): 755-761.

[255] Puigdollers, A.R., Illas, F. and Pacchioni, G. (2016) Structure and Properties of Zirconia Nanoparticles from Density Functional Theory Calculations. **J Phys Chem C**; 120(8): 4392-4402.

[256] Malek, J., Matsuda, S., Watanabe, A., Ikegami, T. and Mitsuhashi, T. (1995) Crystallization kinetics of zirconia-yttria gels. **Thermochim Acta**; 267: 181-194.

[257] Lindgren, M. and Panas, I. (2017) Oxygen Vacancy Formation, Mobility, and Hydrogen Pick-up during Oxidation of Zirconium by Water. **Oxid Met**; 87(3-4): 355-365.

[258] Heiroth, S., Ghisleni, R., Lippert, T., Michler, J. and Wokaun, A. (2011) Optical and mechanical properties of amorphous and crystalline yttria-stabilized zirconia thin films prepared by pulsed laser deposition. **Acta Mater**; 59(6): 2330-2340.

[259] Jubu, P.R., Obaseki, O., Nathan-Abutu, A., Yam, F., Yusof, Y. and Ochang, M. (2022) Dispensability of the conventional Tauc's plot for accurate bandgap determination from UV–vis optical diffuse reflectance data. **Res Opt**; 9: 100273.

[260] Dash, L.K., Vast, N., Baranek, P., Cheynet, M.-C. and Reining, L. (2004) Electronic structure and electron energy-loss spectroscopy of ZrO_2 zirconia. **Phys Rev B**; 70(24).

[261] Chang, S.-M. and Doong, R.-A. (2007) Interband Transitions in Sol−Gel-Derived ZrO_2 Films under Different Calcination Conditions. **Chem Mater**; 19(19): 4804-4810.

[262] Milman, V., Perlov, A., Refson, K., Clark, S.J., Gavartin, J. and Winkler, B. (2009) Structural, electronic and vibrational properties of tetragonal zirconia under pressure: a density functional theory study. **J Condens Matter Phys**; 21(48): 485404.

[263] Götsch, T., Menzel, A., Bertel, E., Stöger-Pollach, M. and Penner, S. (2017) The Crystallographic and Electronic Phase Diagrams of Yttria-Stabilized Zirconia Model Electrolytes. **ECS Trans**; 78(1): 311-319.
[264] Islamov, D.R., Gritsenko, V.A., Perevalov, T.V., Aliev, V.S., Nadolinny, V.A. and Chin, A. (2021) Oxygen vacancies in zirconium oxide as the blue luminescence centres and traps responsible for charge transport: Part II—Films. **Materialia**; 15: 100980.
[265] Czerwiec, T., Michel, H. and Bergmann, E. (1998) Low-pressure, high-density plasma nitriding: mechanisms, technology and results. **Surf Coat Technol**; 108: 182-190.
[266] Łępicka, M. and Grądzka-Dahlke, M. (2016) Direct Current and Pulsed Direct Current Plasma Nitriding of Ferrous Materials a Critical Review. **Acta Mech et Autom**; 10(2): 150-158.
[267] Tao, X., Collins, T.J., Ao, Q., Liu, H., Dashtbozorg, B., Li, X. and Dong, H. (2022) Active screen plasma nitriding of Fe-24Mn-2Al-0.45 C TWIP steel: Microstructure evolution and a synergistic selective oxidation mechanism. **Acta Mater**; 241: 118418.
[268] Zhao, J., Liu, C., Li, J., Wu, R., Wang, J., Qian, H., Guo, H., Li, J. and Ibrahim, K. (2019) Oxygen vacancy induced electronic structure variation in the La0.2Sr0.8MnO3 thin film. **AIP Adv**; 9(5): 055208.
[269] Idriss, H. (2021) On the wrong assignment of the XPS O1s signal at 531–532 eV attributed to oxygen vacancies in photo-and electro-catalysts for water splitting and other materials applications. **Surf Sci**; 712: 121894.
[270] Sinhamahapatra, A., Jeon, J.-P., Kang, J., Han, B. and Yu, J.-S. (2016) Oxygen-deficient zirconia (ZrO2− x): a new material for solar light absorption. **Scientific reports**; 6(1): 1-8.
[271] Zhang, H., Li, Z., Kim, B.-N., Morita, K., Yoshida, H., Hiraga, K. and Sakka, Y. (2012) Effect of alumina dopant on transparency of tetragonal zirconia. **Journal of Nanomaterials**; 2012: 1-1.
[272] Buchanan, R. and Pope, S. (1983) Optical and electrical properties of yttria stabilized zirconia (YSZ) crystals. **Journal of the Electrochemical Society**; 130(4): 962.
[273] Vemury, S. and Pratsinis, S.E. (1995) Dopants in flame synthesis of titania. **Journal of the American Ceramic Society**; 78(11): 2984-2992.
[274] Etacheri, V., Seery, M.K., Hinder, S.J. and Pillai, S.C. (2011) Oxygen rich titania: A dopant free, high temperature stable, and visible-light active anatase photocatalyst. **Advanced Functional Materials**; 21(19): 3744-3752.
[275] Stojadinović, S., Vasilić, R., Radić, N. and Grbić, B. (2015) Zirconia films formed by plasma electrolytic oxidation: Photoluminescent and photocatalytic properties. **Optical Materials**; 40: 20-25.
[276] Moya, J.S., Moreno, R., Requena, J. and Soria, J. (1988) Black color in partially stabilized zirconia. **Journal of the American Ceramic Society**; 71(11): C479-C480.
[277] Sasaki, K. and Maier, J. (2000) Re-analysis of defect equilibria and transport parameters in Y2O3-stabilized ZrO2 using EPR and optical relaxation. **Solid State Ionics**; 134(3-4): 303-321.
[278] Kumar, S. and Ojha, A.K. (2015) Oxygen vacancy induced photoluminescence properties and enhanced photocatalytic activity of ferromagnetic ZrO2 nanostructures on methylene blue dye under ultra-violet radiation. **Journal of Alloys and Compounds**; 644: 654-662.

[279] Zhang, J., Gao, Y., Jia, X., Wang, J., Chen, Z. and Xu, Y. (2018) Oxygen vacancy-rich mesoporous ZrO2 with remarkably enhanced visible-light photocatalytic performance. **Solar Energy Materials and Solar Cells**; 182: 113-120.
[280] Teeparthi, S.R., Awin, E.W. and Kumar, R. (2018) Dominating role of crystal structure over defect chemistry in black and white zirconia on visible light photocatalytic activity. **Scientific reports**; 8(1): 5541.
[281] Renuka, L., Anantharaju, K., Sharma, S., Nagabhushana, H., Vidya, Y., Nagaswarupa, H. and Prashantha, S. (2017) A comparative study on the structural, optical, electrochemical and photocatalytic properties of ZrO2 nanooxide synthesized by different routes. **Journal of Alloys and Compounds**; 695: 382-395.
[282] Reddy, C.V., Reddy, I.N., Ravindranadh, K., Reddy, K.R., Kim, D. and Shim, J. (2020) Ni-dopant concentration effect of ZrO2 photocatalyst on photoelectrochemical water splitting and efficient removal of toxic organic pollutants. **Separation and Purification Technology**; 252: 117352.
[283] Reddy, C.V., Babu, B., Reddy, I.N. and Shim, J. (2018) Synthesis and characterization of pure tetragonal ZrO2 nanoparticles with enhanced photocatalytic activity. **Ceramics International**; 44(6): 6940-6948.
[284] Liu, Y., Ishihara, A., Mitsushima, S. and Ota, K.-i. (2010) Influence of sputtering power on oxygen reduction reaction activity of zirconium oxides prepared by radio frequency reactive sputtering. **Electrochimica Acta**; 55(3): 1239-1244.
[285] Choi, E.-Y. and Heo, D.H. (2018) Reduction of zirconium oxide compounds by lithium metal as a reductant in molten LiCl salt. **Journal of Nuclear Materials**; 512: 193-198.
[286] Azarian, M.H. and Mahmood, W.A.K. (2020) In‐situ sol–gel synthesis of zirconia networks in flexible and conductive composite films. **Journal of Applied Polymer Science**; 137(46): 49506.
[287] Suleiman, R.K., Kumar, A.M., Rahman, M.M., Al-Badour, F.A., Meliani, M.H. and Saleh, T.A. (2020) Effect of metal oxide additives on the structural and barrier properties of a hybrid organosilicon sol-gel coating in 3.5% NaCl medium. **Progress in Organic Coatings**; 148: 105825.
[288] Jacob, K.-H., Knözinger, E. and Benfer, S. (1994) Chemisorption of H 2 and H 2—O 2 on polymorphic zirconia. **Journal of the Chemical Society, Faraday Transactions**; 90(19): 2969-2975.
[289] Masaki, T., Nakajima, K. and Shinjo, K. (1986) High-temperature mechanical properties of Y-PSZ HIPed under an oxygen-containing atmosphere. **Journal of materials science letters**; 5: 1115-1118.
[290] Qi, F., Yang, Z., Wang, Y., Qiu, Q. and Li, H. (2021) Defects in black zirconia responsible for solar energy harvesting. **Journal of Materials Chemistry C**; 9(46): 16732-16740.
[291] Nakajima, H., Itoh, K., Kaneko, H. and Tamaura, Y. (2007) Effects of Fe doping on crystalline and optical properties of yttria-stabilized zirconia. **Journal of Physics and Chemistry of Solids**; 68(10): 1946-1950.
[292] Lv, H., Bao, J., Ruan, F., Zhou, F., Wang, Q., Zhang, W., Guo, W., Zhang, Y., Song, X. and An, S. (2020) Preparation and properties of black Ti-doped zirconia ceramics. **Journal of Materials Research and Technology**; 9(3): 6201-6208.

[293] Nakajima, H., Ishihara, H., Shen, Q., Toyoda, T., Itoh, K., Kaneko, H. and Tamaura, Y. (2007) Effect of Fe doping on photoluminescence of yttria-stabilized zirconia. **Journal of alloys and compounds**; 441(1-2): 255-258.
[294] Christian, K.H., Charalambous, H., Jha, S.K. and Tsakalakos, T. (2020) Current-ramp assisted sintering of 3YSZ: Electrochemical and microstructural comparison to flash and thermal sintering. **Journal of the European Ceramic Society**; 40(2): 436-443.
[295] Dashtbozorg, B., Shi, F., Tagliaferro, A., Abela, S., Falticeanu, L. and Dong, H. (2023) Plasma defect-engineering of bulk oxygen-deficient zirconia. **Acta Materialia**: 119457.
[296] Chen, X., Khor, K., Chan, S. and Yu, L. (2002) Influence of microstructure on the ionic conductivity of yttria-stabilized zirconia electrolyte. **Materials Science and Engineering: A**; 335(1-2): 246-252.
[297] Masó, N. and West, A.R. (2015) Electronic conductivity in yttria-stabilized zirconia under a small dc bias. **Chemistry of Materials**; 27(5): 1552-1558.
[298] Han, P. and Worrell, W. (1995) Mixed (Oxygen Ion and p-Type) Conductivity in Yttria-Stabilized Zirconia Containing Terbia. **Journal of the Electrochemical Society**; 142(12): 4235.
[299] Zhang, L., Zhu, L. and Virkar, A.V. (2016) Electronic conductivity measurement of yttria-stabilized zirconia solid electrolytes by a transient technique. **Journal of Power Sources**; 302: 98-106.
[300] Casselton, R. (1970) Low field DC conduction in yttria-stabilized zirconia. **physica status solidi (a)**; 2(3): 571-585.
[301] Torres, C., Reyes, P., Castillo, F. and Martínez, H., editors. Paschen law for argon glow discharge. **Journal of Physics: Conference Series**; 2012: IOP Publishing.
[302] Loveless, A.M. and Garner, A.L. (2017) A universal theory for gas breakdown from microscale to the classical Paschen law. **Physics of Plasmas**; 24(11).
[303] Morinaga, M., Adachi, H. and Tsukada, M. (1983) Electronic structure and phase stability of ZrO2. **Journal of Physics and Chemistry of Solids**; 44(4): 301-306.
[304] Liu, Q.-J., Liu, Z.-T. and Feng, L.-P. (2011) Elasticity, electronic structure, chemical bonding and optical properties of monoclinic ZrO2 from first-principles. **Physica B: Condensed Matter**; 406(3): 345-350.
[305] Králik, B., Chang, E.K. and Louie, S.G. (1998) Structural properties and quasiparticle band structure of zirconia. **Physical Review B**; 57(12): 7027.
[306] Murad, E. and Hildenbrand, D. (1975) Thermochemical properties of gaseous ZrO and ZrO2. **The Journal of Chemical Physics**; 63(3): 1133-1139.
[307] Murali, M., Bijani, C., Daran, J.-C., Manoury, E. and Poli, R. (2023) Acetate exchange mechanism on a Zr 12 oxo hydroxo cluster: relevance for reshaping Zr–carboxylate coordination adaptable networks. **Chemical Science**; 14(30): 8152-8163.
[308] Kurapova, O.Y., Glumov, O., Pivovarov, M., Golubev, S. and Konakov, V. (2017) Structure and conductivity of calcia stabilized zirconia ceramics, manufactured from freeze-dried nanopowder. **Rev Adv Mater Sci**; 52(1-2): 134-141.
[309] Wright, D., Thorp, J., Aypar, A. and Buckley, H. (1973) Optical absorption in current-blackened yttria-stabilized zirconia. **Journal of Materials Science**; 8: 876-882.

[310] Nagle, D., PaiVerneker, V., Petelin, A. and Groff, G. (1989) Optical absorption of electrolytically colored single crystals of yttria-stabilized zirconia. **Materials Research Bulletin**; 24(5): 619-623.
[311] PaiVerneker, V., Petelin, A., Crowne, F. and Nagle, D. (1989) Color-center-induced band-gap shift in yttria-stabilized zirconia. **Physical Review B**; 40(12): 8555.
[312] Bonola, C., Camagni, P., Chiodelli, P. and Samoggia, G. (1991) Study of defects introduced by electroreduction in YSZ. **Radiation Effects and Defects in Solids**; 119(1): 457-462.
[313] Thorp, J., Aypar, A. and Ross, J. (1972) Electron spin resonance in single crystal yttria stabilized zirconia. **Journal of Materials Science**; 7: 729-734.
[314] Shinar, J., Tannhauser, D. and Silver, B. (1985) ESR study of color centers in yttria stabilized zirconia. **Solid state communications**; 56(2): 221-223.
[315] Ben-Michael, R., Tannhauser, D. and Genossar, J. (1991) ESR centers in reduced stabilized zirconia. **Physical Review B**; 43(10): 7395.
[316] Azzoni, C. and Paleari, A. (1989) EPR study of electron traps in x-ray-irradiated yttria-stabilized zirconia. **Physical Review B**; 40(10): 6518.
[317] Osendi, M.I., Moya, J.S., Serna, C.J. and SORIA, J. (1985) Metastability of tetragonal zirconia powders. **Journal of the American Ceramic Society**; 68(3): 135-139.
[318] Casselton, R.E., Penny, J. and Reynolds, M. STRUCTURAL CONSEQUENCES OF BLACKENING IN YTTRIA-STABILIZED ZIRCONIA. International Research and Development Co. Ltd., Newcastle upon Tyne, Eng., 1971.
[319] Moghadam, F., Yamashita, T. and Stevenson, D. (1983) Characterization of the current-blackening phenomena in scandia stabilized zirconia using transmission electron microscopy. **Journal of materials science**; 18: 2255-2259.
[320] Lévy, M., Fouletier, J. and Kleitz, M. (1980) Electronic conductivity of non stoichiometric yttria-doped ceria. **Le Journal de Physique Colloques**; 41(C6): C6-335-C336-339.
[321] Wang, J., Xiong, J., Peng, Q., Fan, H., Wang, Y., Li, G. and Shen, B. (2009) Effects of DC plasma nitriding parameters on microstructure and properties of 304L stainless steel. **Materials Characterization**; 60(3): 197-203.
[322] Klein, A., Cardoso, R., Pavanati, H., Binder, C., Maliska, A., Hammes, G., Fusao, D., Seeber, A., Brunatto, S.y. and Muzart, J. (2013) DC plasma technology applied to powder metallurgy: an overview. **Plasma Science and Technology**; 15(1): 70.
[323] Li, C. (2010) Active screen plasma nitriding–an overview. **Surface engineering**; 26(1-2): 135-141.
[324] Guillon, O., Elsässer, C., Gutfleisch, O., Janek, J., Korte-Kerzel, S., Raabe, D. and Volkert, C.A. (2018) Manipulation of matter by electric and magnetic fields: toward novel synthesis and processing routes of inorganic materials. **Materials today**; 21(5): 527-536.
[325] Graeve, O.A. (2008) Zirconia. In: **Ceramic and glass materials: structure, properties and processing**. Springer. p 169-197.
[326] Yin, L., Nakanishi, Y., Alao, A.-R., Song, X.-F., Abduo, J. and Zhang, Y. (2017) A review of engineered zirconia surfaces in biomedical applications. **Procedia Cirp**; 65: 284-290.

[327] Elsaka, S.E. (2019) Optical and mechanical properties of newly developed monolithic multilayer zirconia. **Journal of prosthodontics**; 28(1): e279-e284.
[328] Yin, L., Jahanmir, S. and Ives, L. (2003) Abrasive machining of porcelain and zirconia with a dental handpiece. **Wear**; 255(7-12): 975-989.
[329] Chen, H., Zhang, Y. and Ding, C. (2002) Tribological properties of nanostructured zirconia coatings deposited by plasma spraying. **Wear**; 253(7-8): 885-893.
[330] De Aza, A., Chevalier, J., Fantozzi, G., Schehl, M. and Torrecillas, R. (2002) Crack growth resistance of alumina, zirconia and zirconia toughened alumina ceramics for joint prostheses. **Biomaterials**; 23(3): 937-945.
[331] Cionca, N., Hashim, D. and Mombelli, A. (2017) Zirconia dental implants: where are we now, and where are we heading? **Periodontology 2000**; 73(1): 241-258.
[332] Morita, K., Naito, F. and Terada, D. (2021) Microcrack healing in zirconia ceramics under a DC electric field/current. **Journal of the European Ceramic Society**; 41(16): 282-289.
[333] Wang, J. and Stevens, R. (1988) Modification of indentation cracks in TZP ceramics by thermal treatment. **Journal of materials science letters**; 7: 560-562.
[334] Houjou, K., Ando, K. and Takahashi, K. (2009) Crack-healing behaviour of Zirconia/SiC composite ceramics. **Journal of the Society of Materials Science, Japan**; 58(6): 510-515.
[335] Kayukawa, S., Katsuyama, Y., Kodaira, A., Tokunaga, T., Morita, K., Nakamura, A., Higuchi, K. and Yamamoto, T. (2023) Microcrack healing in single-crystal cubic zirconia by thermal annealing. **Journal of the European Ceramic Society**; 43(3): 1078-1086.
[336] Takahashi, S., Morita, K., Nambu, K., Terada, D., Kobayashi, K., Tokunaga, T. and Yamamoto, T. (2023) Effect of Initial Grain Size on Crack Healing Behavior under DC Electric Field of Zirconia (8Y‐CSZ) Ceramic. **Advanced Engineering Materials**: 2201807.
[337] Moradkhani, A., Baharvandi, H., Tajdari, M., Latifi, H. and Martikainen, J. (2013) Determination of fracture toughness using the area of micro-crack tracks left in brittle materials by Vickers indentation test. **Journal of Advanced Ceramics**; 2: 87-102.